

2009

Development and Validation of a Markerless Radiostereometric Analysis (RSA)System

Anne-Marie V. Allen

Follow this and additional works at: <https://ir.lib.uwo.ca/digitizedtheses>

Recommended Citation

Allen, Anne-Marie V., "Development and Validation of a Markerless Radiostereometric Analysis (RSA)System" (2009). *Digitized Theses*. 3934.
<https://ir.lib.uwo.ca/digitizedtheses/3934>

This Thesis is brought to you for free and open access by the Digitized Special Collections at Scholarship@Western. It has been accepted for inclusion in Digitized Theses by an authorized administrator of Scholarship@Western. For more information, please contact wlsadmin@uwo.ca.

DEVELOPMENT AND VALIDATION OF A MARKERLESS RADIOSTEREOMETRIC ANALYSIS (RSA) SYSTEM

(SPINE TITLE: DEVELOPMENT AND VALIDATION OF A MARKERLESS RSA SYSTEM)

(Thesis Format: Monograph)

by

Anne-Marie V. Allen

Biomedical Engineering Graduate Program
in Engineering Science

Submitted in partial fulfillment
of the requirements for the degree of
Master of Engineering Science

! /
The School of Graduate and Postdoctoral Studies
The University of Western Ontario
London, Ontario, Canada
December, 2009

© Anne-Marie V. Allen 2009

THE UNIVERSITY OF WESTERN ONTARIO
SCHOOL OF GRADUATE AND POSTDOCTORAL STUDIES
CERTIFICATE OF EXAMINATION

SUPERVISOR

Thomas R. Jenkyn, Ph.D.
Department of Mechanical & Materials Engineering
School of Kinesiology

SUPERVISORY COMMITTEE

Cynthia E. Dunning, Ph.D.
Department of Mechanical & Materials Engineering

James A. Johnson, Ph.D.
Department of Mechanical & Materials Engineering

EXAMINING BOARD

Volker Nolte, Ph.D.
School of Kinesiology

James A. Johnson, Ph.D.
Department of Mechanical & Materials Engineering

James C. Lacefield, Ph.D.
Department of Electrical and Computer Engineering

The thesis by *Anne-Marie V. Allen* entitled

DEVELOPMENT AND VALIDATION OF A MARKERLESS RADIOSTEREOMETRIC
ANALYSIS (RSA) SYSTEM

is accepted in partial fulfillment of the requirements for the degree of
Master of Engineering Science

Date

Chair of the Thesis Examination Board

ABSTRACT

A markerless radiostereometric analysis (RSA) system was developed to measure three-dimensional (3D) skeletal kinematics using biplanar fluoroscopy. A virtual set-up was created, in which the fluoroscope foci and image planes were positioned. Computed tomography (CT) was used to create 3D bone models that were imported into the virtual set-up and manually moved until their projections, as viewed from the two foci, matched the two images. The accuracy of the markerless RSA system in determining relative shoulder kinematic translations and orientations was evaluated against the “gold standards” of a precision cross-slide table and a standard RSA system, respectively. Average root mean squared errors (RMSEs) of 0.082 mm and 1.18° were found. In an effort to decrease subject’s radiation exposure, the effect of lowering CT dosage on markerless RSA accuracy was evaluated. Acceptable accuracies were obtained using bone models derived from one-ninth of the normal radiation dose.

Keywords: fluoroscopy; radiostereometric analysis (RSA); validation; shoulder; kinematics; computed tomography (CT); radiation dose

ACKNOWLEDGEMENTS

I would like to thank my supervisor Dr. Jenkyn for giving me the opportunity to work on such an exciting and challenging thesis topic. I appreciate your help and encouragement during my time here.

Angela, I am deeply grateful for your unwavering support, guidance and confidence in me. I've learned so much from you! Thank you not only for your priceless academic guidance, but for always being such a good friend!

Crystal, I've really appreciated your support and friendship through all of this. Thanks for all of the rides, for feeding me and helping to keep me sane.

To everyone else in WOBL – Beck, Rebecca, Kristin, Kristyn, Shawn, Angelo, Dan and Ian – thanks for making this process much more enjoyable and for the needed distractions in the lab.

Chris, thanks for your unconditional love and support. You always took the time to understand and listen to my problems and I really value your input. Your honestly spoken, "You can do it Annie!", got me through a lot of bad days. You really helped me on the home stretch!

Mum, Dad and Clay, your encouragement and love mean the world to me! Mum, thanks for your unconditional emotional support. You were always there to share in the excitement of my victories and encourage me during the tough times. Dad, thanks for your undying confidence in me and helping me see the bigger picture. Clay, your presence makes me calm and happy – thanks for coming to visit!

TABLE OF CONTENTS

Certificate of Examination	ii
Abstract	iii
Acknowledgements	iv
Table of Contents	v
List of Tables	ix
List of Figures	x
List of Appendices	xiii
List of Abbreviations, Symbols and Nomenclature	xv
Index of Terms	xix
CHAPTER 1 – INTRODUCTION	1
1.1 Skeletal Kinematics	1
1.2 History of RSA	1
1.2.1 Standard RSA	1
1.2.2 Markerless RSA	3
1.3 Algorithms	6
1.3.1 Standard RSA	6
1.3.2 Markerless RSA	9
1.3.2.1 Template Matching	11
1.3.2.2 Hypothesis and Test Method	11
1.3.2.3 Manual Matching	14
1.4 Experimental Set-up	15
1.4.1 Single Plane	15
1.4.2 Dual Plane	17
1.5 Technology	18
1.5.1 Imaging to Acquire Radiographs	18
1.5.1.1 Fluoroscopy	19
1.5.2 Methods to Create 3D Computer Models	20
1.5.2.1 Computed Tomography Overview	21
1.5.2.2 Computed Tomography Dosage	23

1.6	Shoulder Complex	24
1.6.1	Anatomy	25
1.6.1.1	Bones	26
1.6.1.2	Articulations	26
1.6.2	Kinematics	28
1.6.2.1	Basic Movements	28
1.6.2.2	Anatomical Coordinate Systems	29
1.7	Study Rationale	29
1.8	Objectives and Hypothesis	30
1.9	Overview	31
CHAPTER 2 – DEVELOPMENT OF A MARKERLESS RSA SYSTEM.....		32
2.1	Introduction	32
2.2	Calibration	34
2.2.1	Calibration Algorithm	36
2.2.1.1	Fluoroscope Model	37
2.2.1.2	Pixel Size Calculation	43
2.2.1.3	Parameter Estimation	43
2.2.2	Image Plane Correction	46
2.3	Experimental Set-up Recreation	50
2.4	Model Creation	53
2.5	Matching	54
CHAPTER 3 – METHODS		56
3.1	Validation Study	56
3.1.1	Experimental Set-up	57
3.1.2	Experimental Protocol	58
3.1.3	3D Computer Models	60
3.1.4	Experimental Set-up Recreation	61
3.1.5	Inter-Operator and Intra-Operator Reliability	62
3.1.6	Kinematics	63
3.1.7	Data and Statistical Analysis	63
3.1.7.1	Kinematic Translation	63

3.1.7.2	Kinematic Orientation	63
3.1.7.3	Inter-Operator and Intra-Operator Reliability	64
3.2	Dosage Study	64
3.2.1	CT Acquisition	64
3.2.2	Fluoroscopic Testing	65
3.2.3	3D Model Creation	68
3.2.4	Experimental Set-up Recreation	72
3.2.5	Kinematics	72
3.2.6	Data Analysis	72
CHAPTER 4 – RESULTS.....		73
4.1	Calibration.....	73
4.1.1	Parameter Estimation	73
4.1.2	Image Plane Correction	74
4.2	Validation Study	74
4.2.1	Translation.....	74
4.2.2	Orientation.....	77
4.2.3	Inter-Operator Reliability	78
4.2.4	Intra-Operator Reliability	79
4.3	Dosage Study	80
4.3.1	Kinematics.....	80
4.3.2	CT Dosage.....	81
4.3.3	3D Model Creation and Landmark Digitization.....	82
CHAPTER 5 – DISCUSSION.....		83
5.1	Validation Study	83
5.1.1	Kinematics.....	83
5.1.1.1	Manual Matching	84
5.1.1.2	Digitally Reconstructed Radiographs.....	85
5.1.1.3	Single-Plane.....	86
5.1.1.4	Standard RSA	86
5.1.2	Inter-Operator and Intra-Operator Reliability	87
5.2	Dosage Study	88

CHAPTER 6 – GENERAL DISCUSSION AND CONCLUSIONS.....	90
6.1 Summary	90
6.2 Limitations	91
6.3 Strength	94
6.4 Recommendations and Future Directions	95
6.5 Significance.....	97
REFERENCES.....	98
Curriculum Vitae	163

LIST OF TABLES

Table 3.1: Orientation and translation of the humerus relative to the scapula	59
Table 3.2: CT protocol descriptions.....	65
Table 4.1: ICCs, SEM, RMSE for all three translations.....	75
Table 4.2: Difference between kinematic orientations as measured using standard and markerless RSA	78
Table 4.3: Kinematic parameters determined by three different operators matching the same pose	79
Table 4.4: Kinematic parameters determined by three different operators matching the same pose	79
Table 4.5: Difference in kinematic parameters when using CT Protocol #1 and CT Protocols #2 and #3, for Position #1	80
Table 4.6: Difference in kinematic parameters between CT Protocol #1 and CT Protocols #2 and #3, for Position #2	81
Table 4.7: CTDI and DLP for CT Protocols #1, #2 and #3	82

LIST OF FIGURES

Figure 1.1: Biplanar RSA calibration set-up.....	7
Figure 1.2: Depiction of foci position calculation	8
Figure 1.3: Depiction of object point position calculation	9
Figure 1.4: Markerless RSA experimental set-up.....	10
Figure 1.5: Single plane RSA calibration set-up	16
Figure 1.6: Uniplanar RSA calibration set-up	17
Figure 1.7: Components of a fluoroscope.....	20
Figure 1.8: Helical computed tomography	22
Figure 1.9: Shoulder complex.....	25
Figure 1.10: Basic shoulder movements.....	28
Figure 2.1: Markerless RSA flow diagram.....	33
Figure 2.2: Calibration frame showing the x, y, and z axes in red, green and blue respectively	34
Figure 2.3: Distortion grid	35
Figure 2.4: Calibration frame image.....	36
Figure 2.5: Distortion grid image.....	36
Figure 2.6: Perspective projection model	38
Figure 2.7: Perspective projection model viewed in the Y' direction.....	39
Figure 2.8: Perspective projection model viewed in the Z' direction.....	39
Figure 2.9: Distortion-corrected 2D calibration points shown as open squares and uncorrected points as black circular image points	47
Figure 2.10: Projected points derived from 3D calibration frame coordinates are shown in open red squares.....	48
Figure 2.11 : Two viewpoints from the two x-ray foci.....	51
Figure 2.12: Experimental set-up.....	52
Figure 2.13: Rendered 3D model of humerus as viewed in Rhinoceros	53
Figure 2.14: Rendered 3D model of scapula as viewed in Rhinoceros	53
Figure 2.15: Humerus matched to fluoroscopic images	55
Figure 2.16: Scapula matched to fluoroscopic images	55
Figure 3.1: Experimental set-up for validation study	58
Figure 3.2: Images taken of bone models for the validation study.....	60

Figure 3.3: Experimental set-up recreation of Orientation #1	62
Figure 3.4: Experimental set-up for CT dosage study with a bone phantom representing the cadaveric shoulder.....	66
Figure 3.5: Coronal view of the cadaveric shoulder abducted 45°	67
Figure 3.6: Sagittal-Transverse view of the cadaveric shoulder abducted 45°	67
Figure 3.7: Rendered 3D model of shoulder using protocol#1 CT scans as viewed in Rhinoceros	69
Figure 3.8: Rendered 3D model of shoulder using protocol #2 CT scans as viewed in Rhinoceros	70
Figure 3.9: Rendered 3D model of shoulder using protocol #3 CT scans as viewed in Rhinoceros	71
Figure 4.1: Bland-Altman plot for Orientation #1 in anterior translation.....	76
Figure 4.2: Bland-Altman plot for Orientation #2 in inferior translation	76
Figure 4.3: Bland-Altman plot for Orientation #3 in posterior translation.....	77
Figure A.1: Pixel grid drawing	106
Figure A.2: Pixel number guide.....	110
Figure C.1: Coordinate system for distortion-corrected points	115
Figure E.1: Picture of experimental set-up	139
Figure E.2: Creating coordinate systems	141
Figure E.3: Rot(Z,-0.1006rad)	142
Figure E.4: Rot(Z,-0.1006rad) Rot(Y,0.2395rad).....	143
Figure E.5: Rot(Z,-0.1006rad) Rot (Y,0.2395rad) Rot (X,0.03574rad)	144
Figure E.6: Vector creation.....	146
Figure E.7: Image plane creation	147
Figure E.8: Guide to orient image plane to fluoro B coordinate system	148
Figure E.9: Image plane oriented to fluoro B coordinate system	149
Figure E.10: X-ray source modeled as a perspective camera	150
Figure F.1: Pixel grid coordinate system	151
Figure F.2: Distortion grid numbering.....	152
Figure F.3: Initial distortion grid coordinate system	153
Figure F.4: Final distortion grid coordinate system.....	154
Figure F.5: Calibration image with 2D distortion-corrected points as open squares and uncorrected points as black circular points	155

Figure F.6: 2D distortion-corrected points as open black squares, 3D projected points as open red squares and uncorrected points as black circular points	156
Figure F.7: Final image plane pose.....	157

LIST OF APPENDICES

APPENDIX A – PIXEL SIZE CALCULATION.....	106
A.1 Pixel Grid Drawing	106
A.2 Pixel Size Calculator Code	107
A.3 Pixel Number Guide.....	110
APPENDIX B – SYMBOLIC EQUATIONS FOR CALIBRATION ALGORITHM CREATED IN MAPLE	111
APPENDIX C – MATLAB CODE AND INSTRUCTIONS FOR ESTIMATION OF CALIBRATION PARAMETERS.....	115
C.1 Instructions	115
C.2 “Calibration_Points.m”	116
C.3 “Proj_Points_Calc.m”	118
C.4 “Starting_Parameters.m”	119
C.5 “Optimization_Main.m”	123
C.6 “Objfun.m”	125
C.7 “Confun.m”	126
APPENDIX D – CODE FOR IMAGE PLANE CORRECTION.....	127
D.1 “DistGrid_RotTrans.m”	127
D.2 “ImportPoints.rvb”	128
D.3 “ProjectPoints.rvb”	131
D.4 “Rot_Trans_ImPlane.m”	134
D.5 “Rot_Trans_ImPlane_objfun.m”	137
D.6 “Rot_Trans_ImPlane_confun.m”	138
APPENDIX E – INSTRUCTIONS FOR EXPERIMENTAL SET-UP RECREATION IN RHINOCEROS.....	139
E.1 Initial Notes	139
E.2 Coordinate System Creation.....	140
E.3 Euler Angle Rotations	142
E.4 Vector Creation	145
E.5 Image Plane	146

E.6 Modeling X-Ray Source as a Perspective Camera.....	149
E.7 Importing an Image	150
APPENDIX F – IMAGE PLANE CORRECTION INSTRUCTIONS.....	151
F.1 Image Plane Coordinate Systems	151
F.2 Pixel Grid Coordinate System	152
F.3 Distortion Grid Coordinate System	153
F.4 Initial Estimate of Image Plane Correction	154
F.5 Final Image Plane Correction	154
APPENDIX G – MATCHING INSTRUCTIONS AND CODE	158
G.1 Matching Instructions	158
G.2 “ExportPoints.rvb”	159
APPENDIX H – LETTER OF PERMISSION TO REPRODUCE JOURNAL MATERIAL.....	161

LIST OF ABBREVIATIONS, SYMBOLS AND NOMENCLATURE

$^{\circ}$ - degree(s)

μm – micrometre(s)

α – amount of elevation

β – plane of elevation

γ – internal/external rotation

θ – rotation about the Z axis

ψ – about the X axis (rotation in the plane)

ϕ – rotation about the Y axis (inclination)

2D – two dimensional (two dimensions)

3D – three dimensional (three dimensions)

ACL – anterior cruciate ligament

CAD – computer aided design

C – 2D image plane coordinate system horizontal axis as defined by the distortion grid

c – C coordinate of an image point in the image plane coordinate system

c_i – C coordinate of image point i in the image plane coordinate system

c_s – C coordinate of the projected x-ray source in the image plane coordinate system

cm – centimetre

CT – computed tomography

CTDI – computed tomography dose index

d – distance from the x-ray source (s) to the projection of the x-ray source on the image plane (s')

dcp_c_i – C coordinate of distortion-corrected point

dcp_l_i – L coordinate of distortion-corrected point

DLP – dose length product

DRR – digitally reconstructed radiographs

E(ξ) – root mean squared error (RMSE)

IBRSA – image-based RSA

ICC – intra-class correlation coefficient

ICP – iterative closest point

IIP – iterative inverse point

II – image intensifier

ISB – International Society of Biomechanics

kV – kilovoltage

kVp – peak kilovoltage

L – 2D image plane coordinate system vertical axis as defined by the distortion grid

l – L coordinate of an image point in the image plane coordinate system

l_i – L coordinate of image point i in the image plane coordinate system

l_s – L coordinate of the projected x-ray source in the image plane coordinate system

m_{kl} – the kth row and lth column of the matrix used to estimate the 2D projected image points (**M**(ξ))

mA – milliamperes

mGy – milligray

mGy·cm – milligray centimetre

MIMICS – Materialise Interactive Medical Image Control System

mm – millimetre(s)

$M(\xi)$ – matrix used to estimate the 2D projected image points

MRI – magnetic resonance imaging

np_c_i – new C coordinates of the distortion-corrected points following rotation and translation in the image plane

np_l_i – new L coordinates of the distortion-corrected points following rotation and translation in the image plane

NOA – non-overlapping area

o – the origin of the calibration frame

pix – pixel

RMSE – root mean squared error

RSA – radiostereometric analysis

s – position of the x-ray source

s' – position of the projection of the x-ray source onto the image plane

s_p – pixel size in millimetres (mm)

SEM – standard error of measurement

SI – International System of Units

stl – stereolithography

SD – standard deviation

V – voltage

WOQIL – Wolf Orthopaedic Quantitative Imaging Laboratory

x' – X' coordinate of a calibration point in the projection coordinate system

x_i – X coordinate of the 3D calibration point i in the calibration frame coordinate system

x_s – X coordinate of the x-ray source in the calibration frame coordinate system
 X – axis in the calibration frame coordinate system
 X' – axis in the projection coordinate system
 y' – Y' coordinate of a calibration point in the projection coordinate system
 y_i – Y coordinate of 3D calibration point i in the calibration frame coordinate system
 y_s – Y coordinate of x-ray source in the calibration frame coordinate system
 Y – axis in the calibration frame coordinate system
 Y' – axis in the projection coordinate system
 z' – Z' coordinate of a calibration point in the projection coordinate system
 z_i – Z coordinate of 3D calibration point i in the calibration frame coordinate system
 z_s – coordinate of x-ray source in the calibration frame coordinate system
 Z – axis in the calibration frame coordinate system
 Z' – axis in the projection coordinate system

INDEX OF TERMS

Medical Definitions were cited or adapted from Dorland's Online Medical Dictionary (www.mercksource.com)

Abduct: To draw away from the midline of the body

Acetabular: Pertaining to the cup-shaped cavity on the lateral surface of the hip bone

Acromion process: The lateral extension of the spine of the scapula, forming the highest point on the shoulder; called also acromion

Acromioclavicular: Pertaining to the acromion and the clavicle

Adduct: To draw towards the midline of the body

Anatomical neck: The constriction of the humerus just below its proximal articular surface

Anterior: Situated toward the front

Arthroplasty: The surgical repair of a joint

Anthropometry: The science of dealing with the measurements of the size, weight, and proportions of the human body. Anthropometric, adj

Articulation: The action or manner in which the parts of a joint come together

Aseptic: In the absence of pathological micro-organisms

Cadaveric: Pertaining to a human body preserved for anatomical study

Cartilage: A covering on the articular surface of bones in synovial joints, which allows for smooth joint motion

Clavicle: An elongated, slender, curved bone (collar bone) lying horizontally at the root of the neck, in the upper part of the thorax

Coracoid process: A curved process arising from the upper neck of the scapula and overhanging the shoulder joint; called also coracoid.

Coronal plane: A vertical plane, perpendicular to the sagittal plane that separates the body into anterior (front) and posterior (back) portions

Cost function: See objective function

Distal: Situated away from the point of attachment or centre of the body

Dynamics: Branch of mechanics that is concerned with the effects of forces on the motion of a body or system of bodies

Epicondyle: A rounded projection at the end of a bone, usually a place of attachment for ligaments and tendons

Extension: An unbending movement around a joint in a limb that increases the angle between the bones of the limb at the joint

External rotation: Rotation about the long axis of the humerus laterally

Fibrocartilage: Cartilage of parallel, thick, compact collagenous bundles, separated by narrow clefts containing the typical cartilage cells.

Flexion: A bending movement around a joint in a limb that decreases the angle between the bones of the limb at the joint

Frontal plane: See coronal plane

Glenohumeral: Pertaining to the glenoid and the humerus

Glenoid fossa: A shallow socket on the lateral side of the scapula

Glenoid labrum: Fibrocartilaginous rim around the edge of the glenoid cavity

Gold standard: A benchmark that is considered to be true

Goniometer: An instrument for measuring angles

Greater tuberosity: The posterior and lateral tuberosity on the neck of the humerus

Humeral head: The large rounded head of the humerus, articulates with the glenoid fossa

Humerus: The longest bone of the upper arm or forelimb extending from the shoulder to the elbow

In vitro: Outside the living body in an artificial environment

In vivo: In the living body of a plant or animal

Inferior: Situated below, or directed downwards

Internal rotation: Rotation about the long axis of the humerus medially

Joint Laxity: Looseness of muscles or soft tissue surrounding a joint

Kinematics: The branch of mechanics dealing with the study of the motion of a body or a system of bodies without consideration of its mass or the forces acting on it

Labrum: An edge, rim or lip

Lateral: Situated away from the midline of the body

Lesser tuberosity: The anterior tuberosity on the neck of the humerus

Ligament: A tough band of tissue that connects bones

Medial: Situated closer to the midline of the body

Objective function: (also cost function) Optimization parameter that is used to guide the algorithm towards determining a solution to an indeterminate system

Optimization: A mathematical algorithm that is used to find the best solution to an indeterminate system based on its objective function

Orthopaedics: A branch of surgery dealing with the preservation and restoration of the function of the skeletal system, its articulations, and associated structures

Pathology: The branch of medicine treating the essential nature of disease

Posterior: Situated behind or toward the hind part of the body

Proximal: Situated toward or closer to the point of attachment or centre of the body

Radio opaque: Obstructing the passage of radiant energy, such as x-rays

Radiostereometric Analysis: The reconstruction of a three-dimensional object from two images

Rotator cuff: Group of muscles surrounding the glenohumeral joint

Sagittal plane: A vertical longitudinal plane that divides a body into right and left halves

Scapula: A large, flat and triangular bone in the posterior shoulder (shoulder blade)

Scapulothoracic: Pertaining to the scapula and thorax

Superior: Situated above or directed upwards

Scapular notch: A notch on the superior border of the scapula

Sternoclavicular: Pertaining to the sternum and clavicle

Sternum: Elongated flat bone, forming anterior wall of the chest

Synovial joint: A specialized joint that permits more or less free movement, the union of the bony elements being surrounded by an articular capsule enclosing a cavity lined by synovial membrane

Tendon: A tough cord or band of connective tissue that attaches a muscle to bone or cartilage

Thorax: The chest

Transverse plane: Horizontal plane passing through the body perpendicular to the coronal and sagittal planes, dividing the body into superior and inferior segments

Tuberosity: a projection or a protuberance, especially at the end of a bone for muscle or tendon attachment

CHAPTER 1 – INTRODUCTION

OVERVIEW: This chapter begins by detailing the history of radiostereometric analysis (RSA) and its applications. A description of the algorithms used to perform both standard and markerless RSA, as well as current experimental set-ups and technologies used is provided. A brief summary of the shoulder anatomy and kinematics is also given.

1.1 SKELETAL KINEMATICS

Measuring skeletal kinematics is an important and challenging task in biomechanical research. It is necessary to track three-dimensional (3D) joint motion in order to quantitatively evaluate the effects of medical interventions such as orthopaedic surgeries and physiotherapy regimes. Tracking skeletal kinematics can also provide insights into normal joint function and the development and progression of musculoskeletal diseases and injuries. Various methods currently exist to assess joint kinematics, but it remains difficult to do so both accurately and non-invasively.

1.2 HISTORY OF RSA

1.2.1 STANDARD RSA

Stereophotogrammetry is defined as “measurements in pictures that make it possible to reconstruct a three-dimensional object from two-dimensional images” (Selvik, 1989). This method is more than a century old, but in 1974, Selvik was the first person to apply x-ray stereophotogrammetry to measure relative rigid body motion of the skeletal

system (Selvik, 1989). In 1983, Selvik named his method Roentgen stereophotogrammetric analysis (RSA) (Kärrholm *et al.*, 2006), which is now also synonymous with the terms radiostereometric analysis and radiostereometry (Valstar *et al.*, 2005). Since other RSA variations have since been developed, the method developed by Selvik will be referred to as standard RSA when being compared with other RSA techniques.

The pose of an object refers to its position and orientation in 3D space. In order to determine a rigid object's pose, the position of at least three non-collinear points on the object must be known. Standard RSA determines the pose of 3D objects through calculating the position of markers that have been attached to the object. Small tantalum beads inserted into bone or attached to implants have become the most common markers of choice (Valstar *et al.*, 2005). Tantalum markers are used due to their chemical and biological inertness and radio opacity, making them easily identifiable on radiographs (Aronson *et al.*, 1985).

The first clinical RSA studies examined motion following spine fusions (Olsson *et al.*, 1976) and the growth of bones of the skull (Rune *et al.*, 1979) and lower extremities (Bylander *et al.*, 1981). RSA has also proven to be a useful tool to monitor the effect of surgical procedures performed to compensate for growth disorders that result in skeletal deformities (Kärrholm *et al.*, 1983).

Since 1988 RSA has been used to measure joint laxity, with the first study quantifying knee joint laxity (Edixhoven *et al.*, 1987). Early RSA studies also provided insight into 3D laxity changes following common injuries and disorders such as anterior cruciate ligament (ACL) tears (Kärrholm *et al.*, 1988), posterior cruciate ligament tears

(Jonsson & Kärrholm, 1999) and lateral ankle instabilities (Löfvenberg *et al.*, 1989). Furthermore the success of interventions such as joint reconstructive surgeries (Löfvenberg *et al.*, 1994) and braces (Jonsson & Kärrholm, 1990) have been quantified.

With the expansion of the use of total joint replacements in the 1970s, aseptic implant loosening became an increasing problem, specifically in total knee arthroplasty and total hip arthroplasty (Kärrholm *et al.*, 2006). Due to the high accuracy and repeatability of RSA, this method was able to detect early implant loosening, which could not have been measured using traditional radiographs or other available tools (Malchau *et al.*, 1995). Analyzing prosthetic fixation and wear remains the most popular and successful applications of RSA (Ciccotti *et al.*, 1994; Dunbar *et al.*, 2009; Nelissen *et al.*, 1998; van Door *et al.*, 2002). Due to this success, it has been suggested that RSA be included as a standard testing protocol before implants become available for general use (Valstar *et al.*, 2005).

1.2.2 MARKERLESS RSA

In order to perform standard RSA on implants, the implants must be manufactured with integrated tantalum makers, which drastically increases the implant cost and extends the study planning time. Implants with attached markers are considered to be newly designed implants and as such must undergo all of the necessary testing and procedures required of new designs to ensure safety. Marking implants might also compromise the strength of the implant and cause local stresses in the cement used for fixation to the bone (Kärrholm *et al.*, 2006). With this motivation, markerless RSA methods were developed, which eliminated the need to insert beads into the bones and implants under study.

Even though markerless RSA methods are fairly new, their origins date back to the first RSA study to analyze total hip prostheses wear and migration (Baldursson *et al.*, 1979). Instead of only using inserted beads as markers, this study used the prosthetic femoral head and the ends of the wire in the acetabular socket as markers. Other groups continued to use prosthetic landmarks and forms, such as the head, shoulder and tip of the femoral components (Kiss *et al.*, 1996) and the projection of the hemispherical section and base circle of acetabular cups (Valstar *et al.*, 1997).

These advancements in studying prosthetic migration, however, all relied on well-defined landmarks or basic geometrical shapes. In order to analyze more complexly shaped implants and skeletal kinematics, more generally applicable markerless RSA methods were developed. These markerless RSA methods have many names depending on the algorithms employed and laboratories in which the studies were conducted. These names include model-based tracking (Bey *et al.*, 2006), image-based RSA (IBRSA) (de Bruin *et al.*, 2008), image registration based on digitally reconstructed radiographs (Lemieux *et al.*, 1994), image matching method (Bingham & Li, 2006) and model based Roentgen stereophotogrammetry (Valstar *et al.*, 2001).

The earliest studies to employ these general markerless RSA methods used a single plane set-up to study knee replacement kinematics based on an automated template matching algorithm (Banks & Hodge, 1996; Dennis *et al.*, 1996; Hoff *et al.*, 1998). To provide more out-of-plane accuracy dual plane set-ups have also been introduced to study knee replacement kinematics (Bingham & Li, 2006; Kaptein *et al.*, 2003; Valstar *et al.*, 2001). In addition to knee replacements, shoulder (Mahfouz *et al.*, 2005), ankle (Conti *et*

al., 2006; Komistek *et al.*, 2000) and hip (Kaptein *et al.*, 2006) replacements have also been studied using automated markerless RSA techniques.

Ethical approval to implant beads into bone is often only given if surgery on the joint under study is already medically required, which limits the use of standard RSA to those with pathology of some type. One of the greatest advantages of markerless RSA is that normal skeletal kinematics can be studied, without the requirement of bead implantation. Nishinaka *et al.* (2008) used a single-plane markerless RSA technique to study *in vivo* glenohumeral translation in subjects with no history of shoulder injury or signs of pathology. Other groups have also studied knee kinematics during normal walking (Komistek *et al.*, 2003), treadmill walking (Li *et al.*, 2008) and running (Anderst *et al.*, 2009). Other recent studies have ranged from investigating intervertebral disc deformation under weight bearing conditions (Wang *et al.*, 2009) to analyzing healthy ankle kinematics in various positions (Yamaguchi *et al.*, 2009).

Since markerless RSA allows easier access to a normal subject population, researchers can compare injured or reconstructed joints to the normal contralateral sides or an independent normal population. This technique is becoming especially popular as a method to analyze ACL tears and reconstructions. More specifically, the effect of ACL deficiency on knee kinematics (Mahfouz *et al.*, 2004) and on the elongation of other ligaments in the knee (Van de Velde *et al.*, 2007) has been analyzed. In the shoulder, glenohumeral joint translation in subjects following arthroscopic rotator cuff repair has been studied, using subjects' contralateral shoulders as controls (Bey *et al.*, 2008). The aforementioned applications of markerless RSA suggest that this method has gained the

reputation of being a suitable alternative for standard RSA, with the significant advantage of avoiding surgery to implant beads.

1.3 ALGORITHMS

At the present time there are two main categories of RSA: standard RSA and markerless RSA. These RSA variations utilize similar equipment and components; however, the algorithms and procedures required for each vary drastically. Each form of RSA can either be performed in a single plane or dual plane set-up. The algorithms used in the dual plane setting will be focused upon, since this set-up is used in the Wolf Orthopaedic Quantitative Imaging Laboratory (WOQIL), where the research for this thesis was conducted.

1.3.1 STANDARD RSA

The algorithm that is currently used to perform standard RSA in the WOQIL has been previously described (Kedgley *et al.*, 2009b; Kedgley & Jenkyn, 2009c) and is based on the work of Selvik (Selvik, 1989). A brief outline of the standard RSA algorithm will be given since the algorithm is used as part of the markerless RSA calibration.

A calibration frame is used to determine the position of the two x-ray foci in the laboratory coordinate system and the necessary parameters to compute the 3D positions of markers. The calibration frame is composed of two fiducial planes and two control planes that are embedded with fiducial markers and control markers, respectively. The calibration frame is oriented so that each x-ray device images one fiducial plane and one control plane (Figure 1.1).

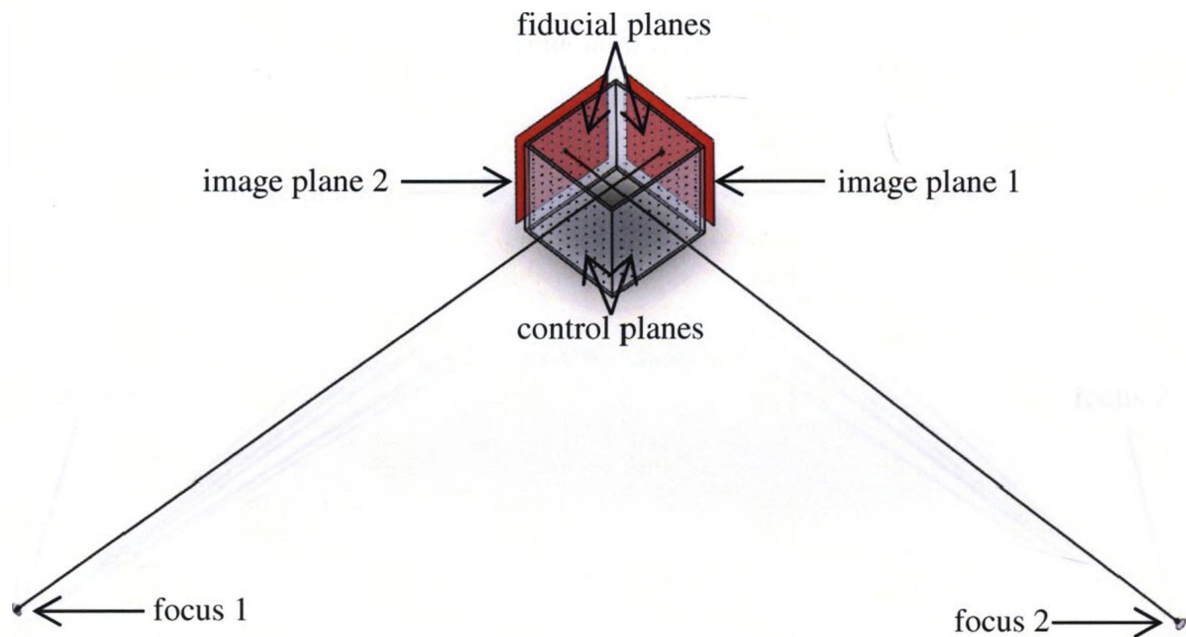


Figure 1.1: Biplanar RSA calibration set-up

Typical biplanar RSA calibration set-up including the x-ray foci, calibration frame and image planes (in red).

The fiducial markers define the laboratory coordinate system and they are also used to generate parameters necessary to compute the projective transformation. The projective transformation transforms image coordinate points to laboratory coordinate points, by projecting points on the image onto the fiducial plane.

The control points are used to calculate the position of each x-ray focus. Using the projective transformation, control points are projected onto each corresponding fiducial plane. Lines connecting each control point and its projection onto the corresponding fiducial plane are extended. The intersection of these extended lines defines the x-ray foci (Figure 1.2). Due to errors, these lines rarely intersect, so a least squares method is used to estimate each focus.

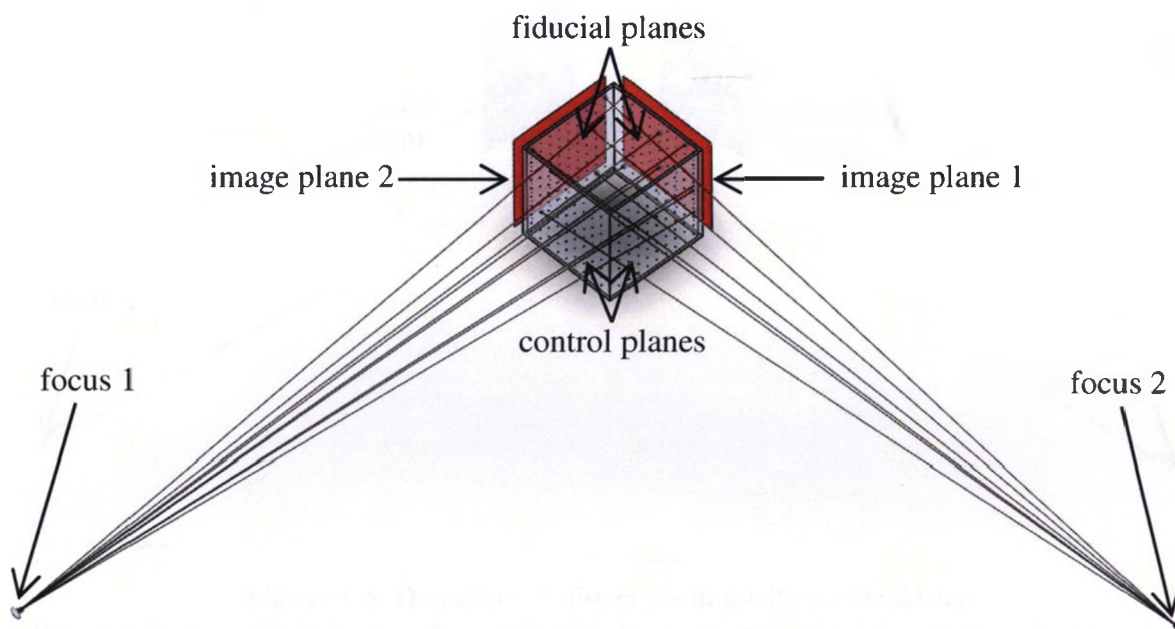


Figure 1.2: Depiction of foci position calculation

Illustration of a biplanar RSA calibration set-up including x-ray foci, calibration frame and image planes (in red). X-rays emanating from the foci are illustrated passing through the control and fiducial planes and producing corresponding images on the image planes.

The projective transformation is used again to determine the 3D position of object markers in the laboratory coordinate system. A line connecting the focus and the projection of an object point on the fiducial plane is calculated for each image. The position of the object point lies at the intersection of these lines, which is also computed using a least squares method (Figure 1.3). Once the position of three, non-linear object points have been determined a coordinate system can be defined, allowing the pose of the object to be determined.

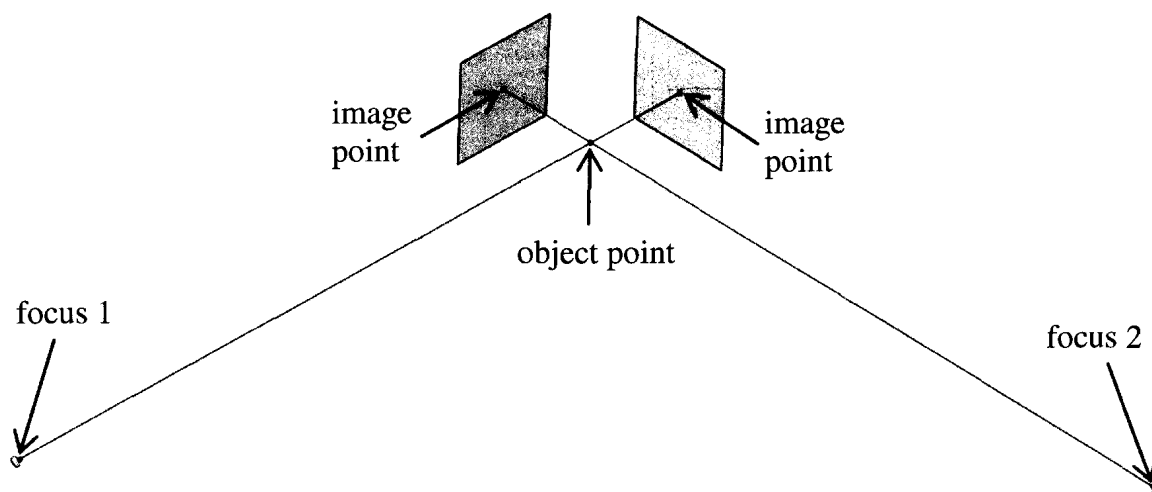


Figure 1.3: Depiction of object point position calculation

Biplanar RSA model indicating the relationship between an object point, and its corresponding image point on each image plane.

1.3.2 MARKERLESS RSA

Markerless RSA is based on matching the projected silhouette of a 3D computer model to the outline of the object as viewed on radiographic images (Figure 1.4). Therefore, in order to perform markerless RSA, a reconstruction of the experimental set-up is required, specifically the position of the x-ray foci and poses of the image planes. As with standard RSA, a calibration frame, with fiducial and control planes is used to calibrate the system. Unlike standard RSA, however, the calibration algorithms used to reconstruct the geometry of the experimental set-up have not been well documented in the literature. The standard RSA algorithm can be used to determine the position of the x-ray foci, but the orientation of the image planes and distance between image plane and x-ray foci still need to be determined. A 3D computer model of the object must also be created, which is usually done through computed tomography (CT) scans, magnetic resonance imaging (MRI) or pre-existing computer aided design (CAD) models, if the object is a prosthetic component.

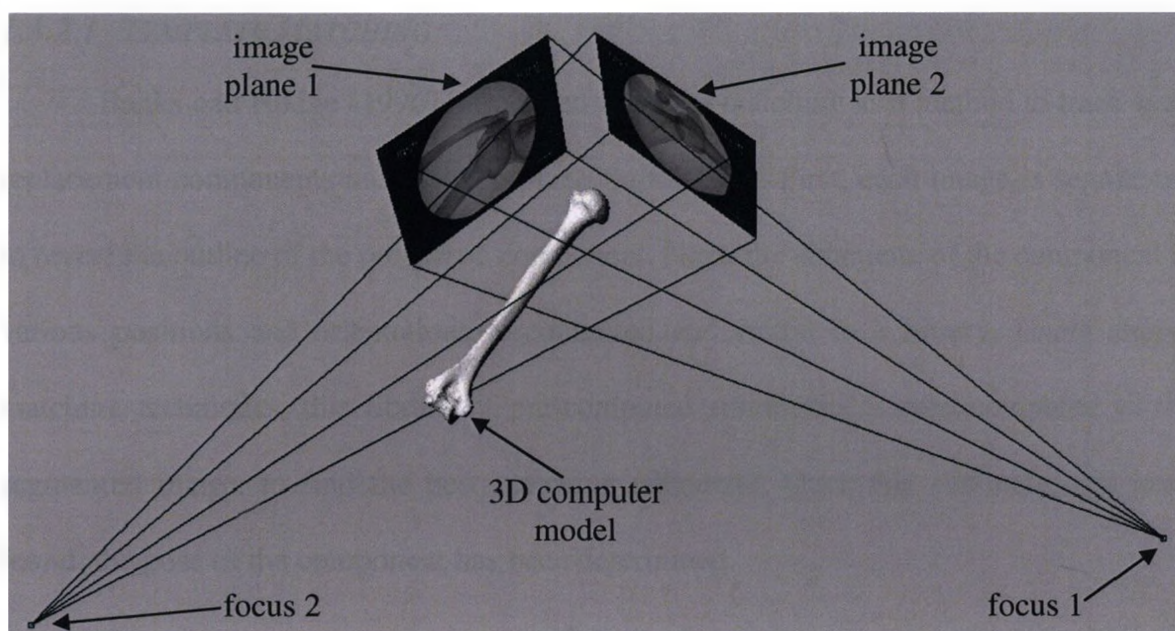


Figure 1.4: Markerless RSA experimental set-up

Virtual model of markerless RSA experimental set-up including x-ray foci, image planes, and computer model of the humerus.

Manual and automated methods exist to match the 3D computer models to the images. Manual methods consist of an operator rotating and translating the 3D object until they consider the projected silhouette to match the outlines on the images (Asano *et al.*, 2001; Li *et al.*, 2004). Various automated methods also exist, which significantly reduce the processing time for an operator (Kaptein *et al.*, 2003; You *et al.*, 2001; Banks & Hodge, 1996). These automated methods of performing markerless RSA can be divided into two main categories: template matching (Banks & Hodge, 1996) and hypothesis and test methods (Kölzow & Krüger, 2002). For automated methods, it is almost always necessary to segment the image to detect the contour of the object in the radiograph. This segmentation is usually done through an edge detection algorithm, such as Canny edge detection (Canny, 1986).

1.3.2.1 *TEMPLATE MATCHING*

Banks and Hodge (1996) introduced template matching as a method to track knee replacement components using single-plane fluoroscopy. First, each image is segmented to reveal the outline of the prosthetic component. Next, the silhouette of the component in various positions and orientations is computed and stored in a library. Using shape-matching techniques, this library of pre-computed silhouettes is then compared to the segmented image, to find the best matching silhouette. Once this silhouette has been found, the pose of the component has been determined.

1.3.2.2 *HYPOTHESIS AND TEST METHOD*

The hypothesis and test method is based on hypothesizing the ideal pose of an object and then testing this hypothesis by using the radiographic images of the object. This cycle of hypothesizing and testing is repeated until a minimal difference between predicted and actual data is found. For this method, the first pose of the object is usually set by an operator. Optimization routines are then used to successively determine better hypotheses for the pose of the object. Groups have used optimization routines such as feasible sequential quadratic programming (Valstar et al., 2001), Levenberg–Marquardt nonlinear least squares method (Zuffi *et al.*, 1999) and the downhill Simplex method (You *et al.*, 2001).

The main variation in hypothesis and test methods, however, lies in the choice of an objective function, which is used to test the validity of the hypothesis. The objective function returns a value, which when minimized, results in the optimal match of the 3D computer model silhouette to the radiographic image, revealing the pose of the object. There are four main objective functions used in markerless RSA: non-overlapping area

(NOA), iterative closest point (ICP), iterative inverse point (IIP) and digitally reconstructed radiographs (DRR) (Bingham, 2006).

Non-overlapping Area

To perform the NOA optimization, the silhouette of the 3D computer model is projected onto the radiograph to form a calculated model contour, which is then compared with the detected contour of the object on the radiograph. As described by Valstar *et al.* (2001), “The NOA is defined as the area that the detected contour and the calculated model contour do *not* have in common”. Once the NOA is minimized, the projected silhouette should most closely match the detected contour, corresponding to the ideal pose of the object.

In a study conducted by Valstar *et al.* (2001), they found that the NOA algorithm did not satisfy the accuracy requirements of markerless RSA to study knee implant components. The NOA algorithm was too sensitive to the large dimensional tolerances of the generic CAD models used. One method to solve this problem is to remove the unreliable parts of the contour resulting from inaccuracies of the model; however, the NOA algorithm cannot be employed with contour drop-outs.

Kaptein *et al.* (2004) conducted a study to compare the accuracies of the NOA, ICP and IIP algorithms to study knee implant components (Kaptein *et al.*, 2004). They again found that the NOA algorithm was not sufficiently accurate, mainly due to the algorithm’s poor performance when the number of points in the actual contour is decreased and the size of drop-outs is increased. In order to use the NOA algorithm with drop-outs, the end points of a drop-out section were connected with a straight line. The

algorithm, however, could prove to be sufficiently accurate when studying skeletal kinematics, since a unique 3D model is usually created for each object under study, thereby eliminating contour drop-outs and minimizing 3D computer model inaccuracies.

Iterative Closest Point

The ICP algorithm minimizes the distance between two contours: the projected contour by the 3D computer model and the detected contour on the radiograph (Kaptein *et al.*, 2003). More specifically, both contours are first defined as a chain of nodes. Next, the shortest distance between each node on the detected contour and the calculated projected contour is computed. The mean value of these distances is minimized to find the ideal pose of the object.

Iterative Inverse Point

The IIP algorithm is based on the fact that contour points on the x-ray image are formed when the x-rays are tangent to the edge of the object. The first step in the IIP algorithm is to create a line from the x-ray focus to points on the detected contour. When the distance between these lines and the 3D model surface is minimized, the lines will be tangent to the 3D computer model and the ideal pose of the object will be recovered (Kaptein *et al.*, 2004; Zuffi *et al.*, 1999).

Digitally Reconstructed Radiographs

Algorithms that use digitally DRRs are also referred to as intensity-based methods, since these methods not only utilize the outer surface of the 3D model, but

mainly rely on the intensity or texture information contained in the entire volume. A DRR is a simulated image, which is created by generating a projection through a 3D volumetric model of an object, based on the object's texture and rough outline (You *et al.*, 2001). The DRR is compared to actual radiographs taken of the object using image matching techniques. When similarities between the DRR and the radiographs are maximized, the object's pose has been determined.

It should be noted that automated methods, excluding methods based on DRR, were used to first study knee implant kinematics (Banks & Hodge, 1996; Dennis *et al.*, 1996; Hoff *et al.*, 1998) and have only more recently been used to track skeletal kinematics (Komistek *et al.*, 2003; Nishinaka *et al.*, 2008). This delay in studying skeletal kinematics is in part due to the challenge of segmenting images of bones. Based on the principal of gradients, the images are segmented in order to obtain outlines of objects, also referred to as edge detection. This process works well for implants, due to the high-contrast and well-defined edges created by the metallic components. However, it is more difficult to segment images of bones because there is less contrast and more interference due to soft-tissue (You *et al.*, 2001). Since algorithms based on DRR rely mainly on the texture of the object, as opposed to the outline of the object, these methods have been used to analyze skeletal kinematics since their inception in the field of biomechanics (You *et al.*, 2001).

1.3.2.3 MANUAL MATCHING

Manual methods rely on an operator rotating and translating a 3D object until they consider that the projected silhouette matches the outlines on the images. These methods are much simpler to employ than automated routines and have also been used

successfully to analyze skeletal kinematics. In 2001, Asano *et al.* developed a markerless RSA method that continues to be used to study knee kinematics (Asano *et al.*, 2005). Li *et al.* (2004) has also developed a method based on manual matching that has been used extensively in many areas such as the knee (Li *et al.*, 2008), spine (Wang *et al.*, 2009) and ankle (de Asla *et al.*, 2006).

1.4 EXPERIMENTAL SET-UP

Each RSA method can either be conducted in a single or dual plane environment, depending on the number of x-ray machines used to image the object under study. A dual plane set-up can further be subdivided into a uniplanar or biplanar set-up, depending on the orientation of the x-ray foci and recording media

1.4.1 SINGLE PLANE

The main limitation of a single plane setting is reduced depth perception, which leads to decreased accuracy in the direction perpendicular to the image plane (out-of-plane movement). Numerous studies have evaluated the accuracy in the out-of-plane direction, which is usually an order of magnitude worse than accuracies in the in-plane direction (Banks & Hodge, 1996; Fregly *et al.*, 2005). Figure 1.5 depicts a typical single plane RSA set-up.

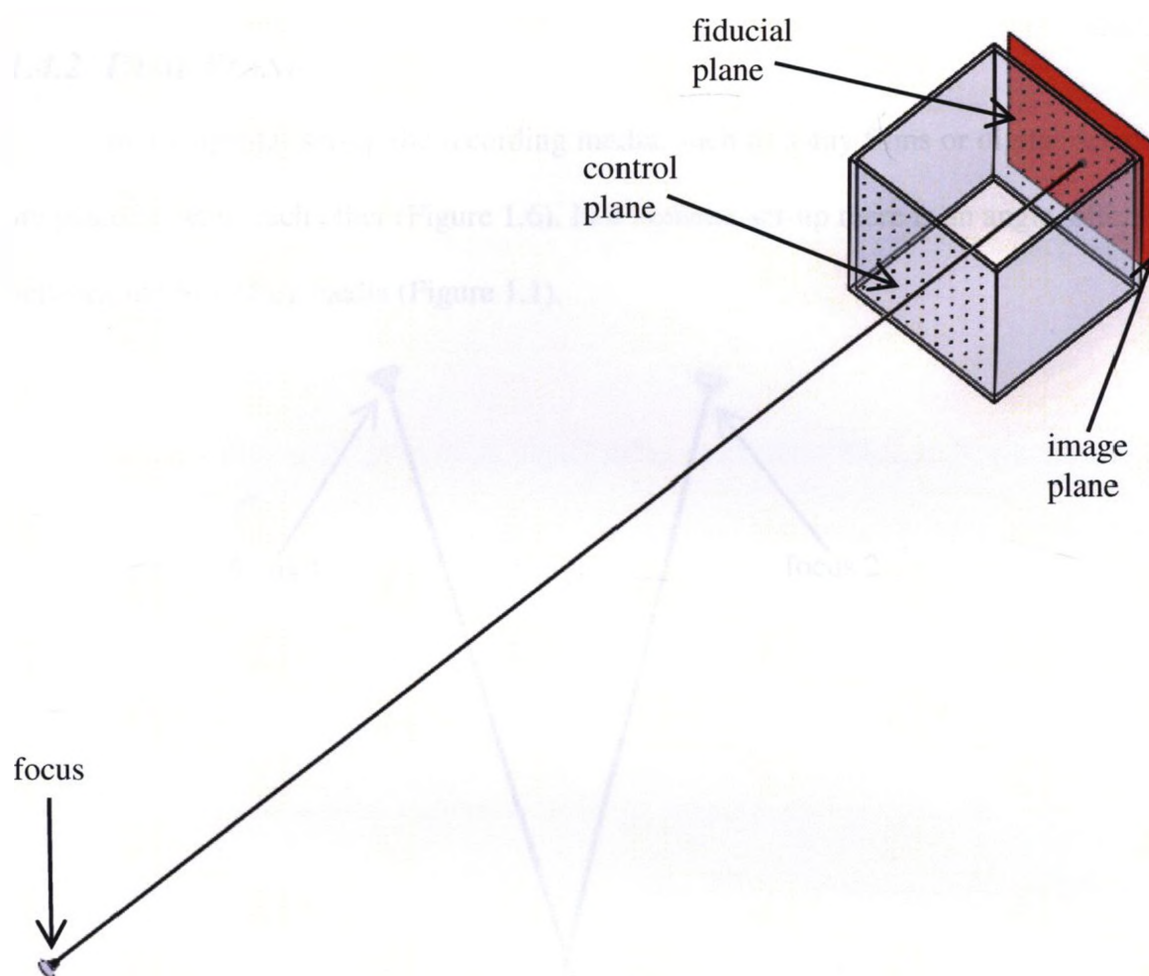


Figure 1.5: Single plane RSA calibration set-up

Single plane RSA calibration set-up including the x-ray focus, control plane, fiducial plane and image plane (in red).

1.4.2 DUAL PLANE

In a uniplanar set-up the recording media, such as x-ray films or digital detectors, are placed next to each other (Figure 1.6). In a biplanar set-up there is an angle, often 90° , between the recording media (Figure 1.1).

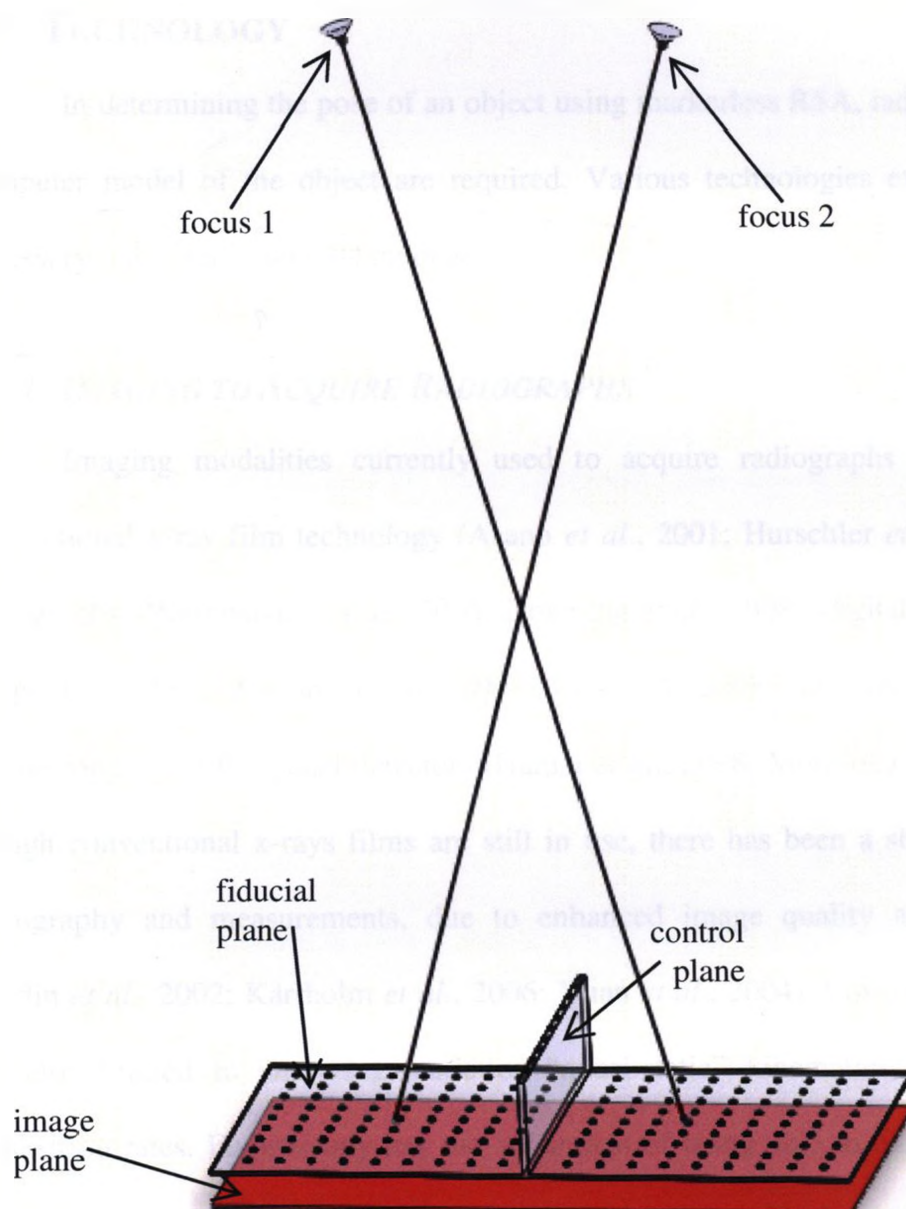


Figure 1.6: Uniplanar RSA calibration set-up
Uniplanar RSA calibration setup including the x-ray foci, fiducial plane, control plane and image planes (in red).

An advantage of a dual plane environment is that there is no loss of accuracy for out-of-plane movement, since out-of-plane movement in one view is in-plane-movement in another view. A disadvantage of a biplanar set-up, however, is that joint movement can be restricted due to the constrained environment imposed by the imaging technology.

1.5 TECHNOLOGY

In determining the pose of an object using markerless RSA, radiographs and a 3D computer model of the object are required. Various technologies exist to acquire the necessary radiographs and 3D models.

1.5.1 IMAGING TO ACQUIRE RADIOGRAPHS

Imaging modalities currently used to acquire radiographs for RSA include conventional x-ray film technology (Asano *et al.*, 2001; Hurschler *et al.*, 2009), digital radiography (Berthonnaud *et al.*, 2005; Downing *et al.*, 2008), digital fluoroscopy using image intensifiers (Garling *et al.*, 2004; Li *et al.*, 2008), and more recently digital fluoroscopy using flat-panel detectors (Hamai *et al.*, 2008; Moro-oka *et al.*, 2007). Even though conventional x-rays films are still in use, there has been a shift towards digital radiography and measurements, due to enhanced image quality and RSA accuracy (Börlin *et al.*, 2002; Kärrholm *et al.*, 2006; Yuan *et al.*, 2004). Conventional x-ray films are also limited to analyzing static or “quasi-static” kinematics, due to their low acquisition rates. Fluoroscopy has the advantage of being able to capture true dynamic motion due to the technology’s high-acquisition rate, 30 frames/second or higher (Bushberg *et al.*, 2002). Since the input screens of the image intensifiers are curved and the output surfaces are flat, images with pincushion distortion result (Bushberg *et al.*,

2002). A main advantage of the new flat-panel fluoroscopes is that the images are distortion-free (Yaffe *et al*, 1997). Fluoroscopes with image intensifiers will be described in more detail, since two fluoroscopy units, (SIREMOBIL Compact (L), Siemens Medical Solutions, USA Inc., Malvern, PA, USA) at the WOQIL were used to acquire the radiographs for this thesis.

1.5.1.1 FLUOROSCOPY

The goal of fluoroscopy systems is to enable low-dose, real-time x-ray viewing. In order to capture the large number of images required to depict motion, without increasing the radiation dosage, an extremely sensitive detector is needed. The image intensifier (II) produces usable radiographs, but uses much fewer x-rays, due to its increased sensitivity. The II is the main component that distinguishes fluoroscopy from radiography. (Bushberg *et al.*, 2002)

The entire fluoroscopy imaging chain consists of several linked components (Figure 1.7). An x-ray tube produces x-rays of varying energy, depending on the applied voltage. Next, a series of filters remove low-energy x-rays, which would otherwise significantly increase the dosage. After filtration, the x-rays emerge in many different directions, so a collimator is used to restrict the x-rays into a useful beam. The x-rays are then attenuated to varying degrees depending on the material composition of the object under study. The image intensifier converts the resulting x-rays into a light image, which is focused onto the focal plane of a video camera using lenses. The video camera then outputs the images to a video monitor. (Bushberg *et al.*, 2002; Hendee & Ritenour, 2002)

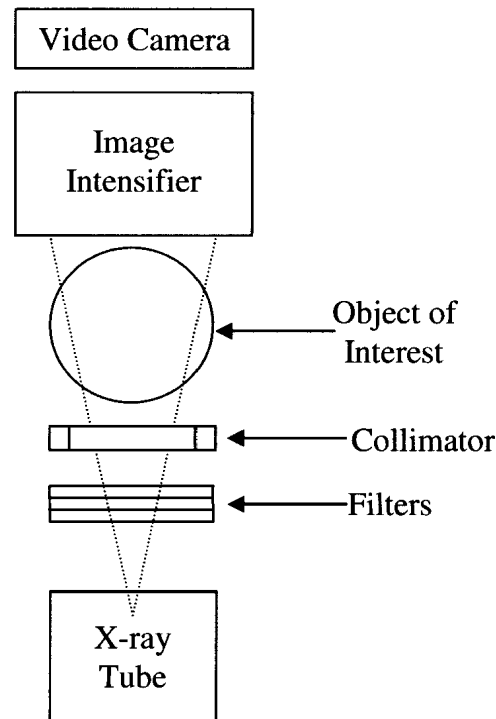


Figure 1.7: Components of a fluoroscope

Block diagram of a typical fluoroscope system including the x-ray tube, filters, collimator, image intensifier and video camera. The object of interest is positioned between the collimator and image intensifier.

1.5.2 METHODS TO CREATE 3D COMPUTER MODELS

Research groups have created and obtained 3D computer models using various methods such as CT (Asano *et al.*, 2001; Komistek *et al.*, 2003), MRI (de Asla *et al.*, 2006), pre-existing CAD models (Bingham & Li, 2006; Valstar *et al.*, 2001) and laser scanning (Kaptein *et al.*, 2006; Mahfouz *et al.*, 2003).

CT and MRI both create a series of images, which require further processing to be transformed into 3D models. For CT, x-rays are passed through the object of interest by rotating the x-ray tube and detector around an object. Data are then synthesized by a computer to create radiograph slices through the object. Unlike CT, MRI does not use x-rays, but a powerful magnetic field to create image slices based on the micromagnetic properties of the object. (Bushberg *et al.*, 2002)

MRI has the significant advantage of avoiding ionizing radiation; however, it is more difficult to create bone models from MRI-derived images, due to the low bone contrast. Images derived from CT are easier to segment, but subjects must be exposed to radiation. In a study conducted by Moro-oka *et al.* (2007), it was found that markerless RSA results were significantly more accurate when using CT-derived bone models, than MRI-derived bone models.

Other methods to obtain 3D computer models rely on using generic CAD models from manufacturers and laser scanning to reverse engineering unique models. These methods, however, cannot be used to create *in vivo* bone models.

1.5.2.1 COMPUTED TOMOGRAPHY OVERVIEW

Due to the availability of the technology and increased markerless RSA accuracy, CT was used to create the 3D computer models for this thesis. A brief outline of CT technology will therefore be given, but the specific details regarding image segmentation to create the 3D models will be provided in Chapter 2.

CT produces cross-sectional images of an object using multiple x-ray transmissions through the object and computer algorithms (Figure 1.8). For helical CT scanning, also referred to as spiral CT scanning, an x-ray tube and an array of detectors are mounted to a gantry, which rotates around the object of interest. As the gantry rotates, the object is translated through it, resulting in a helix pattern of relative motion. (Hendee & Ritenour, 2002; Micheal, 2001)

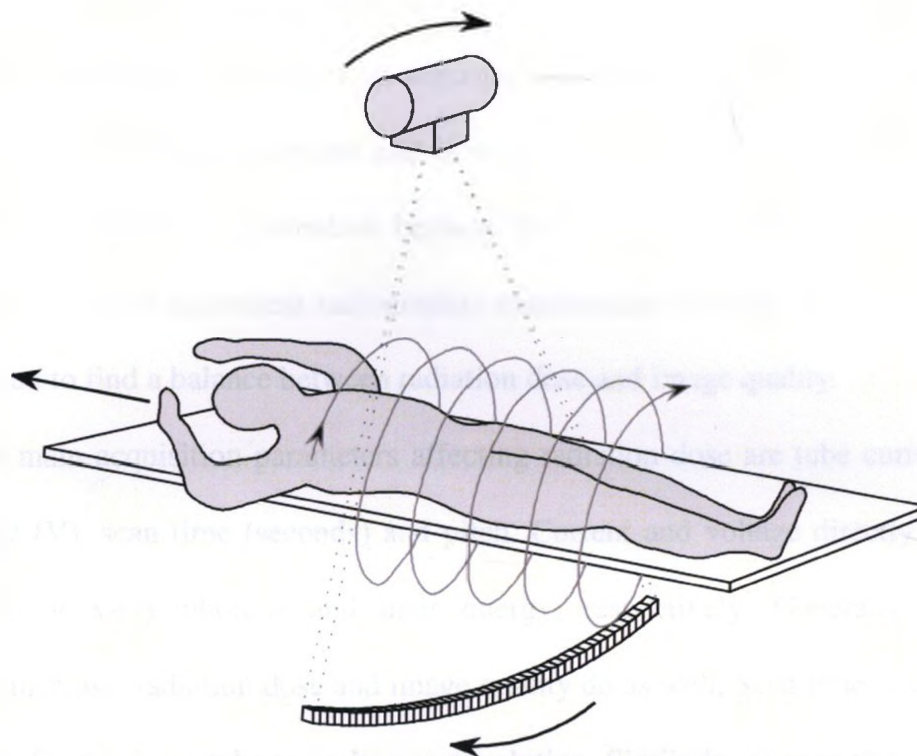


Figure 1.8: Helical computed tomography

Reprinted from Michael, G. (2001). X-ray computed tomography. *Medical Physics*, 36(6), 442-451., with permission from IOP Publishing Ltd.

The x-ray tube produces x-rays, which are then filtered to create a beam with a more uniform intensity. Collimators are used after x-ray production and again before the x-rays reach the x-ray detector. The source collimator controls the shape of the beam and limits the dosage. After transmission through the patient, the x-ray beam is further collimated to control the slice thickness and reduce scattering. The x-ray detector(s) do not directly produce an image; instead, they make measurements through a chosen slice in various directions. With these measurements, there are then various methods to reconstruct the images mathematically, all relying heavily on computer algorithms. (Hendee & Ritenour, 2002; Micheal, 2001)

1.5.2.2 COMPUTED TOMOGRAPHY DOSAGE

Due to the risks associated with ionizing radiation, it is important to understand what factors affect CT x-ray dosage and how dosage is measured and monitored. CT scanning also requires extra attention because the radiation dosage for a CT scan is greater than that of an equivalent radiographic examination (Hendee & Ritenour, 2002). It is important to find a balance between radiation dose and image quality.

The main acquisition parameters affecting radiation dose are tube current (mA), tube voltage (V), scan time (seconds) and pitch. Current and voltage directly influence the number of x-ray photons and their energy, respectively. Generally, as these parameters increase, radiation dose and image quality do as well. Scan time refers to how long it takes for the x-ray tube to make one revolution. Similarly, as scan time increases, so do radiation dose and image quality.

Pitch can be defined in terms of beam pitch (also referred to as collimator pitch) and slice pitch (also referred to as detector pitch). For CT scanners with one detector, beam pitch is equal to slice pitch; however, for CT scanners with multiple detector arrays, there are numerous slices taken in a single x-ray beam, so these pitch values are not equal. (Bushberg *et al.*, 2002; Silverman *et al.*, 2001)

Beam pitch is defined as:

$$\text{Beam pitch} = \frac{\text{table movement (mm) per } 360^\circ \text{ of gantry rotation}}{\text{beam width (mm)}} \quad (\text{Eq. 1.1})$$

Slice pitch is defined as:

$$\text{Slice pitch} = \frac{\text{table movement (mm) per } 360^\circ \text{ of gantry rotation}}{\text{slice width (mm)}} \quad (\text{Eq. 1.2})$$

A low pitch results in improved spatial resolution and increased dosage. Conversely, a high pitch results in decreased spatial resolution and dosage.

Dosage is measured in terms of a CT dose index (CTDI) and dose length product (DLP). The CTDI measures scattered radiation dose from adjacent CT slices in mGy, the SI unit of absorbed radiation dose due to ionizing radiation. The DLP is a measure of total radiation exposure for the entire series of images, measured in mGy·cm. (Bushberg *et al.*, 2002)

1.6 SHOULDER COMPLEX

The shoulder, in both model and cadaveric form, was used as the validation and application site for the work described in this thesis. Therefore, a brief description of the anatomy and kinematics of the shoulder will be given, with focus on the humerus, scapula and glenohumeral joint.

The shoulder's function is to connect the arm to the thorax (trunk) and to position the hand in space, with the help of the elbow (Della Valle *et al.*, 2001). With few bony constraints, the shoulder is the most mobile joint in the human body (Bahk *et al.*, 2007).

1.6.1 ANATOMY

The shoulder complex (Figure 1.9) is comprised of three bones: the humerus (upper arm bone), scapula (shoulder blade) and clavicle (collarbone). Together with the thorax, they form three anatomical joints, (the glenohumeral joint, acromioclavicular, sternoclavicular joints) and two functional joints (scapulothoracic and subacromial joints) (Itoi *et al.*, 1996; Nobuhara, 2003). The anatomical joints are true synovial joints, whereas the functional joints are not, but still describe relative motion between two anatomical structures.

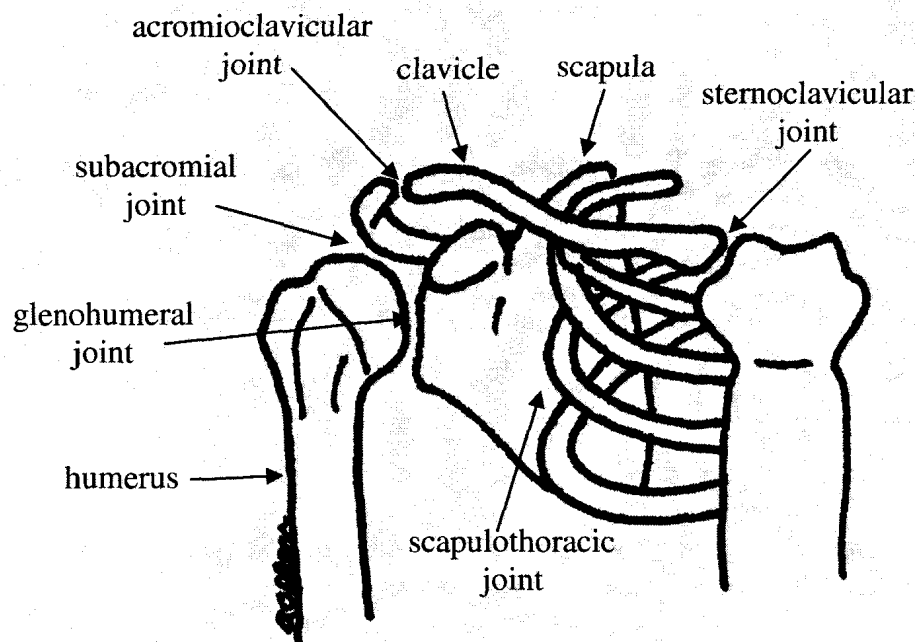


Figure 1.9: Shoulder complex

Diagram of the shoulder complex with humerus, scapula, clavicle and main articulations labeled.

1.6.1.1 BONES

The humerus provides a link between the elbow and the scapula. It is a cylindrical long bone with a hemispheric type form on its superior end, which is directed posteriorly (Nobuhara, 2003). The hemispheric form, also referred to as the humeral head, is covered with cartilage and articulates with the glenoid fossa of the scapula.

The scapula is a triangular flat bone with thick edges and a thin central portion (Prescher, 2000). It is located on the posterior and lateral section of the shoulder girdle and links the clavicle with the humerus. An important function of the scapula is to provide muscle attachment sites (Lugo *et al.*, 2008).

An essential anatomic feature of the scapula is the glenoid fossa, as it is the site of articulation with the humerus. The glenoid fossa is a shallow, pear-shaped cavity located on the lateral side of the scapula. The glenoid labrum is a fibrocartilaginous material that lines the periphery of the glenoid fossa (Della Valle *et al.*, 2001). This added material deepens the glenoid fossa, also increasing the stability and congruity of the glenohumeral joint (Lugo *et al.*, 2008).

The clavicle is a short s-shaped bone, ranging from extremely curved to almost straight in the healthy population (Prescher, 2000). It acts as a strut between the thorax and the scapula, and is an attachment site for many of the muscles acting on the shoulder (Della Valle *et al.*, 2001).

1.6.1.2 ARTICULATIONS

The overall movement of the shoulder complex can be decomposed into five separate articulations: the sternoclavicular, acromioclavicular, scapulothoracic,

subacromial and glenohumeral joints. As only glenohumeral kinematics are calculated in this thesis, only point form descriptions of the other joints will be provided as follows:

Sternoclavicular joint – anatomical joint; attaches the medial end of the clavicle to the thorax via the manubrium, which is superior part of the sternum (Della Valle *et al.*, 2001).

Acromioclavicular joint – anatomical joint; connects the lateral end of the clavicle with the acromion of the scapula (Della Valle *et al.*, 2001).

Scapulothoracic joint – functional joint; consists of the scapula gliding on the thorax (Nobuhara, 2003)

Subacromial joint – functional joint; space between the coracoid process, acromion and humeral head (Nobuhara, 2003)

In the shoulder complex, the glenohumeral joint is the most important joint, defined by the articulation between the humeral head and glenoid fossa of the scapula. This joint is similar to a ball and socket joint, except that the socket is too small and shallow for the large ball to fit into securely (Culham & Peat, 2003). This bony set-up is inherently unstable, so the shoulder is mainly stabilized by the muscles, ligaments and tendons surrounding the joint. With few bony constraints, the glenohumeral joint has the largest range of motion (ROM) of all the joints in the human body (Prescher, 2000).

1.6.2 KINEMATICS

1.6.2.1 BASIC MOVEMENTS

Shoulder movements can be decomposed into three basic movement pairs: abduction and adduction, flexion and extension, and internal and external rotation (Figure 1.10). Abduction and adduction is the movement of the humerus in the coronal plane away from and towards the thorax, respectively. Flexion and extension is the movement of the humerus in the sagittal plane outwards to the front and outward to the back, respectively. Internal and external rotation is the axial rotation of the humerus about its long axis with the anterior aspect moving medially and laterally, respectively.

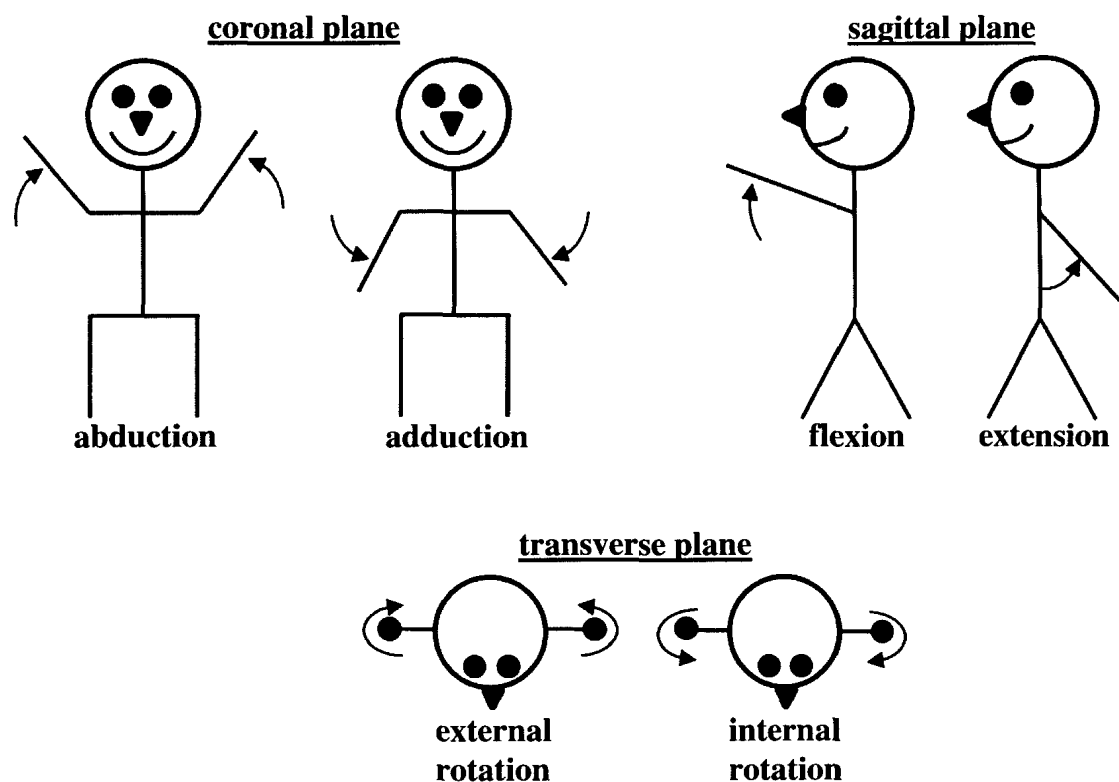


Figure 1.10: Basic shoulder movements

Illustration of basic shoulder movements of interest in this study, including abduction and adduction, flexion and extension and internal and external rotation.

1.6.2.2 ANATOMICAL COORDINATE SYSTEMS

The work in this thesis relies on calculating glenohumeral joint kinematics; therefore, it is necessary to determine the movement of the humerus with respect to the scapula. It was chosen to use conventions established by the International Society of Biomechanics (ISB) when calculating anatomically based coordinate systems, as well as when reporting kinematics (Wu *et al.*, 2008).

Anatomical coordinate systems are created using bony landmarks, which are repeatable and distinguishing points found on each bone. If the same landmarks are used, anatomical coordinate systems allow for the consistent creation of coordinate systems, which can then be easily compared. In order to create its anatomical coordinate system at least three non-colinear points are required for each bone.

In accordance with the ISB conventions, kinematics are reported in terms of a translation and an Euler angle representation. Euler angles are a method used to define the orientation of one object with respect to another, using three sequence-dependent rotations.

1.7 STUDY RATIONALE

Standard RSA is a well-established and accurate method to calculate 3D skeletal kinematics. It is the “gold standard” for tracking prosthetic loosening and joint kinematics on a micromotion level. A standard RSA system has been successfully developed and validated in the WOQIL (Kedgley *et al.*, 2009b; Kedgley & Jenkyn, 2009c). As with all standard RSA systems, the inherent limitation is that beads must be surgically implanted into the bones under study. Clinical research is then limited to subjects with existing pathology, since in many countries ethical approval for the

implantation of beads will only be granted if the subject is already undergoing surgery on the joint to be analyzed. In this situation, standard RSA cannot be used to analyze the joint kinematics of a normal subject population or compare pre- and post-surgical kinematics. Even if all of the necessary imaging equipment is available, standard RSA is not likely to ever be practical for routine clinical practice. The development of a markerless RSA system will eliminate many of the current limitations in the WOQIL, allowing for a broader scope of clinical research to be conducted.

1.8 OBJECTIVES AND HYPOTHESIS

The specific objectives of this thesis were to:

- 1) Develop a biplanar fluoroscopic markerless RSA system to study skeletal kinematics in the glenohumeral joint,
- 2) Validate the accuracy of the markerless RSA system using a precision sliding table and standard RSA,
- 3) Analyze the affect of CT dosage on the *in vitro* accuracy of markerless RSA

The main hypothesis of this thesis was that a markerless RSA system could be successfully developed with accuracies comparable to other similar markerless RSA systems reported in the literature. It was also hypothesized that the accuracy of markerless RSA would decrease as the CT dosage decreased.

1.9 OVERVIEW

This thesis is comprised of six chapters. Chapter 1 provided an introduction to RSA and the overall rationale of this work. Chapter 2 describes the development of a markerless RSA system. Chapter 3 details the protocols used to validate the markerless RSA system and investigates the effect of CT dosage on markerless RSA accuracy. Chapter 4 provides the results, which are then discussed in Chapter 5. The thesis finishes with Chapter 6, which details the conclusions of this work as well as comments on the limitations, strengths and recommendations for future directions of this research.

CHAPTER 2 – DEVELOPMENT OF A MARKERLESS RSA SYSTEM

OVERVIEW: This chapter details the steps taken in the development of a markerless RSA system, specifically the calibration, experimental set-up recreation, 3D model creation and matching. A calibration algorithm was employed to determine the necessary parameters to recreate a virtual experimental set-up. CT images were segmented to create 3D computer models, which were then imported into the virtual environment. The models were manually matched to the radiographs, until a minimization between model silhouette and outlines on the images was achieved.

2.1 INTRODUCTION

The main goal of the markerless radiostereometric analysis (RSA) system is to track skeletal kinematics using two fluoroscopes, without requiring the insertion of beads into the bones of interest. In order to achieve this goal, a system was developed that is based on matching two silhouettes of a three-dimensional (3D) computer model to two radiographs taken simultaneously of the object from different directions. A calibration technique was used to determine the experimental set-up parameters, specifically the x-ray foci locations and the image plane poses. Using these parameters, a virtual environment was created in which the fluoroscope foci and radiographs were accurately positioned. The 3D computer model, created from computed tomography (CT) scans, was then imported into the virtual environment and manually adjusted in 3D space until its projections from the points of view of the two x-ray foci matched the radiographs. Figure 2.1 represents a flow diagram of the markerless RSA procedure developed in this thesis.

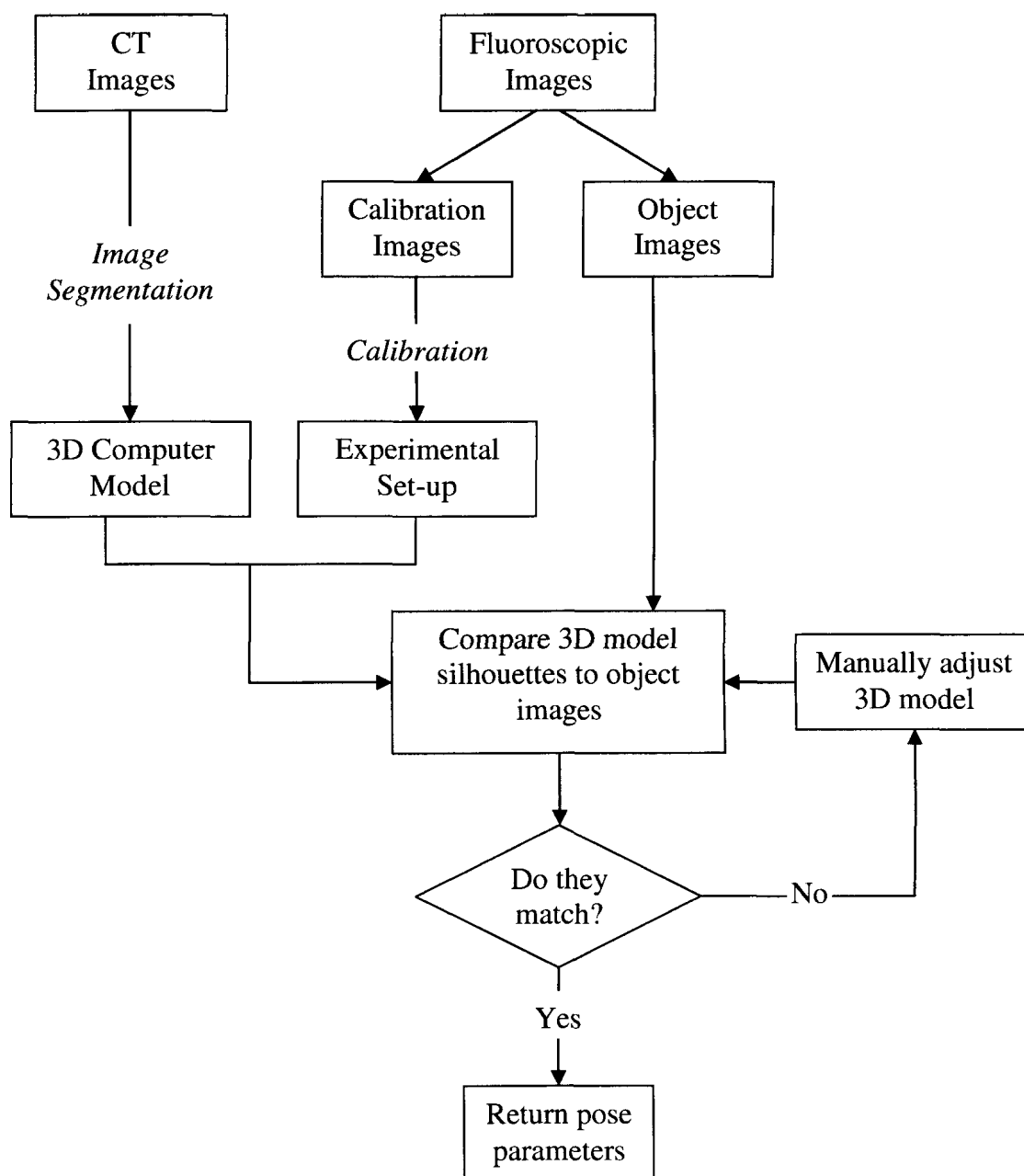


Figure 2.1: Markerless RSA flow diagram

Markerless RSA workflow diagram illustrating the process consists of three basic steps: 3D model generation, system calibration and object image matching and analysis.

2.2 CALIBRATION

X-ray calibration is typically performed by imaging a calibration phantom with embedded beads at known locations. A calibration algorithm is used to determine a relationship between the 3D locations of beads and the two-dimensional (2D) images taken of the beads. This relationship is then used to calculate the parameters necessary to reconstruct the experimental set-up.

A frame, designed by Kedgley, was used as the calibration phantom for this thesis (Kedgley, 2009a; Kedgley *et al.*, 2009b). The frame defined the laboratory coordinate system and was used to determine the experimental set-up parameters. The x, y and z axes are coloured in red, green and blue, respectively in Figure 2.2.

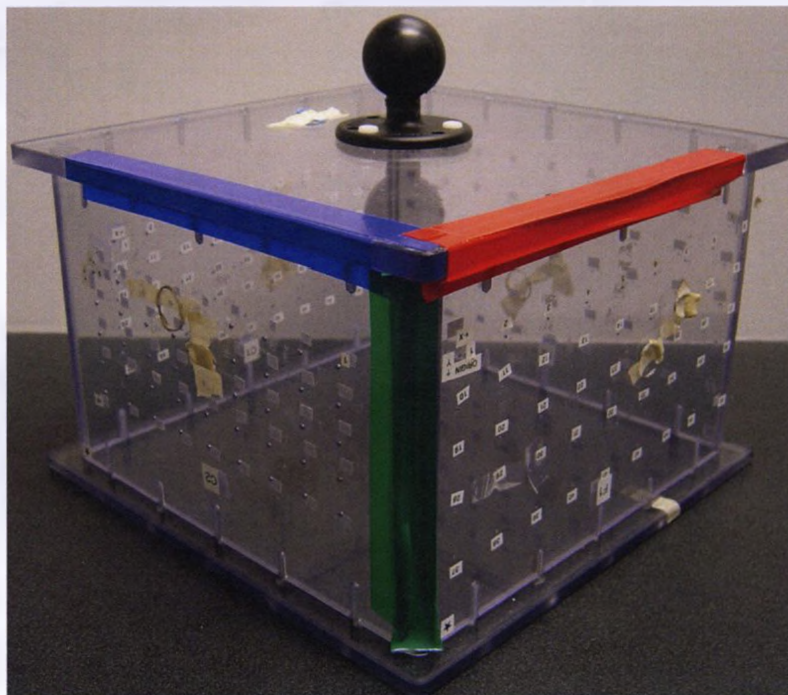


Figure 2.2: Calibration frame showing the x, y, and z axes in red, green and blue respectively

Images of the calibration frame were digitized and corrected for image distortion. Distortion correction was performed by first imaging a distortion grid with beads embedded at known locations. This grid was also designed by Kedgley (Kedgley, 2009a). The calibration points were then corrected for distortion using a global approach that employed a fourth-order polynomial fit (Kedgley, 2009a). Figure 2.3, Figure 2.4 and Figure 2.5 show the distortion grid, a typical calibration image, and a typical distortion grid image, respectively.

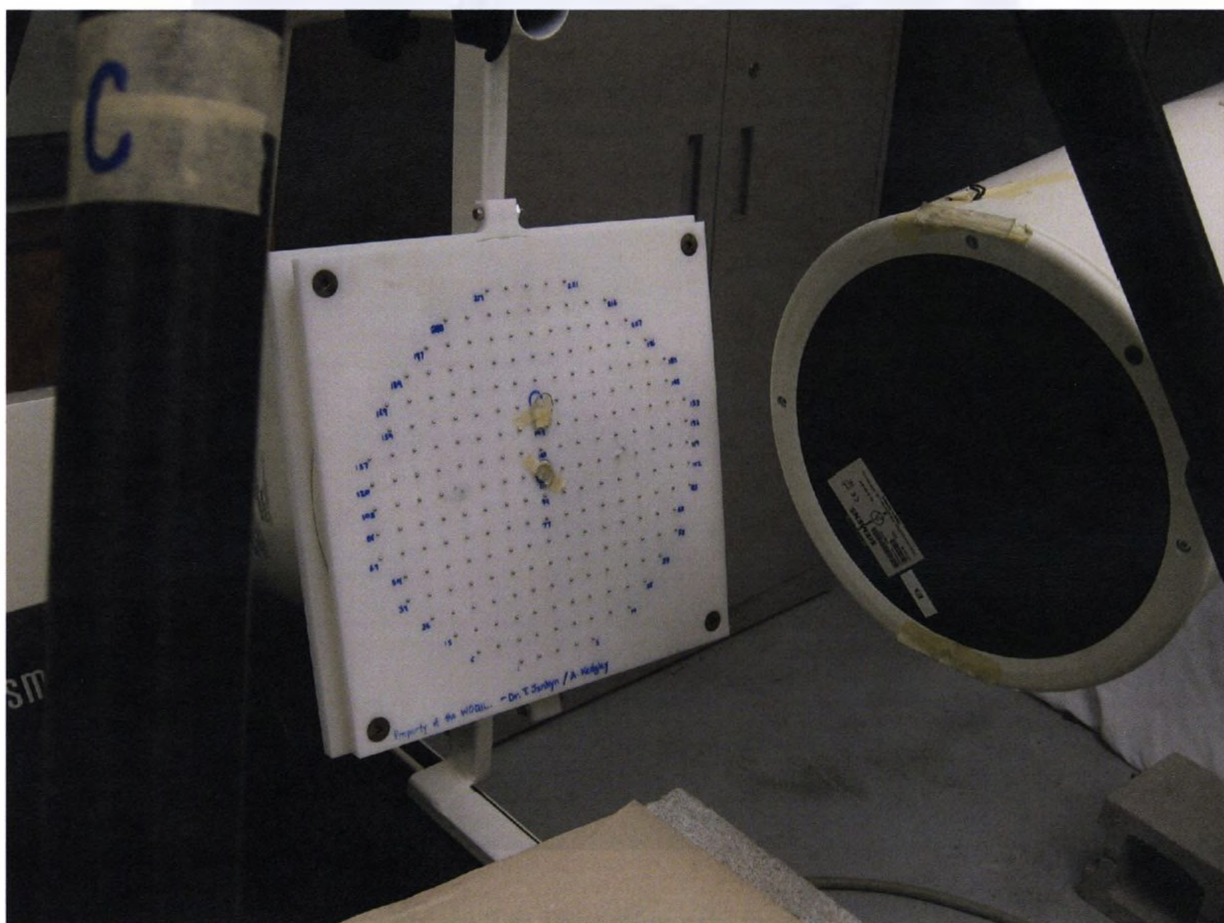


Figure 2.3: Distortion grid

Precisely constructed grid of stainless steel beads embedded in plastic that is used to correct for image distortion.

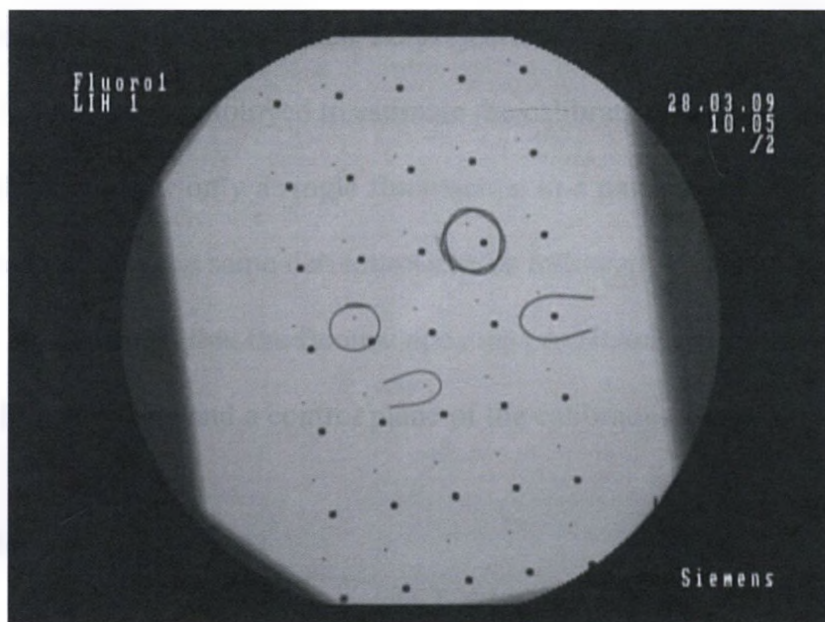


Figure 2.4: Calibration frame image
Image of calibration frame showing fiducial and control beads.

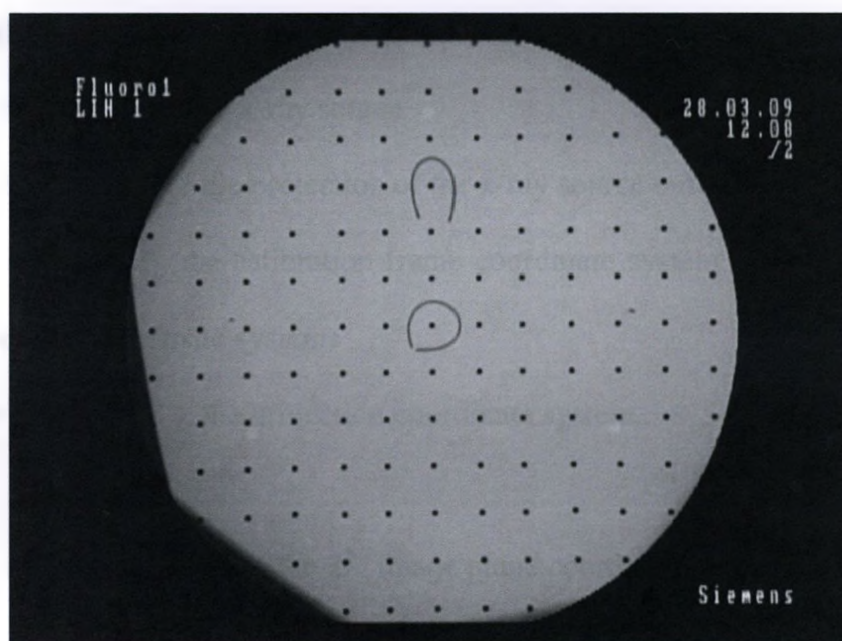


Figure 2.5: Distortion grid image

2.2.1 CALIBRATION ALGORITHM

The calibration algorithm is based on the work of Rougée *et al.* (1993). Each fluoroscope is represented using a perspective projection model and a relationship

between 3D calibration points and their 2D projections is defined. Using this relationship, an optimization routine is employed to estimate the calibration parameters.

The derivation for only a single fluoroscope in a particular calibration set-up will be documented because the same derivation can be followed when calibrating the second fluoroscope. It is assumed that the fluoroscopes are positioned such that each fluoroscope can image a fiducial plane and a control plane of the calibration frame.

2.2.1.1 FLUOROSCOPE MODEL

Each fluoroscope is modeled as a pinhole camera, using a perspective projection model. It is assumed that all x-rays are straight lines that originate from a single point source. Figure 2.6 represents the perspective projection model, where:

o = the origin of the calibration frame

s = the position of the x-ray source

s' = the position of the projection of the x-ray source onto the image plane

$R = (o, X, Y, Z)$, the calibration frame coordinate system (also referred to as the laboratory coordinate system)

$R' = (s, X', Y', Z')$, the projection coordinate system.

The C and L axes define the 2D image plane coordinate system and are parallel to the Y' and Z' axes, respectively. It should be noted that all measurements are in mm, except for measurements in the image plane coordinate systems, which are in pixels. A calibration bead or point and its corresponding image point are also shown (Figure 2.6).

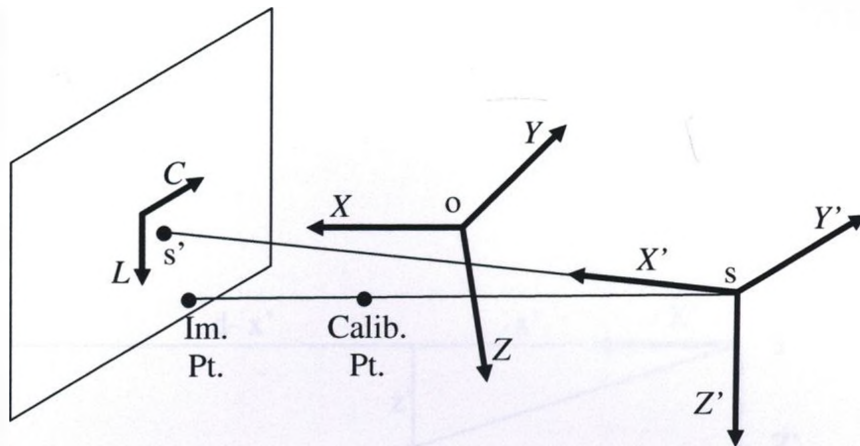


Figure 2.6: Perspective projection model

Perspective projection model illustrating the calibration frame coordinate system, projection coordinate system, a calibration point (Calib. Pt.), and an image point (Im. Pt.).

By viewing the perspective projection model in the Y' direction (Figure 2.7) and Z' direction (Figure 2.8), a relationship between the coordinates of a calibration point in the projection coordinate system (x', y', z') and its image point (c, l) can be determined:

$$(l - l_s) s_p = z' \left(\frac{d}{x'} \right) \quad (\text{Eq. 2.1})$$

$$(c - c_s) s_p = y' \left(\frac{d}{x'} \right) \quad (\text{Eq. 2.2})$$

where:

d = distance from s to s' (mm)

s_p = pixel size (mm)

(c, l) = coordinates of an image point (pixels)

(c_s, l_s) = coordinates of the projection of the source (pixels)

(x', y', z') = calibration point in the projection coordinate system (mm)

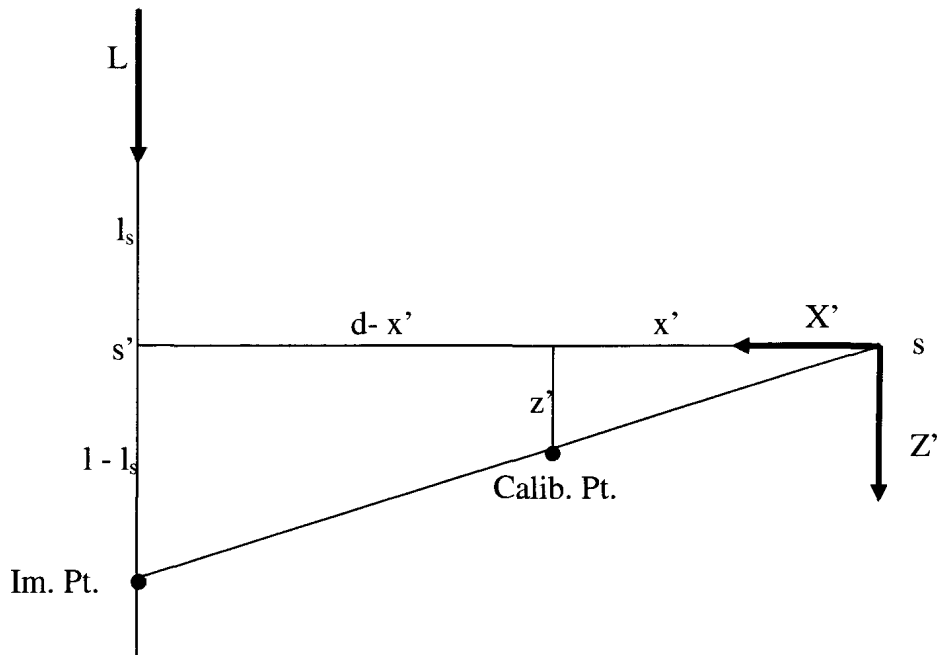


Figure 2.7: Perspective projection model viewed in the Y' direction

Planar view of the projection of a calibration point (Calib. Pt.) onto the image plane (Im. Pt.). The distances labeled are used to determine a relationship between the coordinates of a calibration point in the projection coordinate system (x', y', z') and its image point (c, l) in the X' - Z' plane.

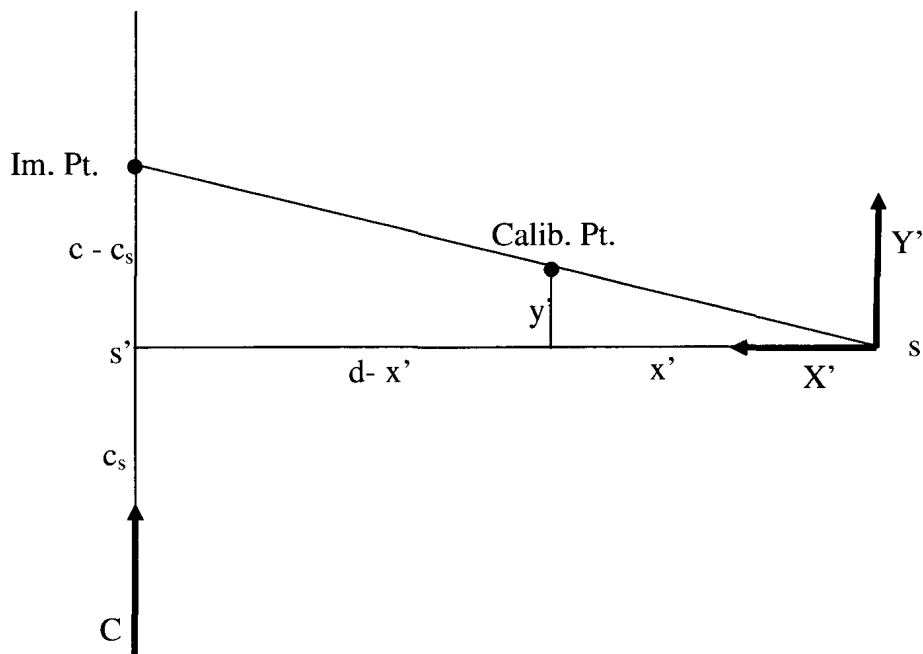


Figure 2.8: Perspective projection model viewed in the Z' direction

Planar view of the projection of a calibration point (Calib. Pt.) onto the image plane (Im. Pt.). The distances labeled are used to determine a relationship between the coordinates of a calibration point in the projection coordinate system (x', y', z') and its image point (c, l) in the X' - Y' plane.

Equations 2.1 and 2.2 can be written in matrix form (Eq. 2.3).

$$\frac{x'}{d} \begin{bmatrix} c \\ 1 \\ 1 \end{bmatrix} = \begin{bmatrix} \frac{c_s}{d} & \frac{1}{s_p} & 0 \\ \frac{l_s}{d} & 0 & \frac{1}{s_p} \\ \frac{1}{d} & 0 & 0 \end{bmatrix} \begin{bmatrix} x' \\ y' \\ z' \end{bmatrix} \quad (\text{Eq. 2.3})$$

where matrix $\mathbf{P}(c_s, l_s, d)$ is defined as:

$$\mathbf{P}(c_s, l_s, d) = \begin{bmatrix} \frac{c_s}{d} & \frac{1}{s_p} & 0 \\ \frac{l_s}{d} & 0 & \frac{1}{s_p} \\ \frac{1}{d} & 0 & 0 \end{bmatrix} \quad (\text{Eq. 2.4})$$

The coordinates of a calibration point in R' are not known, but they can be derived from their known coordinates in R (the laboratory coordinate system).

$$\begin{bmatrix} x' \\ y' \\ z' \end{bmatrix} = \mathbf{R}(\theta, \phi, \psi) \begin{bmatrix} x - x_s \\ y - y_s \\ z - z_s \end{bmatrix} \quad (\text{Eq. 2.5})$$

where:

$\mathbf{R}(\theta, \phi, \psi)$ = the Z-Y-X Euler angle rotation sequence associated with the

change in axes from R to R'

θ = rotation about the Z axis

ϕ = rotation about the Y axis (inclination)

ψ = rotation about the X axis (rotation in the plane)

The rotation matrix \mathbf{R} is calculated as shown:

$$\mathbf{R}(\theta, \phi, \psi) = \text{rot}(\mathbf{Z}, \theta) \text{rot}(\mathbf{Y}, \phi) \text{rot}(\mathbf{X}, \psi) \quad (\text{Eq. 2.6})$$

$$\mathbf{R}(\theta, \phi, \psi) = \begin{bmatrix} \cos \theta & -\sin \theta & 0 \\ \sin \theta & \cos \theta & 0 \\ 0 & 0 & 1 \end{bmatrix} \begin{bmatrix} \cos \phi & 0 & \sin \phi \\ 0 & 1 & 0 \\ -\sin \phi & 0 & \cos \phi \end{bmatrix} \begin{bmatrix} 1 & 0 & 0 \\ 0 & \cos \psi & -\sin \psi \\ 0 & \sin \psi & \cos \psi \end{bmatrix} \quad (\text{Eq. 2.7})$$

where:

$\text{rot}(\mathbf{Z}, \theta)$ = rotation about Z of magnitude θ

Equation 2.5 can be written as:

$$\begin{bmatrix} x' \\ y' \\ z' \end{bmatrix} = \mathbf{R}(\theta, \phi, \psi) \mathbf{T}(x_s, y_s, z_s) \begin{bmatrix} x \\ y \\ z \\ 1 \end{bmatrix} \quad (\text{Eq. 2.8})$$

where:

$$\mathbf{T}(x_s, y_s, z_s) = \begin{bmatrix} 1 & 0 & 0 & -x_s \\ 0 & 1 & 0 & -y_s \\ 0 & 0 & 1 & -z_s \end{bmatrix} \quad (\text{Eq. 2.9})$$

Substituting equations 2.4 and 2.8 into equation 2.3 gives

$$\frac{x'}{d} \begin{bmatrix} c \\ 1 \\ 1 \end{bmatrix} = \mathbf{P}(c_s, l_s, d) \mathbf{R}(\theta, \phi, \psi) \mathbf{T}(x_s, y_s, z_s) \begin{bmatrix} x \\ y \\ z \\ 1 \end{bmatrix} \quad (\text{Eq. 2.10})$$

Assuming that

$$\mathbf{M}(\xi) = \mathbf{P}(c_s, l_s, d) \mathbf{R}(\theta, \phi, \psi) \mathbf{T}(x_s, y_s, z_s) \quad (\text{Eq. 2.11})$$

Equation 2.10 can be re-written as

$$\frac{x'}{d} \begin{bmatrix} c \\ 1 \\ 1 \end{bmatrix} = \mathbf{M}(\xi) \begin{bmatrix} x \\ y \\ z \\ 1 \end{bmatrix} \quad (\text{Eq. 2.12})$$

where:

$(\xi_j)_{j=1,9}$ = the calibration parameters, $(x_s, y_s, z_s, \theta, \phi, \psi, c_s, l_s, d)$

Equation 2.12 provides the required relationship between 3D points and their 2D projections. Using the known coordinates of 3D calibration points (x_i, y_i, z_i) and their measured corresponding 2D projected image points (c_i, l_i) , each point $i=1,N$ must satisfy equation 2.12, which can also be written as:

$$c_i = \frac{m_{11}x_i + m_{12}y_i + m_{13}z_i + m_{14}}{m_{31}x_i + m_{32}y_i + m_{33}z_i + m_{34}} \quad (\text{Eq. 2.13})$$

$$l_i = \frac{m_{21}x_i + m_{22}y_i + m_{23}z_i + m_{24}}{m_{31}x_i + m_{32}y_i + m_{33}z_i + m_{34}} \quad (\text{Eq. 2.14})$$

where:

m_{kl} = the k^{th} row and l^{th} column of $\mathbf{M}(\xi)$

2.2.1.2 PIXEL SIZE CALCULATION

Pixel size is not a calibration parameter, but is considered a known quantity in the calibration algorithm. In order to determine the pixel size for each fluoroscope a pixel grid was manufactured with 0.2 mm diameter holes at known locations (Appendix A.1). The pixel grid was attached to the image intensifier (II) entrance side and radiographs were taken. “Pixel_Size_Calculator” code (Appendix A.2) was developed in MATLAB (The MathWorks, Natick, MA, USA) based on pre-existing code used to digitize images (Kedgley, 2009a). Using the “Pixel_Size_Calculator” code, the five holes closest to the centre of the II were digitized and the average pixel size was calculated based on the known distance between holes in mm and pixels (Appendix A.2 and A.3). The holes closest to the II centre were chosen in order to reduce errors due to image distortion, which tend to be smallest at the centre. The average pixel size for fluoroscopes A and B were found to be 0.3847 mm and 0.3819 mm, respectively.

2.2.1.3 PARAMETER ESTIMATION

Knowing the pixel size and the mathematical relationship between 3D calibration points and their 2D projections, an optimization routine was employed to estimate the calibration parameters. A custom-coded program was written in MATLAB, using the

MATLAB ‘fmincon’ function, which finds the minimum of a constrained nonlinear multivariable function through numerical optimization. The optimization components include: the known 3D calibration point coordinates (x_i, y_i, z_i) , the digitized and distortion-corrected 2D image point coordinates (c_i, l_i) , an objective or cost function to minimize, constraint equations and initial estimates of the calibration parameters,

The 2D image point coordinates were determined by first digitizing calibration images and then correcting these points for image distortion using custom-written code by Kedgley, 2009a. The 3D calibration points were matched with their corresponding 2D image points to be used as input parameters for the optimization.

The optimization routine was based on minimizing the root mean squared error ($E(\xi)$) between 2D image points (c_i, l_i) , as digitized on the calibration images and 2D image points $(c_i(\xi), l_i(\xi))$ as calculated using the calibration parameters.

$$E(\xi) = \sqrt{\frac{1}{N} \sum_{i=1}^N [(c_i(\xi) - c_i)^2 + (l_i(\xi) - l_i)^2]} \quad (\text{Eq. 2.15})$$

where:

$E(\xi)$ = root mean squared error

c_i, l_i = the 2D coordinates of projection points found by digitizing calibration images

$c_i(\xi), l_i(\xi)$ = the 2D coordinates of projection points calculated from (x_i, y_i, z_i) by applying equations 2.13 and 2.14

The symbolic equations for $c_i(\xi)$ and $l_i(\xi)$ were written in Maple (Maplesoft, Waterloo, ON, Canada) using equations 2.13 and 2.14 (Appendix B), which were then

used in custom-written MATLAB code to calculate $c_i(\xi)$ and $l_i(\xi)$ and ultimately estimate the calibration parameters (Appendix C).

It should be noted that the x-ray source position (x_s, y_s, z_s) was not estimated using the optimization algorithm. Instead, existing standard RSA code (Kedgley, 2009a) was used to calculate the source position, meaning the source position coordinates were no longer considered calibration parameters, but were known values. The calibration parameters to be estimated using the optimization algorithm were therefore redefined to be:

$$(\xi_j)_{j=1,6} = \theta, \phi, \psi, c_s, l_s, d \quad (\text{Eq. 2.16})$$

Constraint equations were used to ensure:

$$2 \geq c_s \geq -2 \quad (\text{Eq. 2.17})$$

$$2 \geq l_s \geq -2 \quad (\text{Eq. 2.18})$$

$$1005 \geq d \geq 995 \quad (\text{Eq. 2.19})$$

If the distortion grid is completely centered on the II, the coordinates of the projected source (c_s, l_s) should ideally be (0,0) and according to the fluoroscope operating manual (SIREMOBIL Compact (L), Siemens Medical Solutions USA Inc., Malvern, PA, USA) the distance d should be 1000 mm. Since manufacturing tolerances for these values are not reported and the distortion grid can be slightly off-center, it was thought reasonable to constrain the projected source to within 2 pixels of (0,0) and d to within 5 mm of 1000 mm.

Initial Euler angle estimates were found by iterating through different angle values to find the combination resulting in the lowest $E(\xi)$. The angles were initially

iterated from $-\pi$ radians to π radians with a step size of $\pi/16$ radians. Two other iterations were then performed with successively smaller intervals and step sizes, in order to determine more precise starting estimates for the Euler angles. As previously mentioned, with no reported manufacturing tolerances, the projected source coordinates (c_s, l_s) and source to II distance (d) should be (0,0) mm and 1000 mm, respectively, which were therefore used as the initial estimates. See Appendix C for MATLAB code and instructions to estimate the calibration parameters.

2.2.2 IMAGE PLANE CORRECTION

The calibration algorithm used the positions of 3D calibration points as well as their corresponding 2D projected calibration points as input parameters. These 2D points were corrected for image distortion, meaning their coordinates were expressed relative to the distortion grid coordinate system, as opposed to a coordinate system aligned with the image. The use of a distortion grid produced undesirable image rotations and translations, which have also been reported by previous authors (Gronenschild, 1997; Holdsworth *et al.*, 2005). An image plane correction was therefore required in order to reposition and realign the image within the image plane.

When distortion grid images were captured, the grid was first positioned manually against the input screen of the image intensifier. Using visual inspection, the lines of beads on the grid were aligned with the fluoroscopic images to avoid excessive image rotations induced by the distortion correction process. In order to correct for any residual image rotation and translations, custom-written MATLAB and RhinoScript (Rhinceros, Robert McNeel & Associates, Seattle, WA, USA) programs were used. An initial estimate of the required image plane rotation and translation was found based on the

negative rotation and translation of the distortion grid with respect to the pixel coordinate system on the images (Appendix D.1). An optimization routine was then employed to find the final image pose.

In order to employ this optimization routine, it was necessary to recreate the experimental set-up using the estimated calibration parameters, which is described in detail in Section 2.3 and Appendix E. A RhinoScript program entitled “ImportPoints” (Appendix D.2) was used to plot the 2D calibration points, which had been digitized and distortion corrected, onto the image (Figure 2.9). These 2D points were named distortion-corrected points.

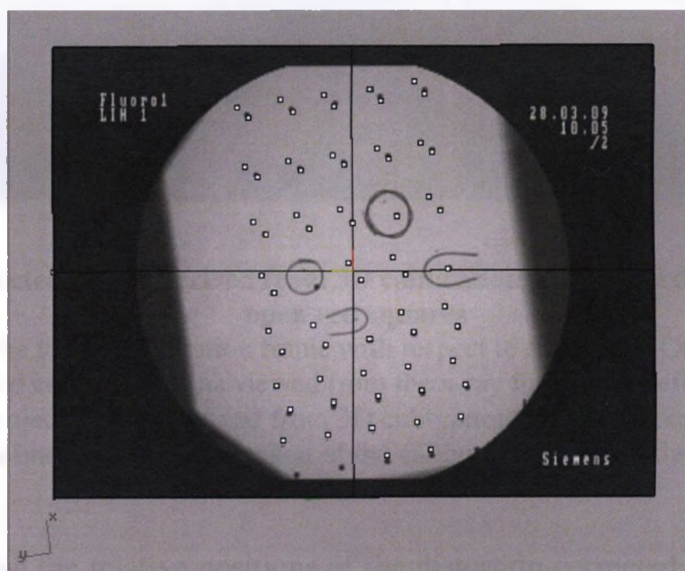


Figure 2.9: Distortion-corrected 2D calibration points shown as open squares and uncorrected points as black circular image points

After distortion correction, many of the corrected points (squares) obscure the view of the uncorrected black circular image points. Near the center one can see there is less distortion (black circles completely obscured by squares) compared to the edge of the image (black circles beside the squares).

With the experimental set-up modeled, the calibration frame was imported into the virtual environment (Figure 2.10). Another RhinoScript program entitled

“ProjectPoints” was run to project the 3D calibration frame points onto the image plane (Appendix D.3). These 2D point coordinates were named projected points.

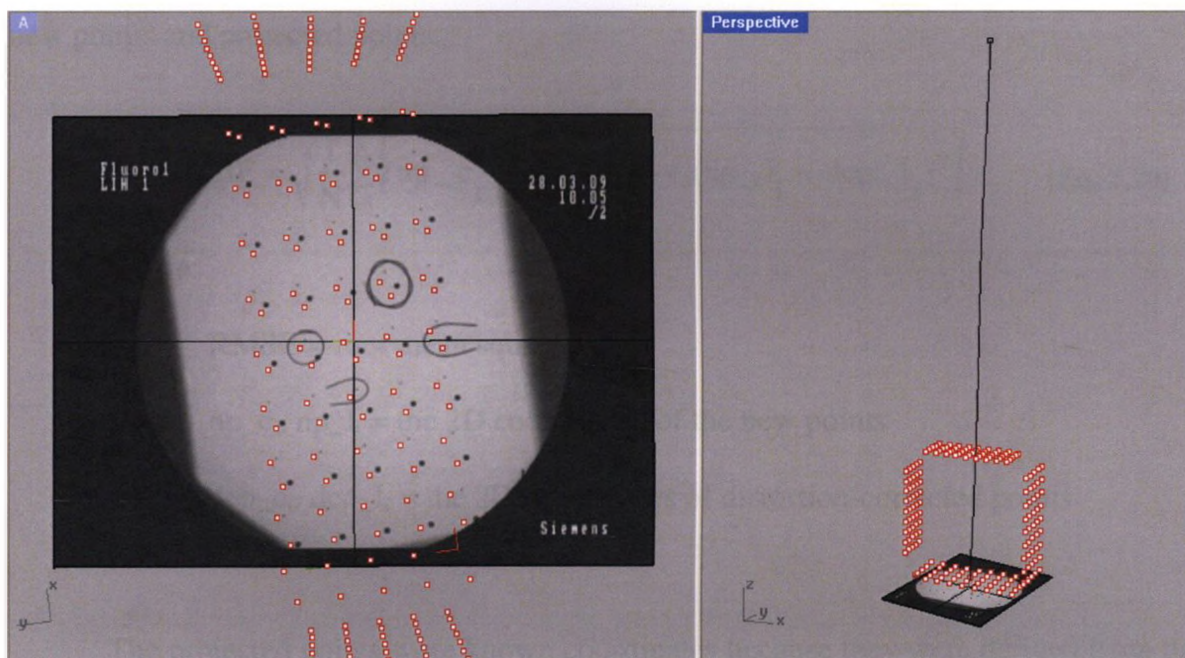


Figure 2.10: Projected points derived from 3D calibration frame coordinates are shown in open red squares

Model depicting the virtual calibration frame with respect to the image. One can see the beads from the fiducial and control plane as viewed from the x-ray foci on the left, and an overall view on the right. The projected point derived from 3D calibration frame coordinates (red squares) do not line up with image taken of the calibration frame on the left.

Even though the relative positions of the distortion-corrected points were known, their absolute positions in the plane were unknown. This can be seen by viewing the mismatch of points in Figure 2.10. Therefore, the optimization routine aimed to find new absolute positions for the distortion-corrected points (named new points). Once the new point coordinates were found, the final image plane pose could be realized.

Similar to the calibration optimization, the image plane optimization, entitled “Rot_Trans_ImPlane”, used the ‘fmincon’ function from the MATLAB optimization

toolbox. Appendices D.4, D.5 and D.6 provide the MATLAB code for the main function, objective function and constraint function, respectively.

The objective function was the root mean squared error (RMSE) between the new points and projected points.

$$\text{RMSE} = \sqrt{\frac{1}{N} \sum_{i=1}^N \left[(\text{np_c}_i - \text{dcp_c}_i)^2 + (\text{np_l}_i - \text{dcp_l}_i)^2 \right]} \quad (\text{Eq. 2.20})$$

where:

RMSE = root mean squared error

np_c_i, np_l_i = the 2D coordinates of the new points

dcp_c_i, dcp_l_i = the 2D coordinates of distortion-corrected points

The projected points were known coordinates because they were derived from the known 3D calibration point coordinates. The new point coordinates were not known, however, and the optimization attempted to find the coordinates of these points that minimize the objective function, while also obeying a set of constraint functions.

The constraint functions relied on the distortion-corrected points. Even though the absolute position of this group of points was unknown, the relative positions between the distortion-corrected points were known. The relative distance between any set of new points from $j = 1$ to M was constrained to equal the corresponding relative distance between sets of distortion-corrected points from $j = 1$ to M .

$$\text{np_d}_{j=1,M} - \text{dcp_d}_{j=1,M} = 0 \quad (\text{Eq. 2.21})$$

where:

$np_{d_{i=1,M}}$ = the distance between new points

$dcp_{d_{i=1,M}}$ = the distance between distortion-corrected points

Once the optimization was complete, the new points were compared to the distortion-corrected points in order to calculate the final image plane translation and rotation. See Appendix F for detailed instructions on performing the image plane correction.

2.3 EXPERIMENTAL SET-UP RECREATION

Using the estimated calibration parameters and image plane correction values, a virtual experimental set-up was recreated in a solid modelling program (Rhino, Robert McNeel & Associates, Seattle, WA, USA). This virtual set-up was necessary in order to match 3D models to their corresponding fluoroscopic images.

Each x-ray source was modeled as a perspective projection camera. The camera location was defined by the x-ray source coordinates and the camera target was placed at s' , the position of the projection of the source coordinate. Using the camera and target pairs, two viewpoints were created so that each image plane could be viewed from its respective x-ray source (Figure 2.11).

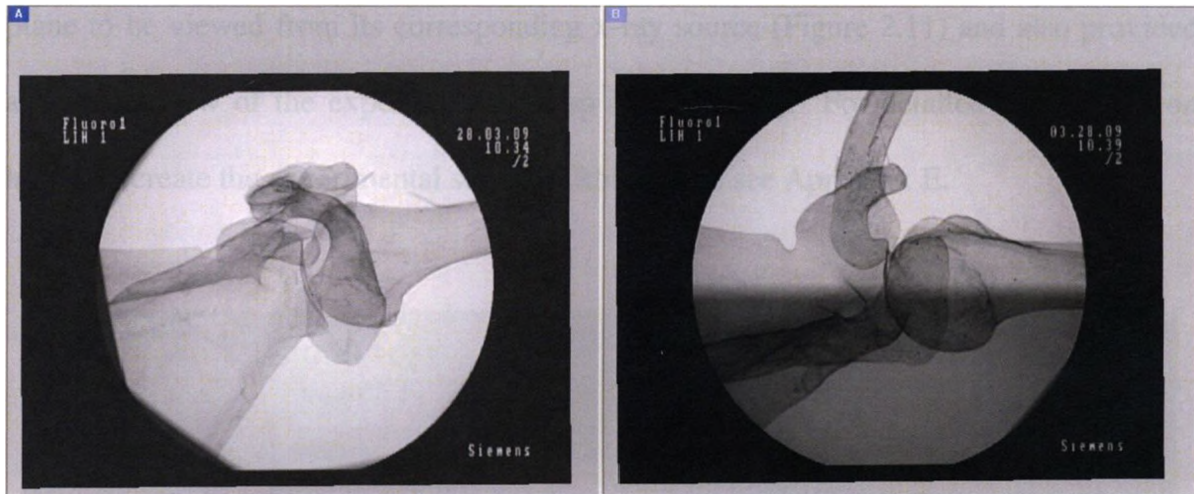


Figure 2.11 : Two viewpoints from the two x-ray foci
Two viewpoints from the two x-ray foci showing the scapula, humerus and clavicle.

The image planes were modeled by first creating a coordinate system specific to each image plane, which was aligned and positioned to match the calibration frame coordinate system. Next, each image plane coordinate system was rotated by its respective calibration Euler angle sequence and translated so that its origin coincided with its respective x-ray source coordinates. In order to position the image planes, a vector was created using the axis about which the final rotation was made (X' for the fluoroscope case modeled in Section 2.2.1.1). One end of the vector coincided with the corresponding x-ray source and its length was defined by d , as calculated during the calibration. The image plane was then defined by creating a plane orthogonal to the vector, with its centre translated by c_s and l_s . The size of each image plane was calculated using the pixel sizes as determined in Section 2.2.1.2 and the known pixel dimensions of the fluoroscopic images (540×720 pixels).

With the x-ray foci and images planes positioned correctly, the virtual experimental set-up was complete. This virtual environment allowed for each image

plane to be viewed from its corresponding x-ray source (Figure 2.11) and also provided an overall view of the experimental set-up (Figure 2.12). For detailed instructions on how to recreate the experimental set-up in Rhinoceros see Appendix E.

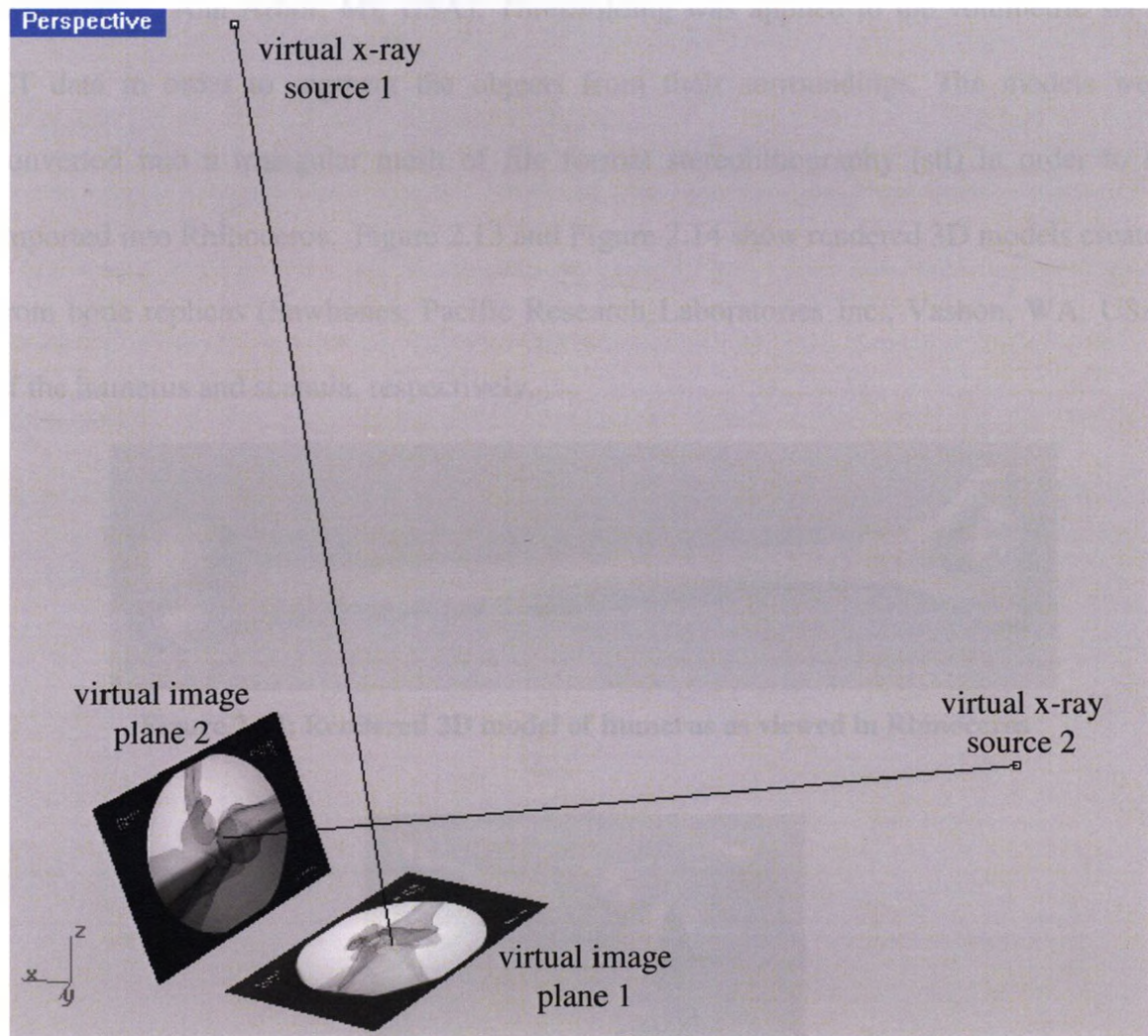


Figure 2.12: Experimental set-up

Virtual experimental set-up containing the two x-ray foci and image planes in Rhinoceros.

2.4 MODEL CREATION

3D models of the objects under study were created using Materialise Interactive Medical Image Control System (MIMICS) software with a MedCAD module (Materialise, Ann Arbor, MI, USA). Thresholding was applied to the volumetric set of CT data in order to segment the objects from their surroundings. The models were converted into a triangular mesh of file format stereolithography (stl) in order to be imported into Rhinoceros. Figure 2.13 and Figure 2.14 show rendered 3D models created from bone replicas (Sawbones, Pacific Research Laboratories Inc., Vashon, WA, USA) of the humerus and scapula, respectively.

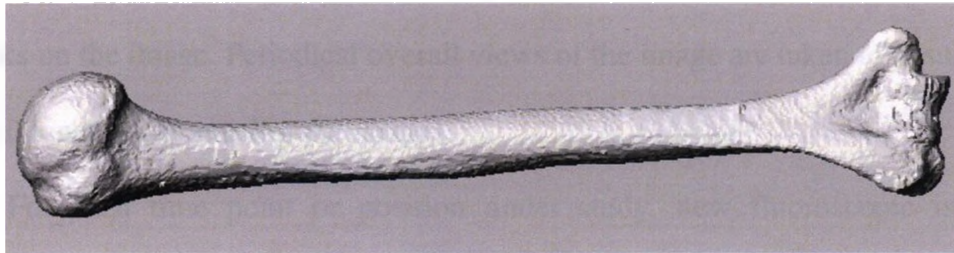


Figure 2.13: Rendered 3D model of humerus as viewed in Rhinoceros



Figure 2.14: Rendered 3D model of scapula as viewed in Rhinoceros

2.5 MATCHING

The matching procedure recreates the pose of the objects captured by the fluoroscopes. The computer models are imported into the virtual environment, where they can be translated and rotated in 3D space. Initially a global approach is taken where the entire fluoroscopic image is viewed and each bone's silhouette is matched to its entire bony outline on each image. During this stage, the 3D model is usually not moved in increments of less than 1 mm or 1°. Following the initial match, the image is enlarged on a few easily identifiable bony landmarks on each image, which are used to fine-tune the match. The model is moved by increments as small as 0.01 mm and 0.01 ° until the silhouette's of the bony landmarks completely matches the outlines of the bony landmarks on the image. Periodical overall views of the image are taken to ensure that the overall silhouette still matches the images.

For each time point or position under study, new fluoroscopic images are imported into the virtual environment and the model is re-matched. Figure 2.15 and Figure 2.16 show a humerus and scapula, respectively, after they have been matched to the fluoroscopic images in the virtual environment.

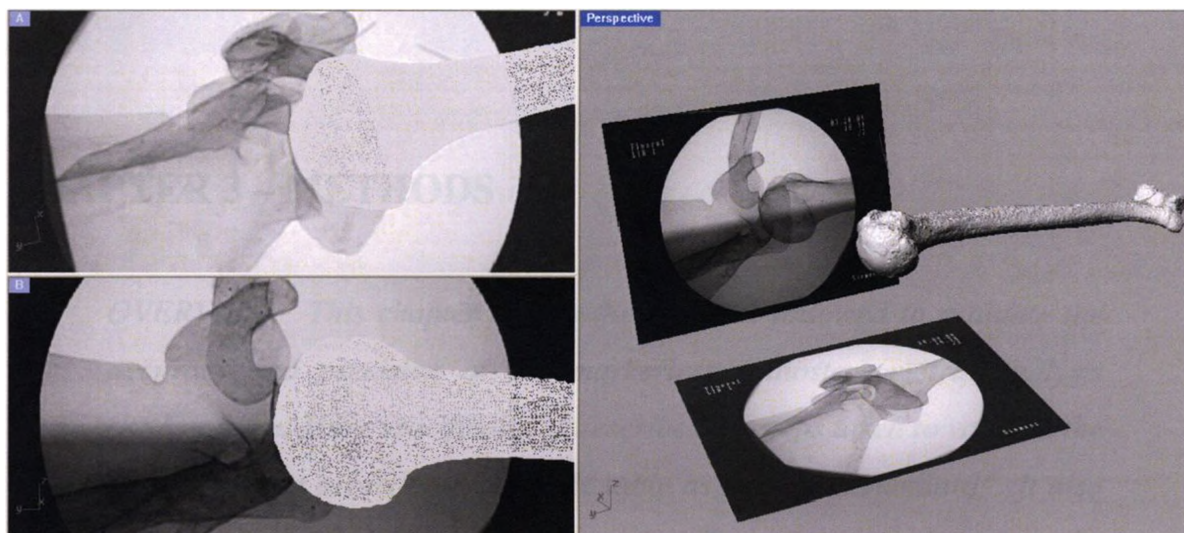


Figure 2.15: Humerus matched to fluoroscopic images

The left side contains the model of the humerus being matched to each image plane from the viewpoints of the corresponding x-ray foci. While the right side displays an overall view of both images, and the model of the humerus in the virtual 3D environment.

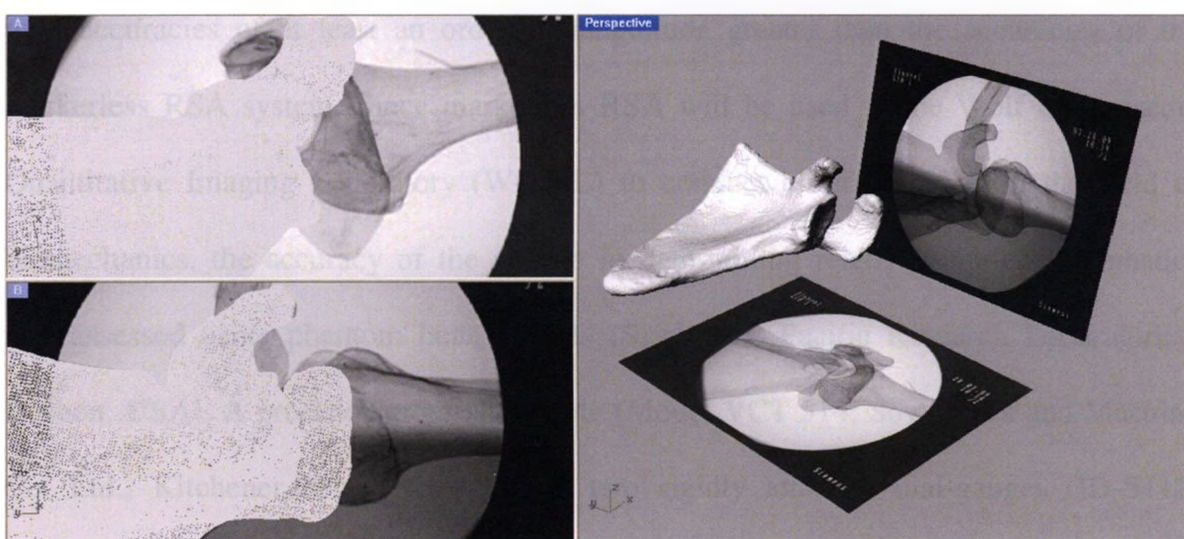


Figure 2.16: Scapula matched to fluoroscopic images

The left side contains the model of the scapula being matched to each image plane from the viewpoints of the corresponding x-ray foci. While the right side displays an overall view of both images, and the model of the scapula in the virtual 3D environment.

CHAPTER 3 – METHODS

OVERVIEW: This chapter details the protocol followed to evaluate the accuracy and precision of the markerless radiostereometric analysis (RSA) system. More specifically, it describes the steps taken to validate the system using a precision cross-slide table as the “gold standard”. It also outlines the methods used to evaluate the effect of computed tomography (CT) dosage on the accuracy of markerless RSA.

3.1 VALIDATION STUDY

In order to validate the markerless radiostereometric analysis system (RSA) system, it was necessary to evaluate its accuracy and precision against a “gold standard”, with accuracies of at least an order of magnitude greater than the accuracies of the markerless RSA system. Since markerless RSA will be used in the Wolf Orthopaedic Quantitative Imaging Laboratory (WOQIL) to conduct clinical studies in the field of biomechanics, the accuracy of the system in determining relative shoulder kinematics was assessed using phantom bone models (Sawbones; Pacific Research Laboratories, Vashon, USA). A precision cross-slide table (Model VCT 514; Sowa Tool and Machine Co. Ltd., Kitchener, ON, Canada) with two rigidly attached dial-gauges (ID-S112; Mitutoyo Corporation, Kawasaki, Japan) was used as the “gold standard” to quantify kinematic translation. The accuracy of this system is 1 μm . In order to evaluate kinematic orientations, a standard RSA system, which has an accuracy of 0.121° (Kedgley *et al.*, 2009b), was used as the “gold standard”.

3.1.1 EXPERIMENTAL SET-UP

Anatomically accurate foam bone models of a left humerus and scapula were used to perform the markerless RSA validation (Sawbones; Pacific Research Laboratories Inc., Vashon, WA, USA). These bone phantoms were manufactured with a zinc coating to mimic the contrast of bone during x-ray imaging. Stainless steel beads with a diameter of 0.8 mm were inserted into the bone models in order for standard RSA to be conducted.

The scapula was clamped to the stationary base of the cross-slide table and provided the fixed reference frame. Using a threaded rod and clamping mechanism the humerus was securely attached to the moveable cross-slide table and could be translated in the inferior/superior and anterior/posterior directions. The humerus could be clamped in various relative orientations to the stationary scapula.

Two fluoroscopes (SIREMOBIL Compact (L); Siemens Medical Solutions USA Inc., Malvern, PA, USA) were set-up up to be approximately orthogonal to one another and their fields of view were centered on the glenohumeral joint (Figure 3.1).

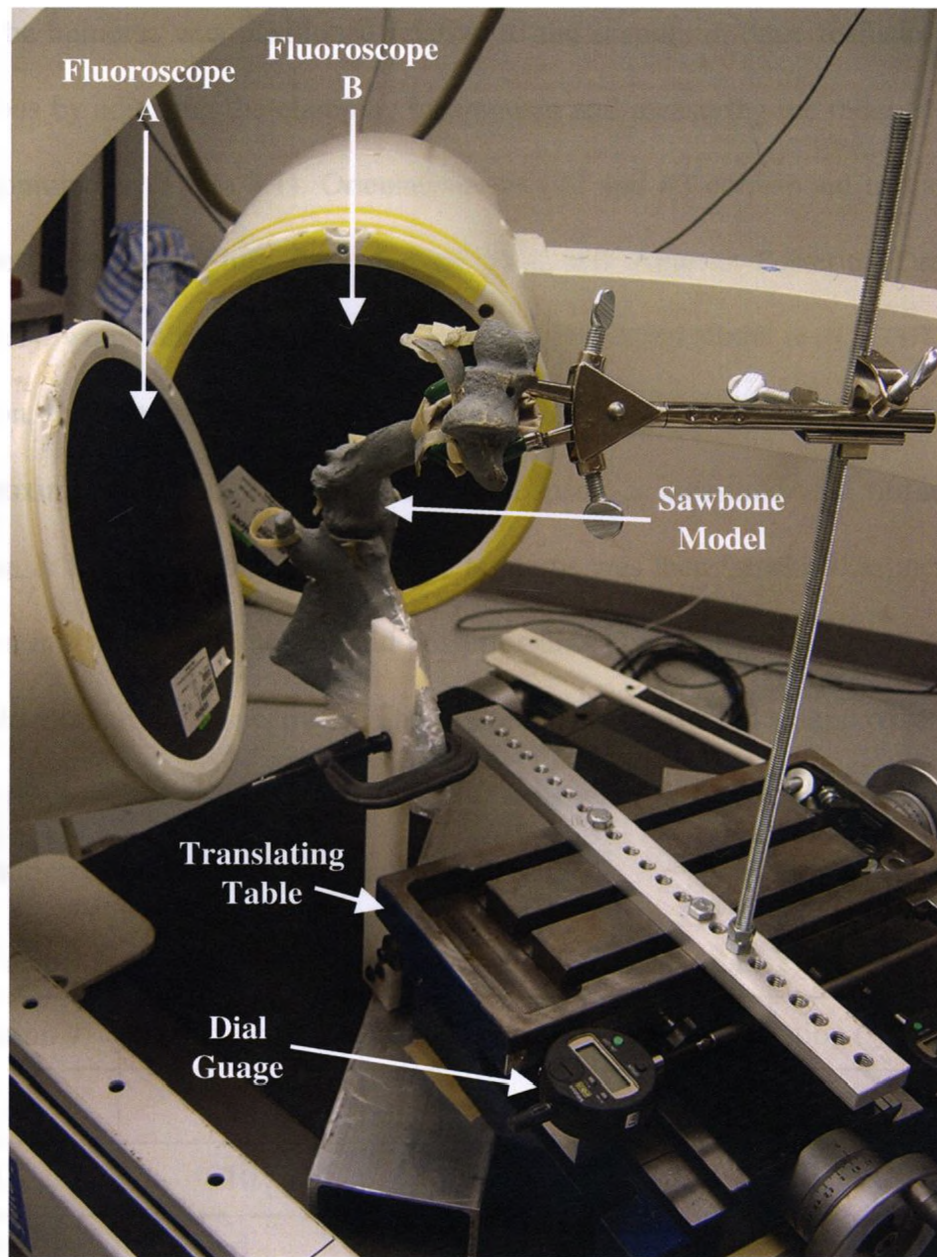


Figure 3.1: Experimental set-up for validation study

The experimental set-up used for the validation study showing the cross-slide table, dial-gauge, stationary scapula bone model, moveable humerus bone model and relative orientation of the two fluoroscopes.

3.1.2 EXPERIMENTAL PROTOCOL

In order to calibrate the fluoroscopy system, images of a calibration frame (Kedgley, 2009a; Kedgley *et al*, 2009b) were first taken before the experimental protocol was executed (see Section 2.2 for further details on the calibration method).

The humerus was positioned relative to the scapula in three realistic anatomical orientations by adjusting the clamping mechanism and measuring the relative orientation with a goniometer (Table 3.1). Orientations #1, #2 and #3 correspond to the clinically significant Load and Shift Test, Sulcus Test and Anterior-Posterior Drawer Test, respectively, which are used to evaluate shoulder instability (Bahk *et al.*, 2007). For each orientation, the humeral head was initially centered in the glenoid fossa, such that there was approximately 5 mm of glenohumeral joint space, as measured with vernier callipers (Petersson & Redlund-Johnell, 1983). The humerus was then translated in increments of 0.500 mm in the anterior, inferior and posterior direction for Orientation #1, Orientation #2 and Orientation #3, respectively. These directions represented an approximate path of 45° with respect to each fluoroscope. The humerus was translated at least 9 mm from the initial position or until it made contact with the scapula.

Table 3.1: Orientation and translation of the humerus relative to the scapula

Orientation #	Flexion (°)	Abduction (°)	External Rotation (°)	Translation
1	20	20	0	Anterior
2	10	10	90	Inferior
3	0	90	15	Posterior

At each position, simultaneous images were taken with the fluoroscopes, which were 720 pixels by 540 pixels in size (Figure 3.2). The voltage and current settings, set automatically by the fluoroscopes, were 50 kVp and 0.3 mA. Following testing, images of a grid of stainless steel beads (referred to as a “distortion grid”) (Kedgley, 2009a) were taken in order to correct the calibration points for image distortion (Section 2.2).

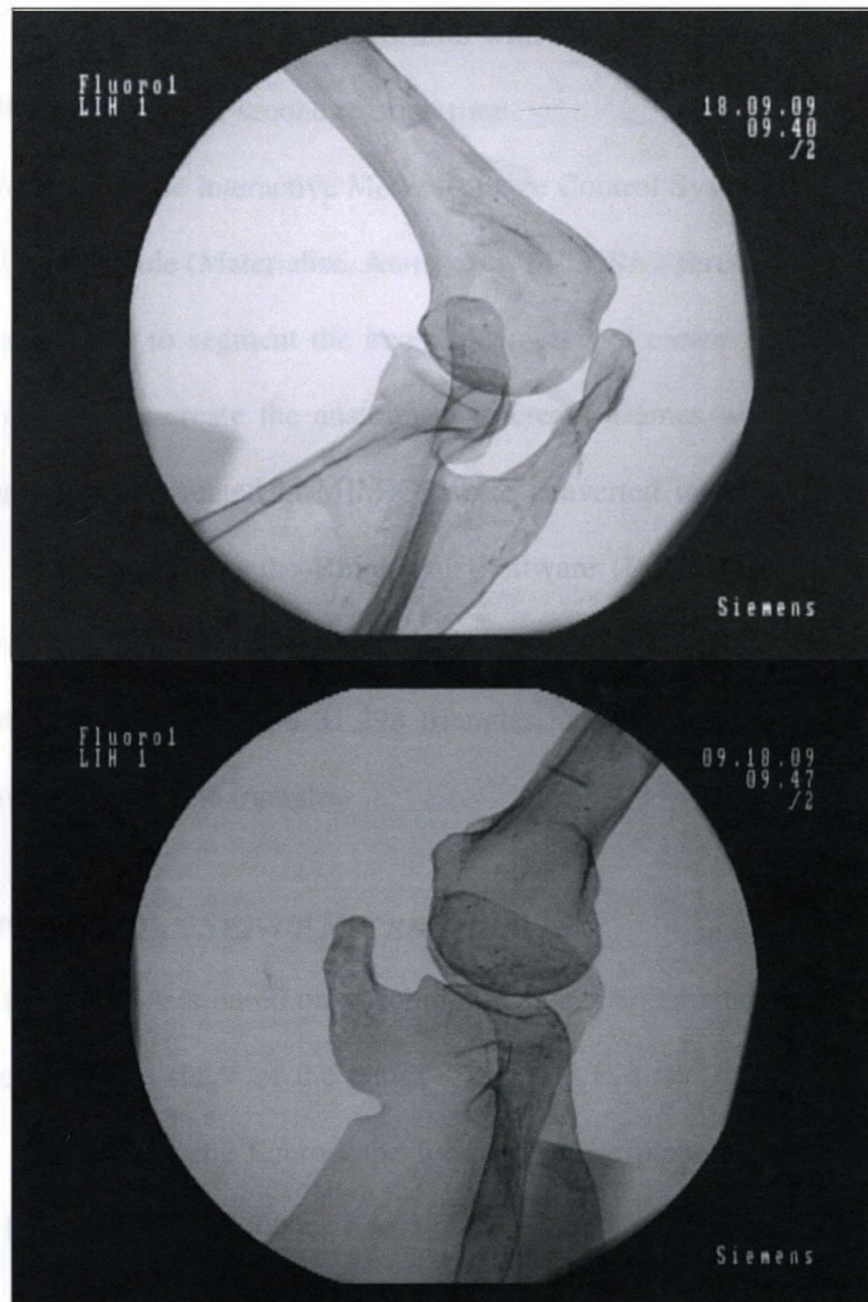


Figure 3.2: Images taken of bone models for the validation study

3.1.3 3D COMPUTER MODELS

Three-dimensional (3D) computer models of the humerus and scapula phantoms were created in order to perform markerless RSA. The phantoms were scanned using isotropic 3D computed tomography (CT) acquisition (Lightspeed VCT; GE Healthcare,

Piscataway, NJ, USA) using a bone algorithm with the following parameters: 0.625 mm sections, 140 kV, 200 mA, 1 second rotation time.

Using Materialise Interactive Medical Image Control System (MIMICS) software with a MedCAD module (Materialise, Ann Arbor, MI, USA), thresholding was applied to the CT data in order to segment the bone phantoms and create 3D models. The bony landmarks required to create the anatomical reference frames were digitized on these models. These models created in MIMICS were converted into triangular meshes that could then be imported into the Rhinoceros software (Robert McNeel & Associates, Seattle, WA, USA) that is used to recreate the experimental set-up. The humerus mesh consisted of 93,894 vertices and 31,298 triangles, and the scapula mesh consisted of 111,289 vertices and 37,096 triangles.

3.1.4 EXPERIMENTAL SET-UP RECREATION

Markerless RSA is based on matching the bones under study to two fluoroscopic images. Therefore, the shape of the bones (Section 3.1.3) and the experimental set-up, specifically the poses of the fluoroscope foci and image planes, were reconstructed. A calibration frame (Kedgley, 2009a; Kedgley *et al*, 2009b), “distortion grid” (Kedgley, 2009a) and custom-written code (Appendix C and Appendix D) were used to accurately determine the fluoroscope positions in 3D space (see Section 2.2 for more details).

Using these data, a virtual environment was created in Rhinoceros, in which the fluoroscope foci and images were positioned. The 3D computer bone models were imported into the virtual environment and moved in 3D space until their projections, from the points of view of the two fluoroscopic foci, matched the fluoroscopic images. The bones were manually matched to the images for each orientation and position imaged,

totalling 37 positions matched. The greater tuberosity, lesser tuberosity and anatomical neck were used as the main landmarks on the humerus for matching. The scapular notch, coracoid process and acromion process were the main landmarks used to match the 3D model of the scapula to the images. Figure 3.3 shows the virtual environment created for Orientation #1, with the humerus and scapula matched to the images.

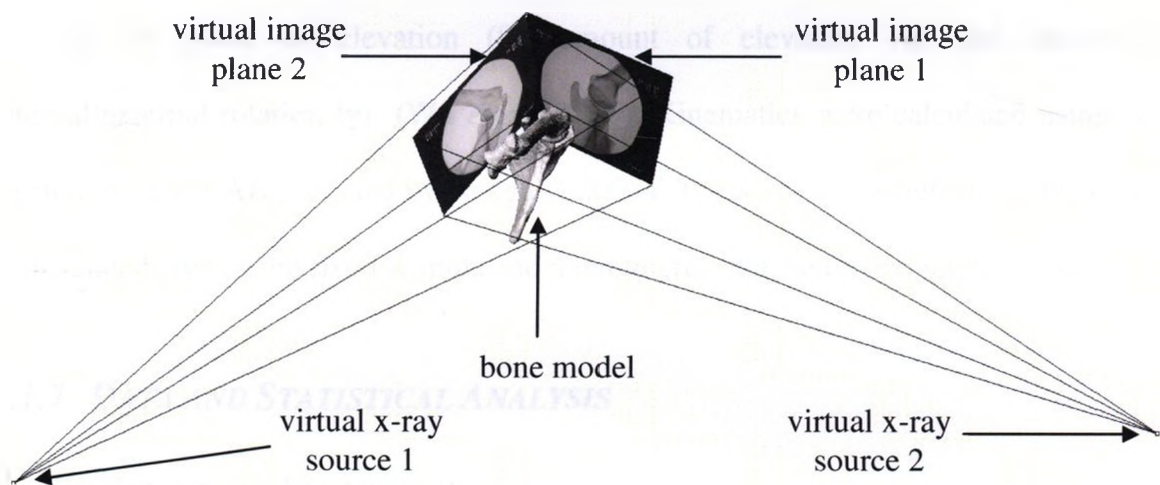


Figure 3.3: Experimental set-up recreation of Orientation #1
Screenshot of the virtual environment recreation in Rhinoceros software for Orientation #1. The virtual x-ray sources, virtual image planes and bone models are shown.

3.1.5 INTER-OPERATOR AND INTRA-OPERATOR RELIABILITY

Inter-operator reliability was assessed by having three operators perform the matching procedure of markerless RSA for the same image pair. Intra-operator reliability was assessed by having one operator match the same image pair on three different occasions that were at least three days apart. Before each matching procedure, the bones were imported into the virtual environment in a random orientation and position.

3.1.6 KINEMATICS

Once the bones were matched to the images, the positions of the bony landmarks were exported to create the anatomical reference frames. In order to characterize shoulder motion, specifically glenohumeral kinematics, all six kinematic parameters (three translations and three rotations) were calculated. Humeral orientation with respect to the scapula was calculated using a Y-X-Y Euler angle sequence, where the rotations defined the plane of elevation (β), amount of elevation (α) and amount of internal/external rotation (γ) (Wu *et al.*, 2006). Kinematics were calculated using code written in MATLAB provided by Kedgley, 2009a. Translation was defined as the change in distance between the fixed scapula and the humerus attached to the sliding tabletop.

3.1.7 DATA AND STATISTICAL ANALYSIS

3.1.7.1 KINEMATIC TRANSLATION

Intraclass correlation coefficients (ICC type 2,1) were used to evaluate the agreement between the known (dial-gauge) and calculated (markerless RSA) translations (Shrout and Fleiss, 1979) and the error in each translation was determined using the root mean squared error and the standard error of measurement (Streiner and Norman, 1995). Agreement between actual and calculated translations was also examined using Bland and Altman plots (Bland and Altman, 1986).

3.1.7.2 KINEMATIC ORIENTATION

For the three shoulder orientations examined, the Euler angle sequence, as calculated using markerless RSA, was compared to standard RSA. The mean and standard deviations (SD) were used to evaluate the accuracy and precision, respectively.

3.1.7.3 INTER-OPERATOR AND INTRA-OPERATOR RELIABILITY

Inter-operator reliability was assessed using the SD of the kinematic parameters as determined by the three operators. Similarly, intra-operator reliability was defined as the SD of the kinematic parameters, as determined by an operator matching one image set on three different occasions.

3.2 DOSAGE STUDY

The effect of lowering CT dosage on markerless RSA performance was investigated in order to find CT parameters that reduced radiation exposure to the subject, while still providing 3D models of sufficient accuracy.

3.2.1 CT ACQUISITION

One cadaveric shoulder specimen (male, age: 76 years) consisting of the proximal humerus, intact scapula and distal clavicle was tested. The frozen specimen was scanned using a helical CT machine (Light Speed Ultra; GE Medical Systems, New Berlin, WI, USA) with three protocols (Table 3.2). The current was varied because it is an easily modified parameter that directly affects CT dosage. Best practice at the hospital is to vary the current between 300 and 650 mA, depending on the size of the patient (M. Deaville, certified x-ray technician, personal communication, June 25, 2009). Therefore, Protocol #1 represents the normal-radiation dose condition where current was set midway between these extremes at 450 mA. Protocols #2 and #3 represent low-radiation dose conditions.

Table 3.2: CT protocol descriptions

Protocol #	Current (mA)	Voltage (kV)	Scan Time (seconds)	Slice Thickness (mm)	Pitch
1	450	120	0.8	0.625	0.969:1
2	150	120	0.8	0.625	0.969:1
3	50	120	0.8	0.625	0.969:1

The shoulder was scanned adjacent to a container of water to simulate the additional tissue that would be present in an *in vivo* subject (Bomford, 2003). The container measured 22 cm across, which is within normal range of half of a male's shoulder breadth (Pheasant & Haslegrave, 2006). Following each CT scan, the CT-dose index (CTDI) and dose-length product (DLP) were recorded to evaluate the CT dosage.

3.2.2 FLUOROSCOPIC TESTING

The cadaveric shoulder was allowed to thaw to room temperature before it was prepared for fluoroscopic testing. The inferior portion of the scapula was cleaned of soft tissue and then cemented (DenStone; Miles Inc., South Bend, IN, USA) inside a rectangular potting container that screwed to a Plexiglas sheet.

One fluoroscope was positioned under the sheet to provide a view in the coronal plane, while the other fluoroscope was positioned on an angle, providing a combined sagittal-transverse view. Figure 3.4 shows the experimental set-up, with bone models representing the cadaveric shoulder.

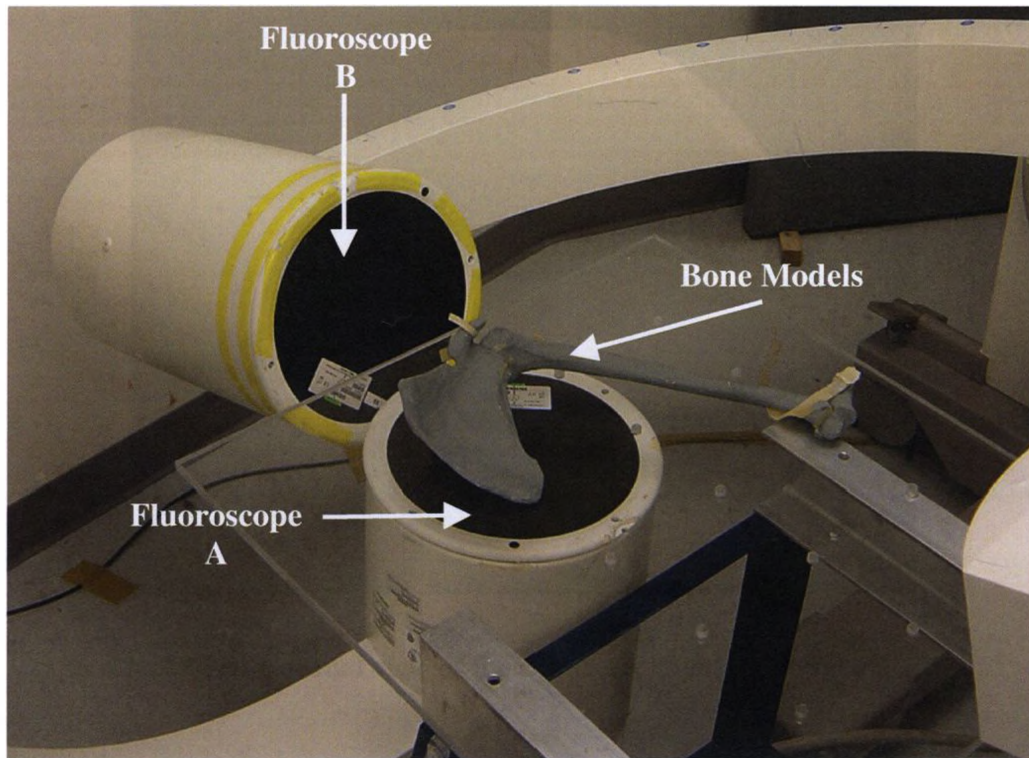


Figure 3.4: Experimental set-up for CT dosage study with a bone phantom representing the cadaveric shoulder

In the actual experiment the scapula was potted in cement and secured to the plexiglass sheet.

Once calibration images were taken (see Section 2.2 for further calibration details), images of the shoulder (720×540 pixels) were taken at approximately 45° of flexion and 45° abduction (Figure 3.5 and Figure 3.6). Following testing, images of a “distortion grid” (Kedgley, 2009a) were taken in order to correct the calibration points for image distortion (Section 2.2). The voltage and current settings, set automatically by the fluoroscopes, were 60 kVp and 1.4 mA for the fluoroscope providing a coronal view and 55 kVp and 0.7 mA for the other fluoroscope.

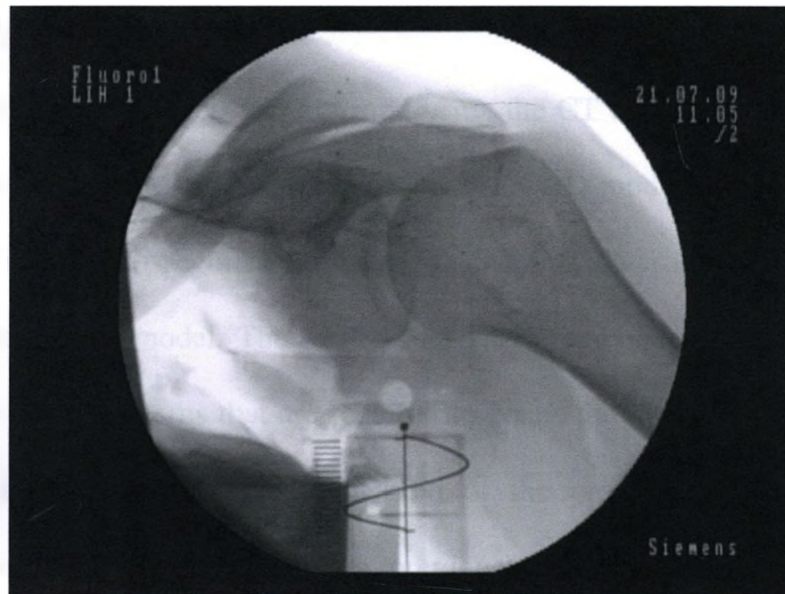


Figure 3.5: Coronal view of the cadaveric shoulder abducted 45°

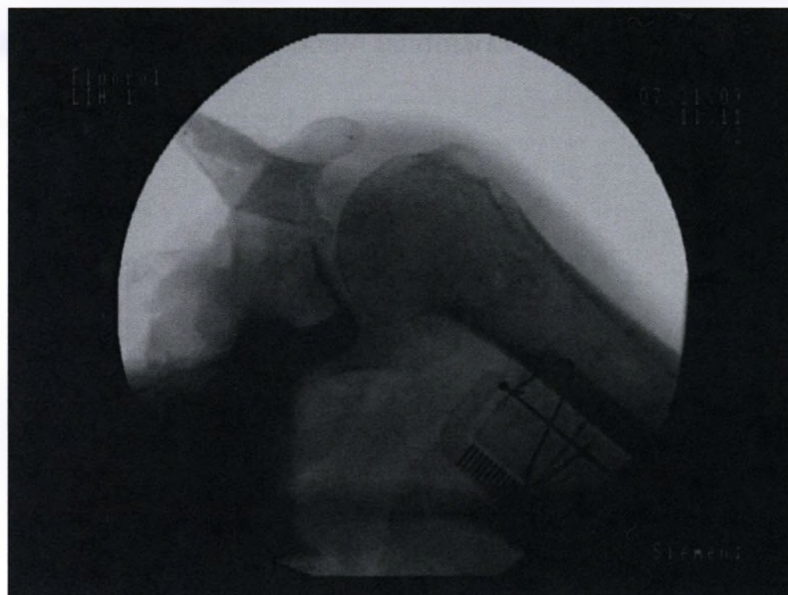


Figure 3.6: Sagittal-Transverse view of the cadaveric shoulder abducted 45°

3.2.3 3D MODEL CREATION

Three computer models were created using the CT data set from Protocol #1, #2 and #3, respectively. MIMICS software with a MedCAD module was used to threshold each data set in order to segment the humerus and scapula from the surrounding soft-tissue and create a 3D model. The medial and lateral epicondyles are bony landmarks located on the distal humerus that are required to create the humerus coordinate system. Since the cadaveric shoulder only consisted of the proximal humerus, these bony landmarks were unavailable. Instead, a previously acquired CT scan of the entire humerus of the same specimen was used to create a 3D model that was then registered to the proximal humerus model, such that they were aligned and positioned in the same coordinate system. With the distal and proximal portions of the humerus registered and in the same coordinate system, the bony landmarks required to create the anatomical reference frames were then digitized.

A 3D model was created of only the portion of the scapula being matched in order to reduce the time required to create the model. For Protocol #1, the humerus mesh consisted of 109,314 vertices and 36,438 triangles, and the scapula mesh consisted of 220,464 vertices and 73,488 triangles.



Figure 3.7: Rendered 3D model of shoulder using protocol#1 CT scans as viewed in Rhinoceros

For Protocol #2, the humerus mesh consisted of 110,586 vertices and 36,862 triangles, and the scapula mesh consisted of 209,892 vertices and 69,964 triangles (Figure 3.8).



Figure 3.8: Rendered 3D model of shoulder using protocol #2 CT scans as viewed in Rhinoceros

For Protocol #3, the humerus mesh consisted of 132,810 vertices and 44,270 triangles, and the scapula mesh consisted of 284,652 vertices and 94,884 triangles (Figure 3.9).



Figure 3.9: Rendered 3D model of shoulder using protocol #3 CT scans as viewed in Rhinoceros

3.2.4 EXPERIMENTAL SET-UP RECREATION

The experimental set-up was recreated in Rhinoceros using the process described in (Section 3.1.4). The bicipital groove was used as the main landmarks on the humerus for matching and the acromion and scapula notch were used as the main landmarks on the scapula for matching.

3.2.5 KINEMATICS

With the bones matched to the images, the positions of the bony landmarks were exported from Rhinoceros to create the anatomical reference frames for the humerus and scapula required to analyze glenohumeral kinematics. Humeral orientation with respect to the scapula was calculated using a Y-X-Y Euler angle sequence, where the rotations defined the plane of elevation (β), amount of elevation (α) and amount of internal/external rotation (γ). Humeral position with respect to the scapula was defined as the position of the centre of the humeral head in the scapula coordinate system (Wu *et al.*, 2006).

3.2.6 DATA ANALYSIS

The average root mean squared errors between the kinematic parameters, as calculated using the normal-dose and low-dose CT derived 3D bone models were compared.

CHAPTER 4 – RESULTS

OVERVIEW: This chapter begins by detailing the calibration results for both studies. It then describes the results of the validation study to quantify the accuracy and repeatability of the markerless radiostereometric analysis (RSA) system. It also contains the results of the study to investigate the effect of computed tomography (CT) dosage on markerless RSA accuracy.

4.1 CALIBRATION

Using the ‘fmincon’ function in MATLAB (The MathWorks, Natick, MA, USA), an optimization routine was employed to estimate both the calibration parameters and the image plane correction. The precision of the solution and ability of the optimization to converge was based on setting tolerances on the constraint function, objective function and parameters to be estimated (represented in the ‘fmincon’ function as ‘TolCon’, ‘TolFun’ and ‘TolX’, respectively).

4.1.1 PARAMETER ESTIMATION

With the optimization tolerances kept at the default value of 1×10^{-6} , the optimization routine converged successfully when estimating the calibration parameters for both fluoroscopes in the validation and dosage studies. For the validation study, the average root mean squared errors (RMSE) of the objective functions for the fluoroscopes were 0.310 mm and 0.245 mm. For the dosage study, the average RMSEs of the objective functions for the fluoroscopes were 0.118 mm and 0.175 mm.

4.1.2 IMAGE PLANE CORRECTION

It was more difficult to achieve convergence in a reasonable amount of time when applying the optimization for the image plane correction. Therefore the tolerances on the constraint functions and parameters to be estimated were increased for both to 0.001 mm. For the validation study, the average RMSEs of the objective functions for fluoroscopes were 1.122×10^{-7} mm and 3.826×10^{-8} mm respectively. For the dosage study, the average RMSEs of the objective functions for fluoroscopes A and B were 1.445×10^{-7} mm and 1.483×10^{-8} mm.

4.2 VALIDATION STUDY

The humerus was positioned relative to the scapula in three different orientations and for each orientation the humerus was translated in a different direction. For Orientation #1 and Orientation #3, the humerus was translated 9 mm in the anterior direction and 10 mm in the posterior direction, respectively. For Orientation #2, the humerus was translated until it made contact with the glenoid rim. This resulted in a translation of 8.5 mm.

4.2.1 TRANSLATION

The accuracy of the markerless RSA system in measuring relative kinematic translations was evaluated by comparing the actual translations (cross-slide table) to the measured translations (markerless RSA). The intra-class correlation coefficients (ICCs), standard errors of measurement (SEM) and RMSE for all three translations are listed in Table 4.1. Excellent agreement was found between the actual and measured translations

for all three scenarios, with ICCs greater than 0.999. The average SEM and RMSE were calculated to be 0.059 mm and 0.082 mm, respectively.

Table 4.1: ICCs, SEM, RMSE for all three translations

Orientation #	Translation	ICC	SEM (mm)	RMSE (mm)
1	Anterior	0.9997	0.046	0.063
2	Inferior	0.9994	0.067	0.093
3	Posterior	0.9995	0.065	0.091

Bland-Altman plots for Orientation #1, #2 and #3 are shown in Figure 4.1, Figure 4.2 and Figure 4.3, respectively. The horizontal axis in all plots is the mean translation as reported using the two measures (cross-slide table and markerless RSA) and the vertical axis is the difference between the two measures. The mean difference in measuring translation between the cross-slide table and markerless RSA is shown as solid line with plus and minus two standard deviations (SDs) plotted as a dashed line. The plots show a random distribution and with no obvious bias or trends in the difference between actual and measured translations using markerless RSA were observed. The SEM, RMSE and difference between measures for Orientation #1, as seen on Figure 4.1, were less than those for Orientations #2 and #3.

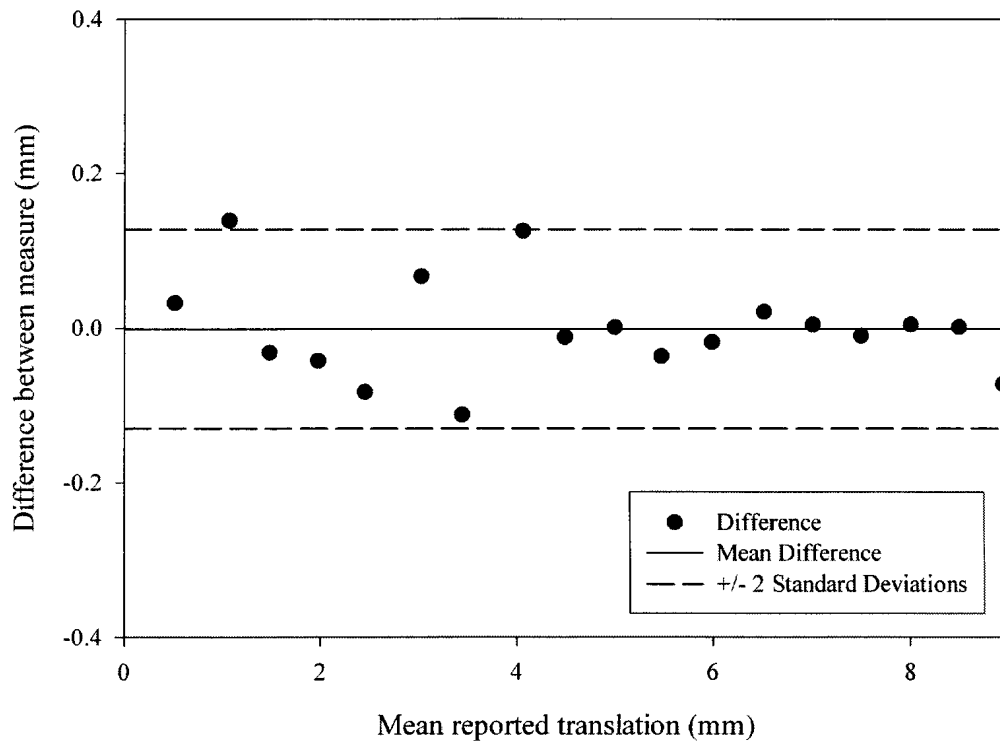


Figure 4.1: Bland-Altman plot for Orientation #1 in anterior translation

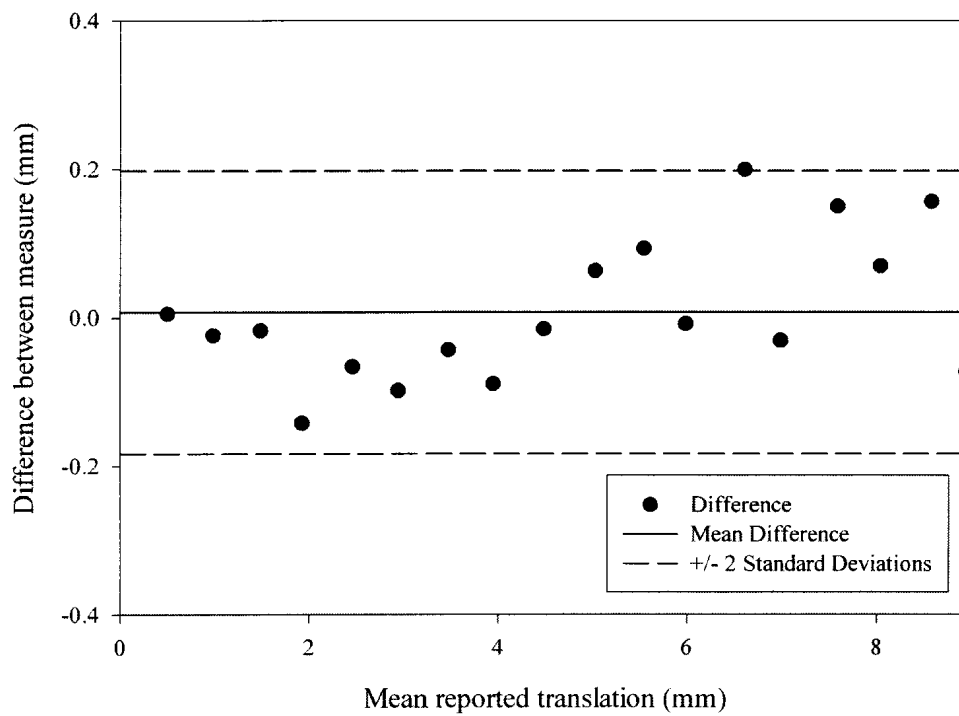


Figure 4.2: Bland-Altman plot for Orientation #2 in inferior translation

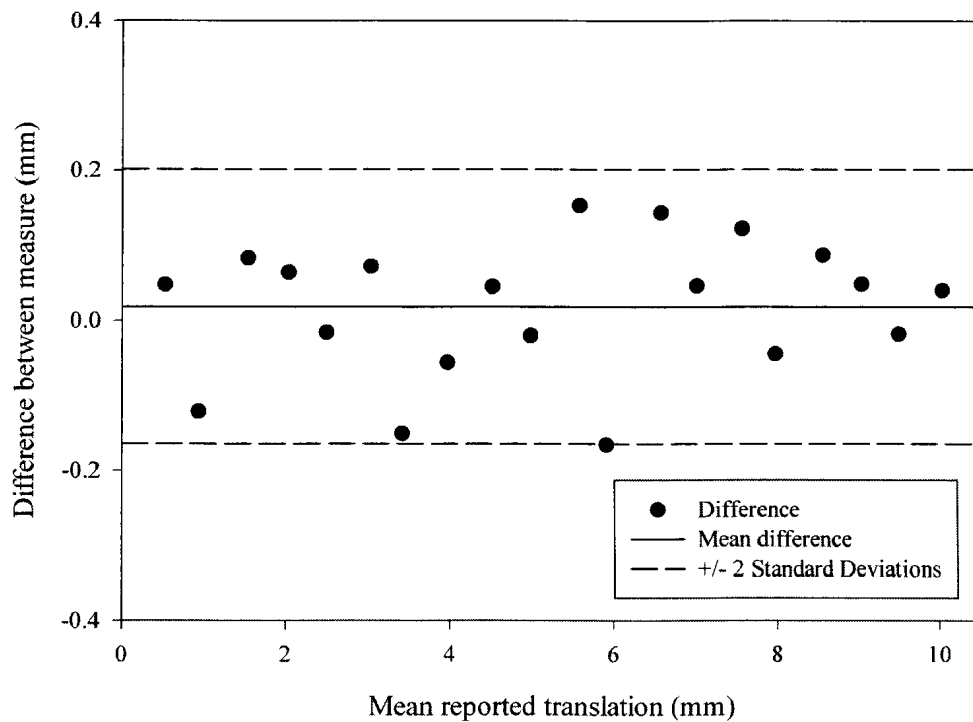


Figure 4.3: Bland-Altman plot for Orientation #3 in posterior translation

4.2.2 ORIENTATION

The accuracy of markerless RSA in measuring relative kinematic orientations was evaluated against the “gold standard” of standard RSA. Glenohumeral kinematics were calculated for each orientation, where the Euler angle rotations defined the plane of elevation (β), amount of elevation (α) and amount of internal/external rotation (γ) (Wu *et al.*, 2006). In orientations where there is very little elevation ($\alpha \approx 0$), different values of β and γ may result in approximately the same final pose if $\beta - \gamma$ are equal, since β and γ are both about the same axis of the humerus. Only at low elevations will this circumstance occur. Since Orientation #1 and #2 are at low levels of elevation, reporting only β and γ without reporting $\beta - \gamma$ would overestimate the actual markerless RSA error in calculating kinematic orientations. For this reason, the differences between standard RSA and markerless RSA in calculating β , α , γ and $\beta - \gamma$ for the three orientations is given in Table 4.2.

Table 4.2: Difference between kinematic orientations as measured using standard and markerless RSA

	Difference in measure (°)			
Orientation #	β	α	γ	$\beta - \gamma$
1	-1.34	0.071	0.16	-1.50
2	9.49	1.81	11.03	-1.54
3	0.69	0.47	1.56	-0.87

The average RMSE error was calculated using β , α and $\beta - \gamma$. Excluding the difference in the plane of elevation (β) for Orientation #2, the average RMSE for markerless RSA in determining kinematic orientations is 1.18°. Excluding this same angle, the SD in determining kinematic orientations is 1.22°. Without excluding the angle β for Orientation #2, the RMSE and SD for markerless RSA in determining kinematic orientations are 3.35° and 3.45°, respectively.

4.2.3 INTER-OPERATOR RELIABILITY

The initial starting position of Orientation #1 was matched by three different operators. The kinematic parameters as determined by each operator are given in Table 4.3. Using β , α and $\beta - \gamma$, the average SD for kinematic orientations and positions is 0.75° and 0.49 mm. Each operator spent two to five hours gaining familiarity with the Rhinoceros software (Robert McNeel & Associates, Seattle, WA, USA) and matching the model to the image set.

Table 4.3: Kinematic parameters determined by three different operators matching the same pose

	Orientation (°)				Humeral Head Position (mm)		
Operator #	β	α	γ	$\beta - \gamma$	x	y	z
1	49.29	26.67	54.09	-4.80	-38.00	-6.83	2.07
2	46.52	26.51	51.46	-4.93	-38.32	-5.39	1.66
3	45.63	26.78	50.15	-4.5	-38.57	-5.17	1.53
Avg. SD	0.75				0.49		

4.2.4 INTRA-OPERATOR RELIABILITY

The initial starting position of Orientation #1 was matched three times by the same operator. The kinematic parameters for all three trials are given in Table 4.4. Using β , α and $\beta - \gamma$, the average SDs for kinematic orientations and positions are 0.74° and 0.58 mm, respectively.

Table 4.4: Kinematic parameters determined by three different operators matching the same pose

	Orientation (°)				Humeral Head Position (mm)		
Trial #	β	α	γ	$\beta - \gamma$	x	y	z
1	49.29	26.67	54.09	-4.80	-38.00	-6.83	2.07
2	49.32	26.97	54.94	-4.62	-38.39	-6.36	1.46
3	48.21	27.14	51.71	-3.49	-39.09	-5.37	1.22
Avg. SD	0.74				0.58		

4.3 DOSAGE STUDY

Three-dimensional computer models were created for an *in vitro* shoulder using computer tomography (CT) protocols of varying dosage. CT Protocol #1 represents the current practice used for a typical shoulder CT, while CT Protocols #2 and #3 represent lower dose settings.

4.3.1 KINEMATICS

Glenohumeral kinematics were calculated for two different shoulder positions using 3D computer models derived from three different CT protocols. The accuracies of using the lower-dose conditions (CT Protocols #2 and #3) in measuring glenohumeral kinematics were evaluated through comparison with results obtained using the normal-dose condition (CT Protocol #1).

For Position #1, when using CT Protocol #2, the differences in measuring orientation and position ranged from -0.82° to 3.21° and -0.51 mm to -0.07 mm, respectively (Table 4.5). When CT Protocol #3 was employed similar kinematic differences were found, ranging from -0.80° to 2.32° for measuring orientations and from -0.77 mm to -0.46 mm for measuring positions.

Table 4.5: Difference in kinematic parameters when using CT Protocol #1 and CT Protocols #2 and #3, for Position #1

CT Protocol #	Difference in Orientation ($^{\circ}$)				Difference in Position (mm)		
	β	α	γ	$\beta - \gamma$	x	y	z
2	2.18	-0.82	3.21	-1.03	-0.51	-0.07	-0.50
3	0.78	-0.80	2.32	-1.59	-0.46	-0.77	-0.35

For Position #2, when using CT Protocol #2, the differences in measuring orientation and position ranged from -0.61° to 2.04° and -0.84 mm to 0.13 mm, respectively (Table 4.6). When CT Protocol #3 was employed, smaller kinematic differences were found when measuring orientations, ranging from -0.48° to -0.07° , and larger differences were found when measuring positions, ranging between -1.63 mm and -0.19 mm

Table 4.6: Difference in kinematic parameters between CT Protocol #1 and CT Protocols #2 and #3, for Position #2

CT Protocol #	Difference in Orientation ($^\circ$)				Difference in Position (mm)		
	β	α	γ	$\beta - \gamma$	x	y	z
2	2.04	-0.61	0.19	1.85	-0.84	0.13	-0.18
3	-0.40	-0.48	-0.32	-0.07	-1.63	-0.19	-0.62

The average RMSEs when using CT Protocol #2 to measure kinematic orientations and positions were 1.55° and 0.46 mm, respectively. For CT Protocol #3, the average RMSEs in measuring kinematic orientations and positions were 0.78° and 0.73 mm, respectively.

4.3.2 CT DOSAGE

The CT dose index (CTDI) and dose length product (DLP) were recorded for each CT Protocol (Table 4.7). One third of the tube current was used for CT Protocol #2 in comparison to CT Protocol #1 and one third of the tube current was used for CT Protocol #3 in comparison to CT Protocol #2. This same relationship exists for the CT dosage, as tube current directly affect the CT dosage.

Table 4.7: CTDI and DLP for CT Protocols #1, #2 and #3

CT Protocol #	CTDI (mGy)	DLP (mGy·cm)
1	33.76	770.69
2	11.25	256.90
3	3.75	85.63

4.3.3 3D MODEL CREATION AND LANDMARK DIGITIZATION

When creating the 3D models for each CT Protocol, automatic thresholding was first used to segment the CT slices. For CT Protocol #1, this thresholding worked very well and minor operator input was needed to modify the thresholding results in creating the 3D model.

Creating the 3D models and digitizing the bony landmarks required more user-input and data-processing for the lower-dose protocols. As more noise was present, the thresholding procedure did not accurately segment the bones from the surrounding tissue and a smoothing operation was required. Furthermore, with the additional noise it became difficult to determine the edges of bones and digitize the landmarks.

CHAPTER 5 – DISCUSSION

OVERVIEW: This chapter discusses the findings described in the previous chapter with respect to previously published literature. Specifically the results of the markerless radiostereometric analysis (RSA) validation study and the computed tomography (CT) dosage study are discussed.

5.1 VALIDATION STUDY

The accuracy of the markerless radiostereometric analysis (RSA) system in measuring skeletal kinematics was assessed against the “gold standards” of a precision cross-slide table (Model VCT 514; Sowa Tool and Machine Co. Ltd., Kitchener, ON, Canada) for kinematic translations and a standard RSA system (Kedgley, 2009a) for kinematic orientations. Shoulder bone models (Sawbones; Pacific Research Laboratories, Vashon, USA) were positioned in three orientations and at each orientation the humerus was translated relative to the fixed scapula.

5.1.1 KINEMATICS

Excellent agreement was found between the true (cross-slide table) and measured (markerless RSA) translations with intraclass correlation coefficients (ICCs) greater than 0.999 for all directions. The average root mean squared errors (RMSE) for translations in the anterior, inferior and posterior directions were 0.063 mm, 0.093 mm and 0.091 mm, respectively. The x-ray images acquired when translating the humerus in the inferior and posterior directions were substantially darker than the images acquired for the anterior

direction. It was more difficult to match the 3D bone models to these darker images, which is likely the cause of the increased RMSEs in these directions.

The average RMSE and standard error of measurement (SEM) for all translations were found to be 0.082 mm and 0.059 mm, respectively. In measuring orientations, the average RMSE and standard deviation (SD) were 1.18° and 1.22°, respectively. The translational accuracies are comparable to current RSA systems that use bi-planar fluoroscopy (Bey *et al.*, 2006; Li *et al.*, 2008), while the accuracies in determining kinematic orientations are comparable to the first implementations of many markerless RSA systems (Mahfouz *et al.*, 2003; You *et al.* 2001). The accuracies reported in this thesis will be evaluated against previously published validation studies; however, it can be difficult to directly compare accuracy results due to variations in experimental set-up and protocol.

5.1.1.1 MANUAL MATCHING

Li *et al.* (2004) reported an average markerless RSA error of 0.1 mm and 0.1° using a method based on manual matching. Unfortunately, in this study, only one position was analyzed and simplistic, easy to match phantoms were used, such as spheres and cylinders. The same research group reported an average error in displacement of 0.04 ± 0.06 mm (mean \pm SD) when conducting an *in vitro* study on a knee using a materials testing machine as the “gold standard” (DeFrate *et al.*, 2006). Accuracies in measuring kinematic orientations were not reported due to difficulties in finding a “gold standard” to measure relative kinematic orientations. Another study published by the same group reported mean errors within 0.11 mm and 0.24° when conducting a validation study on knee replacement components (Hanson *et al.*, 2006). This set-up was performed under

idealized conditions, as synthetically generated images were used as the “gold standard”. Most recently, Li *et al.* (2008) conducted a validation study to measure dynamic motion and reported mean *in vivo* errors of less than 0.15 mm and *in vitro* errors of less than 0.24 mm and 0.16°. The translational accuracies reported in this thesis are comparable to current markerless RSA systems performed with manual matching, while the accuracies in determining kinematic orientation are in general lower.

5.1.1.2 DIGITALLY RECONSTRUCTED RADIOGRAPHS

Accuracies reported using digitally reconstructed radiographs (DRRs) vary substantially based on the research group, experimental set-up and system version. The initial implementation of a system based on DRRs reported average RMSEs of 0.23 mm and 1.2° *in vitro* and 0.5 mm and 2.6° *in vivo* during dynamic motion of a canine tibia (You *et al.*, 2001). Subsequent implementations allowed the research group to report average RMSEs of 0.38 mm and 0.36° for dynamic *in vitro* shoulder motion (Bey *et al.*, 2006). When measuring *in vivo* knee motion RMSEs ranged from 0.04 mm to 0.23 mm and 0.18° to 0.85° for static trials and ranged between 0.23 mm and 0.88 mm and between 0.54° and 1.75° for running trials (Anderst *et al.*, 2009). The translational markerless RSA accuracies reported in this thesis are of the same order of magnitude as the previously mentioned systems based on DRRs, with rotational accuracies comparable to the first implementation of these systems. However, it is difficult to make a fair comparison to these published studies as most were conducted in a dynamic setting.

Another recently published validation study reported high accuracies when employing matching based on DRRs (de Bruin *et al.*, 2008). Using a scapula bone model and cadaveric scapula, measurements made using markerless RSA were compared to the

“gold standards” of a micromanipulator and standard RSA, respectively. The accuracies reported were less than 4 μm and 0.02° for the bone models and 0.08 mm and 0.02° for the cadaveric scapula. These accuracies surpass those reported in this thesis, and they provide a useful benchmark for accuracies obtainable using markerless RSA in ideal laboratory conditions.

5.1.1.3 SINGLE-PLANE

An initial implementation of a system based on DRRs using a single-plane set-up reported overall RMSEs of 0.65 mm for in-plane motion, 3.2 mm for out-of plane motion and 1.5° for rotations when conducting an *in vivo* experiment with an optical sensor as the “gold standard” (Mahfouz *et al.*, 2003). In a subsequent markerless RSA iteration, these errors decreased to approximately 0.05 mm, 1.05 mm and 0.1° for in-plane motion, out-of-plane motion and rotations, respectively (Mahfouz *et al.*, 2005).

For another semi-automated single-plane markerless RSA system, in-plane translational accuracy and rotational accuracy decreased respectively from 2 mm and 1.5° (Fregly *et al.*, 2005) to 0.53 mm and 0.54° in a future iteration (Moro-oka *et al.*, 2007). The translational accuracies in this thesis surpass the in-plane and especially out-of-plane accuracies reported by single-plane techniques. The rotational accuracies are comparable to the earlier implementations of single-plane markerless RSA techniques.

5.1.1.4 STANDARD RSA

Since markerless RSA is being proposed as a less invasive alternative to standard RSA, it is important to compare the accuracies reported in this thesis to standard RSA accuracies. Kedgley *et al.* (2009b) reported SEM values of 0.032 mm and 0.121° for a

standard RSA system. For the markerless RSA system, the SEM for translations was 0.059 mm, approximately double that of the standard RSA system. The SD of 1.22° in determining kinematic orientations for markerless RSA is an order of magnitude higher than the SEM reported for standard RSA. Even though the markerless RSA accuracies are lower than those reported with standard RSA, the markerless RSA system is a suitable alternative to standard RSA in situations where lower accuracies are tolerable and the implantation of beads is not feasible.

5.1.2 INTER-OPERATOR AND INTRA-OPERATOR RELIABILITY

The inter-operator and intra-operator reliabilities in matching a 3D computer model to an image set were very similar and found to be 0.75° and 0.74° in measuring orientations and 0.49 mm and 0.58 mm in measuring positions, respectively. The similarity of the two measures indicates that with minimal training, operators previously unfamiliar with the matching technique and Rhinoceros software (Robert McNeel & Associates, Seattle, WA, USA) can produce results that are as accurate as those produced by a skilled operator matching an image more than once. This is a promising result for future researchers who may use the markerless RSA system.

As part of a markerless RSA study to determine skeletal kinematics, five matching trials were conducted for five positions to determine reliability (Wang *et al.*, 2009). Standard deviations ranging from 0.11 mm to 0.26 mm and 0.42° to 0.89° were reported. It is unclear however, if the same operator conducted each matching trial. The reliability measures reported in this thesis are somewhat higher than those reported by Wang *et al.* (2009), but are still of the same order of magnitude.

5.2 DOSAGE STUDY

When performing markerless RSA it is necessary to create three-dimensional (3D) computer models of the bones of interest. CT scanning is a popular method used to create 3D models; however, it was uncertain how much CT dosage is required to create 3D models of sufficient accuracy for markerless RSA. In an effort to reduce the adverse effects of radiation exposure during CT scanning, this study analyzed the effect of lowering CT dosage on markerless RSA accuracy using a cadaveric shoulder. The specimen was scanned using a normal-dose (CT Protocol #1) and two lower-dose CT conditions (CT Protocols #2 and #3). A 3D computer model was created using each CT protocol and markerless RSA was performed for two glenohumeral joint positions. Using the normal-dose condition as the “gold standard”, RMSEs in measuring kinematic orientations and positions were calculated for the two lower-dose conditions. For CT Protocol #2, when the CT dosage was decreased by a third from the normal-dose condition, the average RMSEs for measuring kinematic orientations and positions were 1.55° and 0.46 mm, respectively. When the CT dosage was again decreased by a third, the average RMSEs were 0.78° and 0.73 mm. The accuracies for both the CT Protocols #2 and #3 will likely be acceptable for the majority of clinical studies conducted using the markerless RSA system.

As this is the first study to investigate the effect of lowering CT dosage on markerless RSA accuracy, it is difficult to find suitable studies with which to compare its results. The most relevant study was conducted by Oka *et al.* (2009) to investigate the effect of lowering CT dosage on performing upper limb reconstruction surgery using 3D computer models. Acceptable accuracies of less than 0.5 mm were achieved when the CT

dosage was lowered to one-thirtieth of the normal radiation dose. Since the CT dosage was reduced to one-ninth of the normal radiation dose in the study in this thesis, the research conducted by Oka *et al.* (2009) suggests that the CT dosage could potentially be further reduced while still maintaining acceptable RSA accuracies.

A negative consequence of decreasing the CT dosage is the increased difficulty and data processing required to create the 3D bone models and digitize the bony landmarks. It was found that as the CT dose was reduced, the processing required to create the 3D models increased, as smoothing operations were required.

For the normal-dose CT setting (Protocol #1), a CTDI and DLP of 33.76 mGy and 770.69 mGy·cm were reported, respectively. These data are higher than the reported CTDI of 19.49 ± 13.77 mGy and DLP of 315.96 ± 211.46 mGy·cm for a typical shoulder CT scan (Biswas *et al.*, 2009). The water used to simulate the soft tissue of the missing thorax was stored in a plastic container during CT scanning. The water container may have provided more interference than was necessary, which would lead to an increase in the dosage values and a degradation in the image quality.

CHAPTER 6 – GENERAL DISCUSSION AND CONCLUSIONS

OVERVIEW: This chapter summarizes the findings of the research program, outlines its strengths and limitations, and lists several recommendations for future work. The significance of this work is also highlighted.

6.1 SUMMARY

An accurate and non-surgical method to study three-dimensional (3D) skeletal kinematics was developed in this thesis. More specifically, a biplanar fluoroscopic markerless radiostereometric analysis (RSA) system was developed that is based on matching the bones under study to their shadows on two fluoroscopic images. In order to match the bones to the images, the shape of the bones and the experimental set-up (poses of the fluoroscope foci and image planes) were accurately reconstructed. Computed tomography (CT) scans of the bones were used to construct 3D computer models, on which bony landmarks were digitized to create clinically relevant coordinate systems. A calibration procedure was used to accurately determine the fluoroscope positions in 3D space, and using these data a virtual environment was created, in which the fluoroscope foci and images were positioned. The computer bone models were imported into the virtual environment and manually moved in 3D until their projections, from the points of view of the two fluoroscopic foci, matched the fluoroscopic images.

The accuracy of the system in determining kinematic translations and orientations was evaluated using the “gold standards” of a precision cross-slide table and a standard

RSA system, respectively. Intra-class correlation coefficients (ICCs) point to excellent agreement between actual (cross-slide table) and measured (markerless RSA) translations (ICCs > 0.999). The average root mean squared error (RMSE) and standard error of measurement (SEM) were 0.082 mm and 0.059 mm, respectively. Good agreement between actual (standard RSA) and measured (markerless RSA) kinematic orientations was found with a RMSE and standard deviation (SD) of 1.18° and 1.22°, respectively.

The effect of decreasing CT dosage on the accuracy of markerless RSA was investigated. It was found that by decreasing the dose length product (DLP) to a ninth of the normal-dose setting, the average RMSE in translation and rotation were 0.73 mm and 0.78° respectively. These accuracies are still within acceptable limits to be used in biomechanical studies.

6.2 LIMITATIONS

One limitation of the markerless RSA system described herein is that when conducting *in vivo* studies subjects will be exposed to ionizing radiation during both the CT scanning and fluoroscopic imaging. During a typical shoulder CT scan, subjects will be exposed to a computed tomography dose index and DLP of about 19 mGy and 316 mGy·cm, respectively (Bismas *et al.*, 2009). While every attempt will be made to minimize radiation exposure, this will always be a requirement of markerless RSA testing.

With the current system, the type of movement and number of joints that can be studied simultaneously are limited for future *in vivo* research. Due to the space constraints and small capture volume imposed by the fluoroscopes, usually only one joint and movements with a small range of motion can be studied.

There are limitations to the accuracy of the 3D model creation and markerless RSA calibration. The 3D bone models do not perfectly capture the bone geometry due to factors such as imperfect segmentation and smoothing that occurs when creating the triangular mesh. Calibration is limited due to factors such as errors in the calibration frame and distortion grid manufacturing, digitization process and distortion correction process. While these errors are difficult to quantify individually, they have been quantified all together as a standard error of measurement of 0.032 mm for translations and 0.121° for rotations (Kedgley *et al.*, 2009c).

Performing the markerless RSA calibration procedure is a time-consuming process and requires an investigator who is comfortable deriving new calibration equations for new experimental set-ups, running software in Maple (Maplesoft, Waterloo, ON, Canada), MATLAB (The MathWorks, Natick, MA, USA) and Rhinoceros (Robert McNeel & Associates, Seattle, WA, USA) and modeling the experimental set-up in Rhinoceros. These constraints will tend to limit the number of investigators who can perform markerless RSA to only those with extensive training, which will limit its immediate clinical application.

The matching procedure is also an operator-intensive task with several limitations of its own. In order to determine skeletal kinematics, an operator manually matches the 3D model of a bone to two fluoroscopic images. This matching procedure is constrained by an operator's ability to detect different pixel shades, as the operator must determine the exact edge of a bone on each image. Matching is also affected by the patience of the operator, as it can take up to several hours to match a bone to two images. While the matching process has proven accurate, it is somewhat subjective and varies based on an

operator's perception of a "matched" 3D model, as demonstrated with an intra-operator reliability of 0.58 mm and 0.74° and an inter-operator reliability of 0.49 mm and 0.75°.

The markerless RSA system was validated using bone models in static positions. However, this system is expected to be used to study dynamic *in vivo* skeletal kinematics, which is a different testing scenario. It has been shown that as speed increases, markerless RSA accuracy decreases (Anderst *et al.*, 2009; Li *et al.*, 2008). The matching procedure will also likely be more difficult in an *in vivo* setting due to soft tissue interference and motion-blur on the images. For the validation study conducted, the scapula was matched only once, as it was fixed, while the humerus was re-matched for each new position analyzed. When studying *in vivo* shoulder kinematics, both the humerus and scapula will need to be re-matched for each new position under study, likely decreasing the accuracy of the system.

A limitation of the CT study is that it was conducted *in vitro* and water was used to simulate the missing soft tissue of half the thorax. Water-phantoms are commonly used to simulate tissue (Bomford, 2003), however the plastic water container may have provided more interference than was needed, which increased the reported x-ray dosage. The age of the cadaver (76 years old) was also not representative of the middle-aged subjects generally seen in the Wolf Orthopaedic Quantitative Imaging Laboratory (WOQIL). A final limitation is the small sample size of only one subject, however, it should be noted that this is the preliminary data of a larger study which is not yet complete.

6.3 STRENGTH

The strengths of this research are that a non-surgical and accurate method to study 3D skeletal kinematics was developed with an average RMSE of 0.082 mm and 1.18°. Using anatomically accurate bone phantoms (Sawbones; Pacific Research Laboratories Inc., Vashon, WA, USA), the accuracy of both kinematic translations and orientations were evaluated against the “gold standards” of a precision cross-slide table and standard RSA, respectively. The markerless RSA system was rigorously validated, especially when compared to previously reported markerless RSA validations in the literature that used simplistic phantoms, such as spheres and cylinders (Li *et al.*, 2004), only reported repeatability when validating kinematic orientations (Asano *et al.*, 2001; DeFrate *et al.*, 2006), used synthetic computer generated images as the “gold standard” (Bingham & Li, 2006; Fregly *et al.*, 2005; Hanson *et al.*, 2006; Moro-oka *et al.*, 2007) and only reported translations and orientations in a global coordinate system (Hanson *et al.*, 2006).

The translational accuracies are comparable to current measurements with bi-planar fluoroscopic RSA systems that use manual matching (0.24 mm and 0.16° accuracy; Li *et al.*, 2008) and intensity-based matching (0.4 mm and 0.4° accuracy; Bey *et al.*, 2006) and single-plane automated systems (0.53 mm and 0.54° accuracy; Moro-oka *et al.*, 2007). The orientation accuracies are comparable to “first generation” markerless RSA systems, such as intensity-based matching (0.23 mm and 1.2° accuracy; You *et al.*, 2001) and single-plane automated systems (2 mm and 1.5° accuracy; Fregly *et al.*, 2005).

This was also the first reported study to examine the effect of CT dosage on markerless RSA accuracies, in an effort to reduce radiation exposure to subjects. The findings of this study allow the radiation dosage from CT scanning to be reduced to a

ninth from the current practice, while still achieving acceptable accuracies for most clinical studies.

6.4 RECOMMENDATIONS AND FUTURE DIRECTIONS

In order to increase the fluoroscopic capture volume to allow for a greater variety of *in vivo* studies to be conducted, it is recommended that new fluoroscopes with larger image intensifiers (IIs) be purchased. It is also recommended that flat-panel IIs be purchased, which would avoid the need to perform image distortion correction, and therefore likely reduce calibration and matching errors.

If the current fluoroscopes are used, it is recommended that as well as the calibration points, the entire fluoroscopic images be distortion-corrected. The effects of distortion are not obvious when viewing the fluoroscopic images being matched. During the final stages of matching however, the images are zoomed in closely to an anatomical landmark, where small adjustments to the image could have significant consequences to the quality of the match.

It is also recommended that steps be taken to improve the manual markerless RSA matching procedure. In the future, edge detection should be performed to outline the bones on the images before matching occurs. These outlines will reduce the subjectivity of matching because operators will not have to estimate the edge of a bone contour. An effort should also be made to calculate and display the mean distance between the bony outline on an image and projected silhouette in real-time. A minimum allowable mean distance should then be investigated and set as a matching criterion to further decrease the subjectivity of the matching procedure.

If a less operator-intensive method is desired, it is recommended that a method based on semi-automated matching be developed, specifically a method based on digitally reconstructed radiographs (DRR). An operator would determine an initial pose of each bone and then DRRs would be used to find the final pose. Matching based on DRR has proven to be the most accurate automated matching method for studying a wide range of skeletal kinematics in a variety of settings (Bey *et al.*, 2006; de Bruin *et al.*, 2008). This recommendation should be followed when significant time and computer power can be devoted to the project, due to the complexity and numerical intensity of performing matching based on DRRs.

It is recommended that further attempts be made to reduce the radiation exposure to subjects during the markerless RSA process. Using generic 3D computer bone models instead of 3D computer models created from CT scans, would drastically reduce radiation exposure to the subjects. The generic bone models would be scaled anthropometrically based on key anatomical landmarks for each subject and the accuracy of markerless RSA would need to be re-evaluated. The use of magnetic resonance imaging (MRI) derived bone models is another method to reduce radiation exposure. Even though lower accuracies have been reported using MRI-derived bone models (Moro-oka *et al.*, 2007; Wang *et al.*, 2008), thus far the differences in accuracies have only been proven to be significant in a single-plane RSA set-up (Moro-oka *et al.*, 2007). It is recommended to investigate if the lower accuracies associated with MRI-derived bone models are sufficient to warrant future research in the WOQIL with this method.

The markerless RSA system will be used in the WOQIL to study dynamic *in vivo* kinematics. It is therefore recommended that a validation study be conducted to

determine the effect of both speed and *in vivo* conditions on the accuracy of markerless RSA, using standard RSA as the “gold standard”.

6.5 SIGNIFICANCE

With the development of the markerless RSA system, a much broader scope of clinical biomechanical research can be conducted in the WOQIL. Previous studies were limited to investigating skeletal kinematics following a surgical intervention. With the markerless RSA system, kinematics can be analyzed not only before a surgery is conducted, but also on a normal subject population to evaluate the success of an intervention to restore normal joint function.

Markerless RSA has numerous applications in fields such as orthopaedics, physiotherapy and sport biomechanics. The system can be used to study the effect of a wide range of interventions from joint arthroplasty and reconstructive surgeries to braces and orthotics. The markerless RSA system developed in this thesis has the potential to answer a broad range of biomechanical questions and thus significantly contribute to the field of biomechanics.

REFERENCES

- Anderst, W., Zauel, R., Bishop, J., Demps, E., & Tashman, S. (2009). Validation of three-dimensional model-based tibio-femoral tracking during running. *Medical Engineering & Physics*, 31(1), 10-16.
- Aronson, A. S., Jonsson, N., & Alberius, P. (1985). Tantalum markers in radiography. *Skeletal Radiology*, 14(3), 207-211.
- Asano, T., Akagi, M., Tanaka, K., Tamura, J., & Nakamura, T. (2001). In vivo three-dimensional knee kinematics using a biplanar image-matching technique. *Clinical Orthopaedics and Related Research*, (388), 157-166.
- Asano, T., Akagi, M., & Nakamura, T. (2005). The functional flexion-extension axis of the knee corresponds to the surgical epicondylar axis: in vivo analysis using a biplanar image-matching technique. *The Journal of Arthroplasty*, 20(8), 1060-1067.
- Bahk, M., Keyurapan, E., Tasaki, A., Sauers, E. L., & McFarland, E. G. (2007). Laxity testing of the shoulder: a review. *The American Journal of Sports Medicine*, 35(1), 131-144.
- Baldursson, H., Egund, N., Hansson, L. I., & Selvik, G. (1979). Instability and wear of total hip prostheses determined with roentgen stereophotogrammetry. *Archives of Orthopaedic and Traumatic Surgery. Archiv Für Orthopädische Und Unfall-Chirurgie*, 95(4), 257-263.
- Banks, S. A., & Hodge, W. A. (1996). Accurate measurement of three-dimensional knee replacement kinematics using single-plane fluoroscopy. *IEEE Transactions on Bio-medical Engineering*, 43(6), 638-649.
- Berthonnaud, E., Herzberg, G., Zhao, K. D., An, K. N., & Dimnet, J. (2005). Three-dimensional in vivo displacements of the shoulder complex from biplanar radiography. *Surgical and Radiologic Anatomy*, 27(3), 214-222..
- Bey, M. J., Zauel, R., Brock, S. K., & Tashman, S. (2006). Validation of a new model-based tracking technique for measuring three-dimensional, in vivo glenohumeral joint kinematics. *Journal of Biomechanical Engineering*, 128(4), 604-609.
- Bey, M. J., Kline, S. K., Zauel, R., Lock, T. R., & Kolowich, P. A. (2008). Measuring dynamic in-vivo glenohumeral joint kinematics: technique and preliminary results. *Journal of Biomechanics*, 41(3), 711-4.
- Bingham, J. T. (2006) An automated matching algorithm for dual orthogonal fluoroscopy. Thesis, Massachusetts Institute of Technology, Cambridge.

- Bingham, J., & Li, G. (2006). An optimized image matching method for determining in-vivo TKA kinematics with a dual-orthogonal fluoroscopic imaging system. *Journal of Biomechanical Engineering*, 128(4), 588-95.
- Biswas, D., Bible, J. E., Bohan, M., Simpson, A. K., Whang, P. G., & Grauer, J. N. (2009). Radiation Exposure from Musculoskeletal Computerized Tomographic Scans. *Journal of Bone and Joint Surgery*, 91(8), 1882-1889.
- Bland, J.M. & Altman, D.G. (1986) Statistical methods for assessing agreement between two methods of clinical measurement. *Lancet* 1, 307–310.
- Bomford, K. (2003). Principles of radiation treatment planning. In C. K. Bomford and I. H. Kunkler (Eds.), *Walter and Miller's textbook of radiotherapy: radiation physics, therapy and oncology* (5th ed.) (pp. 191-206). London: Churchill Livingstone.
- Börlin, N., Thien, T., & Kärrholm, J. (2002). The precision of radiostereometric measurements. Manual vs. digital measurements. *Journal of Biomechanics*, 35(1), 69-79.
- Bushberg, J. T., Seibert, J. A., Leidholdt Jr., E. M. & Boone, J. M. (2002) *The Essential Physics of Medical Imaging*. (2nd ed.). Philadelphia: Lippincott Williams & Wilkins.
- Bylander, B., Aronson, S., Egund, N., Hansson, L. I., & Selvik, G. (1981). Growth disturbance after physial injury of distal femur and proximal tibia studied by roentgen stereophotogrammetry. *Archives of Orthopaedic and Traumatic Surgery. Archiv Für Orthopädische Und Unfall-Chirurgie*, 98(3), 225-235.
- Canny, J. (1986). A computational approach to edge detection. *IEEE Transactions on Pattern Analysis and Machine Intelligence*, 8(6), 679-698.
- Ciccotti, M. G., Rothman, R. H., Hozack, W. J., & Moriarty, L. (1994). Clinical and roentgenographic evaluation of hydroxyapatite-augmented and nonaugmented porous total hip arthroplasty. *The Journal of Arthroplasty*, 9(6), 631-639.
- Conti, S., Lalonde, K. A., & Martin, R. (2006). Kinematic analysis of the agility total ankle during gait. *Foot & Ankle International*, 27(11), 980-984.
- Culham, E., & Peat, M. (1993). Functional anatomy of the shoulder complex. *The Journal of Orthopaedic and Sports Physical Therapy*, 18(1), 342-350.
- de Asla, R. J., Wan, L., Rubash, H. E., & Li, G. (2006). Six DOF in vivo kinematics of the ankle joint complex: Application of a combined dual-orthogonal fluoroscopic and magnetic resonance imaging technique. *Journal of Orthopaedic Research*, 24(5), 1019-1027.
- de Bruin, P. W. D., Kaptein, B. L., Stoel, B. C., Reiber, J. H., Rozing, P. M., & Valstar, E. R. (2008). Image-based RSA: Roentgen stereophotogrammetric analysis based on 2D-3D image registration. *Journal of Biomechanics*, 41(1), 155-164.

- DeFrate, L. E., Papannagari, R., Gill, T. J., Moses, J. M., Pathare, N. P., & Li, G. (2006). The 6 degrees of freedom kinematics of the knee after anterior cruciate ligament deficiency: an in vivo imaging analysis. *The American Journal of Sports Medicine*, 34(8), 1240-1246.
- Della Valle, C. J., Rokito, A. S., Birdzell, M. G., & Zuckerman, J.D. (2001). Biomechanics of the shoulder. In M. Nordin., & V. H. Frankel (Eds.), *Basic Biomechanics of the Musculoskeletal System*. (3rd ed.) (pp. 318-339). Philadelphia: Lippincott Williams & Wilkins.
- Dennis, D. A., Komistek, R. D., Hoff, W. A., & Gabriel, S. M. (1996). In vivo knee kinematics derived using an inverse perspective technique. *Clinical Orthopaedics and Related Research*, (331), 107-117.
- Downing, M. R., Ashcroft, P. B., Johnstone, A. J., Bach, O., Mackenzie, S., & Ashcroft, G. P. (2008). Assessment of inducible fracture micromotion in distal radial fractures using radiostereometry. *Journal of Orthopaedic Trauma*, 22(8 Suppl), S96-105.
- Dunbar, M. J., Wilson, D. A. J., Hennigar, A. W., Amirault, J. D., Gross, M., & Reardon, G. P. (2009). Fixation of a trabecular metal knee arthroplasty component. A prospective randomized study. *The Journal of Bone and Joint Surgery*. American Volume, 91(7), 1578-1586.
- Edixhoven, P., Huiskes, R., de Graaf, R., van Rens, T. J., & Slooff, T. J. (1987). Accuracy and reproducibility of instrumented knee-drawer tests. *Journal of Orthopaedic Research*, 5(3), 378-387.
- Fregly, B. J., Rahman, H. A., & Banks, S. A. (2005). Theoretical accuracy of model-based shape matching for measuring natural knee kinematics with single-plane fluoroscopy. *Journal of Biomechanical Engineering*, 127(4), 692-9.
- Garling, E. H., Kaptein, B. L., Geleijns, K., Nelissen, R. G. H. H., & Valstar, E. R. (2005). Marker Configuration Model-Based Roentgen Fluoroscopic Analysis. *Journal of Biomechanics*, 38(4), 893-901.
- Gronenschild, E. (1997). The accuracy and reproducibility of a global method to correct for geometric image distortion in the x-ray imaging chain. *Medical Physics*, 24(12), 1875-1888.
- Hamai, S., Miura, H., Higaki, H., Shimoto, T., Matsuda, S., Okazaki, K., & Iwamoto, Y. (2008). Three-dimensional knee joint kinematics during golf swing and stationary cycling after total knee arthroplasty. *Journal of Orthopaedic Research*, 26(12), 1556-1561.
- Hanson, G. R., Suggs, J. F., Freiberg, A. A., Durbhakula, S., & Li, G. (2006). Investigation of in vivo 6DOF total knee arthroplasty kinematics using a dual orthogonal fluoroscopic system. *Journal of Orthopaedic Research*, 24(5), 974-981.

- Hendee, W. R. & Ritenour, E. R. (2002). *Medical Imaging Physics*. (4th ed.). New York: Wiley-Liss, Inc.
- Hoff, W. A., Komistek, R. D., Dennis, D. A., Gabriel, S. M., & Walker, S. A. (1998). Three-dimensional determination of femoral-tibial contact positions under in vivo conditions using fluoroscopy. *Clinical biomechanics*, 13(7), 455-472.
- Holdsworth, D. W., Pollmann, S. I., Nikolov, H. N., & Fahrig, R. (2005). Correction of XRII geometric distortion using a liquid-filled grid and image subtraction. *Medical Physics*, 32(1), 55-64.
- Hurschler, C., Seehaus, F., Emmerich, J., Kaptein, B. L., & Windhagen, H. (2009). Comparison of the model-based and marker-based roentgen stereophotogrammetry methods in a typical clinical setting. *The Journal of Arthroplasty*, 24(4), 594-606.
- Itoi, E., Hsu, H. C., & An, K. N. (1996). Biomechanical investigation of the glenohumeral joint. *Journal of Shoulder and Elbow Surgery*, 5(5), 407-424.
- Jonsson, H., & Kärrholm, J. (1990). Brace effects on the unstable knee in 21 cases. A roentgen stereophotogrammetric comparison of three designs. *Acta Orthopaedica Scandinavica*, 61(4), 313-318.
- Jonsson, H., & Kärrholm, J. (1999). Three-dimensional knee kinematics and stability in patients with a posterior cruciate ligament tear. *Journal of Orthopaedic Research*, 17(2), 185-191.
- Kaptein, B. L., Valstar, E. R., Stoel, B. C., Rozing, P. M., & Reiber, J. H. (2003). A new model-based RSA method validated using CAD models and models from reversed engineering. *Journal of Biomechanics*, 36(6), 873-882.
- Kaptein, B. L., Valstar, E. R., Stoel, B. C., Rozing, P. M., & Reiber, J. H. C. (2004). Evaluation of three pose estimation algorithms for model-based roentgen stereophotogrammetric analysis. *Proceedings of the Institution of Mechanical Engineers. Part H, Journal of Engineering in Medicine*, 218(4), 231-238.
- Kaptein, B. L., Valstar, E. R., Spoor, C. W., Stoel, B. C., & Rozing, P. M. (2006). Model-based RSA of a femoral hip stem using surface and geometrical shape models. *Clinical Orthopaedics and Related Research*, 448, 92-97.
- Kärrholm, J., Hansson, L. I., Laurin, S., & Selvik, G. (1983). Post-traumatic growth disturbance of the ankle treated by the Langenskiöld procedure. Evaluation by radiography, roentgen stereophotogrammetry, scintimetry and histology: case report. *Acta Orthopaedica Scandinavica*, 54(5), 721-729.
- Kärrholm, J., Selvik, G., Elmqvist, L. G., Hansson, L. I., & Jonsson, H. (1988). Three-dimensional instability of the anterior cruciate deficient knee. *The Journal of Bone and Joint Surgery. British Volume*, 70(5), 777-783.

- Kärrholm, J., Gill, R. H. S., & Valstar, E. R. (2006). The history and future of radiostereometric analysis. *Clinical Orthopaedics and Related Research*, 448, 10-21.
- Kedgley, A. E. (2009a) Development of a fluoroscopic radiostereometric analysis system with an application to glenohumeral joint kinematics. Ph.D. Thesis, University of Western Ontario, London.
- Kedgley, A. E., Birmingham, T., & Jenkyn, T. R. (2009b). Comparative accuracy of radiostereometric and optical tracking systems. *Journal of Biomechanics*, 42(9), 1350-1354.
- Kedgley, A. E., & Jenkyn, T. R. (2009c). RSA calibration accuracy of a fluoroscopy-based system using nonorthogonal images for measuring functional kinematics. *Medical Physics*, 36(7), 3176-3180.
- Kiss, J., Murray, D. W., Turner-Smith, A. R., Bithell, J., & Bulstrode, C. J. (1996). Migration of cemented femoral components after THR. Roentgen stereophotogrammetric analysis. *The Journal of Bone and Joint Surgery*. British Volume, 78(5), 796-801.
- Kölzow, T., & Krüger, L. (2002). Matching of a 3D model into a 2D image using a hypothesize and test alignment method. In *Advanced Signal Processing Algorithms, Architectures, and Implementations XII* (Vol. 4791, pp. 222-232). Presented at the Advanced Signal Processing Algorithms, Architectures, and Implementations XII, Seattle, WA, USA: SPIE.
- Komistek, R. D., Stiehl, J. B., Buechel, F. F., Northcut, E. J., & Hajner, M. E. (2000). A determination of ankle kinematics using fluoroscopy. *Foot & Ankle International*, 21(4), 343-350.
- Komistek, R. D., Dennis, D. A., & Mahfouz, M. (2003). In vivo fluoroscopic analysis of the normal human knee. *Clinical Orthopaedics and Related Research*, (410), 69-81.
- Lemieux, L., Jagoe, R., Fish, D. R., Kitchen, N. D., & Thomas, D. G. (1994). A patient-to-computed-tomography image registration method based on digitally reconstructed radiographs. *Medical Physics*, 21(11), 1749-1760.
- Li, G., Wuerz, T. H., & DeFrate, L. E. (2004). Feasibility of using orthogonal fluoroscopic images to measure in vivo joint kinematics. *Journal of Biomechanical Engineering*, 126(2), 314-318.
- Li, G., Velde, S. K. V. D., & Bingham, J. T. (2008). Validation of a non-invasive fluoroscopic imaging technique for the measurement of dynamic knee joint motion. *Journal of Biomechanics*, 41(7), 1616-1622.
- Löfvenberg, R., Kärrholm, J., Selvik, G., Hansson, L. I., & Ahlgren, O. (1989). Chronic lateral instability of the ankle. Roentgen stereophotogrammetry of talar position. *Acta Orthopaedica Scandinavica*, 60(1), 34-39.

Löfvenberg, R., Kärrholm, J., & Ahlgren, O. (1994). Ligament reconstruction for ankle instability. A 5-year prospective RSA follow-up of 30 cases. *Acta Orthopaedica Scandinavica*, 65(4), 401-407.

Lugo, R., Kung, P., & Ma, C. B. (2008). Shoulder biomechanics. *European Journal of Radiology*, 68(1), 16-24.

Mahfouz, M. R., Hoff, W. A., Komistek, R. D., & Dennis, D. A. (2003). A robust method for registration of three-dimensional knee implant models to two-dimensional fluoroscopy images. *IEEE Transactions on Medical Imaging*, 22(12), 1561-1574.

Mahfouz, M. R., Komistek, R. D., Dennis, D. A., & Hoff, W. A. (2004). In vivo assessment of the kinematics in normal and anterior cruciate ligament-deficient knees. *The Journal of Bone and Joint Surgery*. American Volume, 86-A Suppl 2, 56-61.

Mahfouz, M., Nicholson, G., Komistek, R., Hovis, D., & Kubo, M. (2005). In vivo determination of the dynamics of normal, rotator cuff-deficient, total, and reverse replacement shoulders. *The Journal of Bone and Joint Surgery*. American volume, 87 Suppl 2, 107-113.

Malchau, H., Kärrholm, J., Wang, Y. X., & Herberts, P. (1995). Accuracy of migration analysis in hip arthroplasty. Digitized and conventional radiography, compared to radiostereometry in 51 patients. *Acta Orthopaedica Scandinavica*, 66(5), 418-424.

Michael, G. (2001). X-ray computed tomography. *Medical Physics*, 36(6), 442-451.

Moro-oka, T. A., Hamai, S., Miura, H., Shimoto, T., Higaki, H., Fregly, B. J., et al. (2007). Can magnetic resonance imaging-derived bone models be used for accurate motion measurement with single-plane three-dimensional shape registration? *Journal of Orthopaedic Research*, 25(7), 867-872.

Nelissen, R. G., Valstar, E. R., & Rozing, P. M. (1998). The effect of hydroxyapatite on the micromotion of total knee prostheses. A prospective, randomized, double-blind study. *The Journal of Bone and Joint Surgery*. American Volume, 80(11), 1665-1672.

Nishinaka, N., Tsutsui, H., Mihara, K., Suzuki, K., Makiuchi, D., Kon, Y., Wright, T.W., Moser, M.W., Gamada, K., Sugimoto, H., & Banks, S.A. (2008). Determination of in vivo glenohumeral translation using fluoroscopy and shape-matching techniques. *Journal of Shoulder and Elbow Surgery*, 17(2), 319-322.

Nobuhara, K. (2003). *The shoulder: its Function and Clinical Aspects*. River Edge, NJ: World Scientific Publishing Co. Pte. Ltd.

Oka, K., Murase, T., Moritomo, H., Goto, A., Sugamoto, K., & Yoshikawa, H. (2009). Accuracy analysis of three-dimensional bone surface models of the forearm constructed from multidetector computed tomography data. *The International Journal of Medical Robotics + Computer Assisted Surgery*

Olsson, T. H., Selvik, G., & Willner, S. (1976). Kinematic analysis of spinal fusions. *Investigative Radiology*, 11(3), 202-209.

Petersson, C. J., & Redlund-Johnell, I. (1983). Joint space in normal gleno-humeral radiographs. *Acta Orthopaedica Scandinavica*, 54(2), 274-276.

Pheasant, S. & Haslegrave, C. M. (2006) *Bodyspace: anthropometry, ergonomics, and the design of work* (3rd ed.). Boca Raton: Taylor and Francis Group, LLC.

Prescher, A. (2000). Anatomical basics, variations, and degenerative changes of the shoulder joint and shoulder girdle. *European Journal of Radiology*, 35(2), 88-102.

Rougée, A., Picard, C., Ponchut, C., & Troussel, Y. (1993). Geometrical calibration of x-ray imaging chains for three-dimensional reconstruction. *Computerized Medical Imaging and Graphics*, 17(4-5), 295-300.

Rune, B., Selvik, G., Kreiborg, S., Sarnäs, K. V., & Kågström, E. (1979). Motion of bones and volume changes in the neurocranium after craniectomy in Crouzon's disease. A roentgen stereometric study. *Journal of Neurosurgery*, 50(4), 494-498.

Selvik, G. (1989). Roentgen stereophotogrammetry. A method for the study of the kinematics of the skeletal system. *Acta Orthopaedica Scandinavica*. Supplemental, 232, 1-51.

Shrout, P.E. & Fleiss, J.L. (1979) Intraclass correlations: uses in assessing rater reliability. *Psychological Bulletin*, 86, 420-428.

Silverman, P. M., Kalender, W. A., & Hazle, J. D. (2001). Common terminology for single and multislice helical CT. *AJR. American Journal of Roentgenology*, 176(5), 1135-1136.

Streiner, D.L. & Norman, G.R. (1995) *Health Measurement Scales: A Practical Guide to their Development and Use*. Oxford University Press, New York.

Valstar, E. R., Spoor, C. W., Nelissen, R. G., & Rozing, P. M. (1997). Roentgen stereophotogrammetric analysis of metal-backed hemispherical cups without attached markers. *Journal of Orthopaedic Research*, 15(6), 869-873.

Valstar, E. R., de Jong, F. W., Vrooman, H. A., Rozing, P. M., & Reiber, J. H. (2001). Model-based Roentgen stereophotogrammetry of orthopaedic implants. *Journal of Biomechanics*, 34(6), 715-22.

Valstar, E. R., Gill, R., Ryd, L., Flivik, G., Börllin, N., & Kärrholm, J. (2005). Guidelines for standardization of radiostereometry (RSA) of implants. *Acta Orthopaedica*, 76(4), 563-572.

Van de Velde, S. K., DeFrate, L. E., Gill, T. J., Moses, J. M., Papannagari, R., & Li, G. (2007). The effect of anterior cruciate ligament deficiency on the in vivo elongation of

the medial and lateral collateral ligaments. *The American Journal of Sports Medicine*, 35(2), 294-300.

van Doorn, W. J., ten Have, B. L. E. F., van Biezen, F. C., Hop, W. C. J., Ginai, A. Z., & Verhaar, J. A. N. (2002). Migration of the femoral stem after impaction bone grafting. First results of an ongoing, randomised study of the exeter and elite plus femoral stems using radiostereometric analysis. *The Journal of Bone and Joint Surgery*. British Volume, 84(6), 825-831.

Wang, S., Passias, P., Li, G., Li, G., & Wood, K. (2008). Measurement of vertebral kinematics using noninvasive image matching method-validation and application. *Spine*, 33(11), E355-61.

Wang, S., Xia, Q., Passias, P., Wood, K., & Li, G. (2009). Measurement of geometric deformation of lumbar intervertebral discs under in-vivo weightbearing condition. *Journal of Biomechanics*, 42(6), 705-711.

Wu, G., van der Helm, F. C. T., Veeger, H. E. J., Makhsous, M., van Roy, P., Anglin, C., Nagels, J., Karduna, A. R., Mcquade, K., Wang, X. G., Werner, F. W., Buchholz, B., (2005). ISB recommendation on definitions of joint coordinate systems of various joints for the reporting of human joint motion-Part II: shoulder, elbow, wrist and hand. *Journal of Biomechanics*, 38(5), 981-992.

Yaffe, M. J., & Rowlands, J. A. (1997). X-ray detectors for digital radiography. *Physics in Medicine and Biology*, 42(1), 1-39.

Yamaguchi, S., Sasho, T., Kato, H., Kuroyanagi, Y., & Banks, S. A. (2009). Ankle and subtalar kinematics during dorsiflexion-plantarflexion activities. *Foot & Ankle International*, 30(4), 361-366.

You, B. M., Siy, P., Anderst, W., & Tashman, S. (2001). In vivo measurement of 3-D skeletal kinematics from sequences of biplane radiographs: application to knee kinematics. *IEEE Transactions on Medical Imaging*, 20(6), 514-525.

Yuan, X., Drangova, M., Pollmann, S., Miron, R., Bourne, R., & Holdsworth, D. (2004). Comparison of a digital flat panel, x-ray image intensifier and conventional film-screen system for radiostereometric analysis (RSA). *In Proceedings of SPIE - The International Society for Optical Engineering*, Vol. 5368, pp. 914-921.

Zuffi, S., Leardini, A., Catani, F., Fantozzi, S., & Cappello, A. (1999). A model-based method for the reconstruction of total knee replacement kinematics. *IEEE Transactions on Medical Imaging*, 18(10), 981-91.

APPENDIX A – PIXEL SIZE CALCULATION

A.1 PIXEL GRID DRAWING

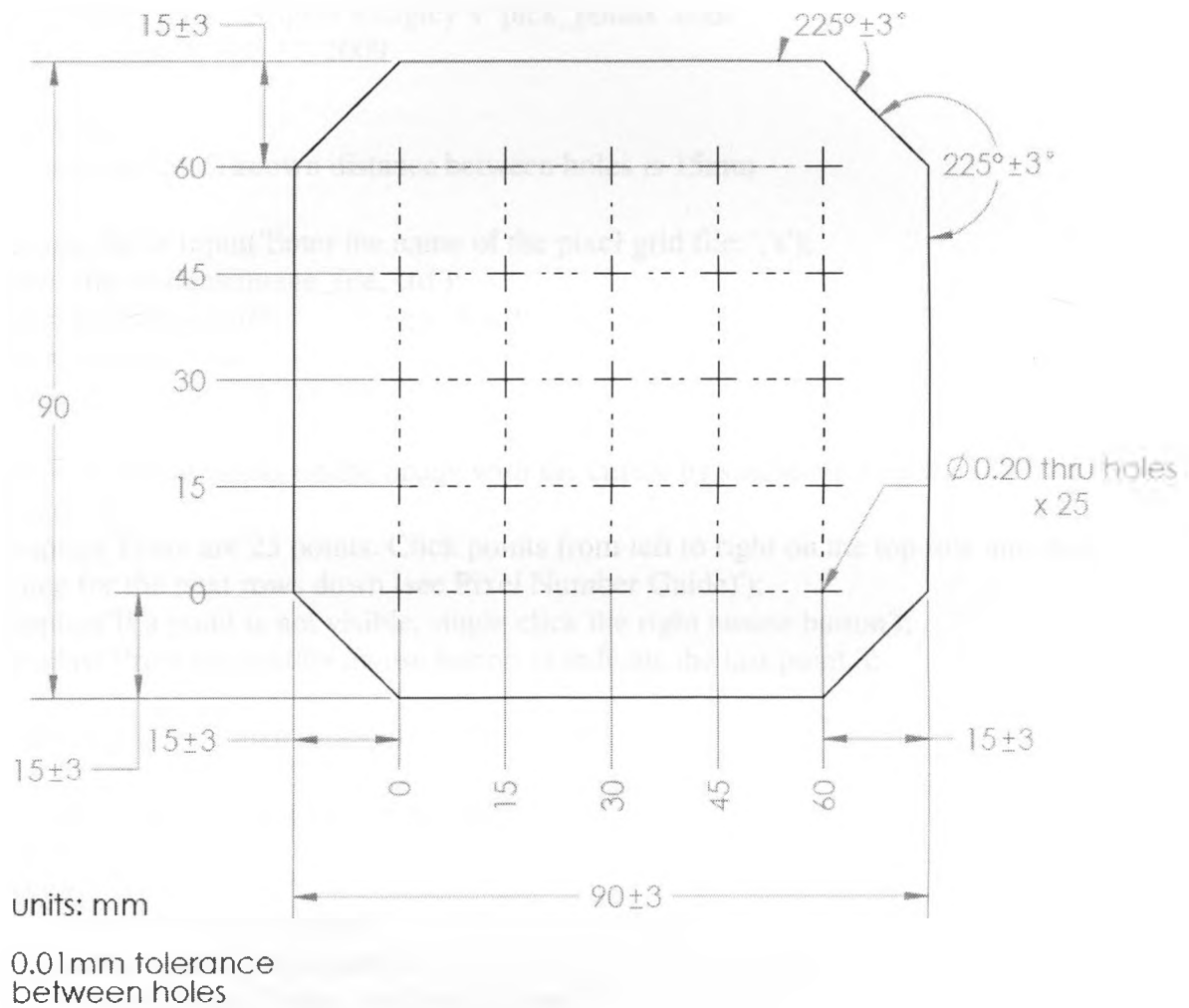


Figure A.1: Pixel grid drawing

A.2 PIXEL SIZE CALCULATOR CODE

```
%Program Name: Pixel_Size_Calculator.m
%Determines the pixel size based on the known distance between holes(15mm)
%Created by: Anne-Marie Allen
%Modified from: Angela Kedgley's 'pick_points' code
%Date created: Feb 17, 2009

drawnow;
known_d=15; %known distance between holes is 15mm

image_file = input('Enter the name of the pixel grid file: ','s');
new_file = strcat(image_file, '.tif');
im = imread(strcat('C:\.... \', new_file));
im = rgb2gray(im);
im = imcrop(im,[105 15 510 450]);

display('Select points on the image with the cursor by single-clicking the left mouse
button. ');
display('There are 25 points. Click points from left to right on the top row and then do the
same for the next rows down (see Pixel Number Guide)');
display('If a point is not visible, single click the right mouse button');
display('Press the middle mouse button to indicate the last point. ');

colormap(gray(256)); image(im); axis image

% Allow the user to select the points
counter = 1;
while 1
    names(counter) = counter;
    points(counter,:) = ginput(1);
    if strcmp(get(gcf,'SelectionType'),'extend')
        break
    end

    if strcmp(get(gcf,'SelectionType'),'alt')
        points(counter,:) = 5555;
    end
    counter = counter + 1;
end

%Determines pixel value of point selected
for n=1:1:counter
    if points(n,1)~=5555 & points(n,2)~=5555
        pixRGB_orig(n,1:3) = impixel(im,points(n,1),points(n,2));
```

```

else
    pixRGB_orig(n,1:3) = 5555;
end

% Create subsets of the image surrounding each point
for n = 1:1:counter
    if points(n,1)~=5555 & points(n,2)~=5555
        xmax(n,:) = round(points(n,1)) + 10;
        xmin(n,:) = round(points(n,1)) - 10;
        ymax(n,:) = round(points(n,2)) + 10;
        ymin(n,:) = round(points(n,2)) - 10;
    else
        xmax(n,1) = 5555;
        xmin(n,1) = 5555;
        ymax(n,1) = 5555;
        ymin(n,1) = 5555;
    end
end

% Finds the lightest pixel within each subset
for n = 1:1:counter
    if points(n,1)~=5555 & points(n,2)~=5555
        %impixel determines the pixel colour value
        pixRGB(n,:)=impixel(im,xmin(n),ymin(n));
        for x = xmin(n,:):1:xmax(n,:)
            for y = ymin(n,:):1:ymax(n,:)
                pixRGB_new(n,:) = impixel(im,x,y);
                if pixRGB_new(n,:) > pixRGB(n)
                    %records the coordinates of the lightest coloured
                    %pixel in the subset
                    coords(n,:) = [x y];
                    pixRGB(n,:)=pixRGB_new(n);
                end
            end
        end
    else
        pixRGB(n,1:3) = 5555;
        pixRGB_new(n,1:3) = 5555;
        coords(n,1:2) = 5555;
    end
end

%calculates horizontal distance(pix) between holes and pixel size (mm/pix)
n=1;
pix_horiz_counter=0;
pix_size_horiz_total=0;

```

```

while n<counter & n<25
    if isequal(n,5)lisequal(n,10)lisequal(n,15)lisequal(n,20)
        pix_size_horiz(n,1) = 5555;

    elseif (points(n,:)==5555) |(points(n+1,:)==5555)
        pix_size_horiz(n,1) = 5555;

    else
        x_dist=coords(n,1)-coords(n+1,1);
        y_dist=coords(n,2)-coords(n+1,2);
        dist_horiz(n,:)=((x_dist^2)+(y_dist^2))^0.5;
        pix_size_horiz(n,:)=known_d/dist_horiz(n,:);

        pix_size_horiz_total = pix_size_horiz(n,1) + pix_size_horiz_total;
        pix_horiz_counter = pix_horiz_counter + 1;
    end
    n=n+1;
end
%average horizontal pixel size (mm/pix)
avg_pix_size_horiz = pix_size_horiz_total/pix_horiz_counter;

%calculates vertical distance(pix) between holes and pixel size (mm/pix)
n=1;
pix_vert_counter=0;
pix_size_vert_total = 0;
while n<counter-4 & n<21
    if (points(n,:)==5555) |(points(n+5,:)==5555)
        pix_size_vert(n,1)=5555;

    else
        x_dist=coords(n,1)-coords(n+5,1);
        y_dist=coords(n,2)-coords(n+5,2);
        dist_vert(n,:)=((x_dist^2)+(y_dist^2))^0.5;
        pix_size_vert(n,:)=known_d/dist_vert(n,:);

        pix_size_vert_total = pix_size_vert(n,1) + pix_size_vert_total;
        pix_vert_counter = pix_vert_counter + 1;
    end
    n=n+1;
end
%average vertical pixel size
avg_pix_size_vert = pix_size_vert_total/pix_vert_counter;

%average pixel size
avg_pix_size = (avg_pix_size_horiz + avg_pix_size_vert)/2;
end

```


A.3 PIXEL NUMBER GUIDE

Digitize the holes closes to the image intensifier centre (the circled numbers).

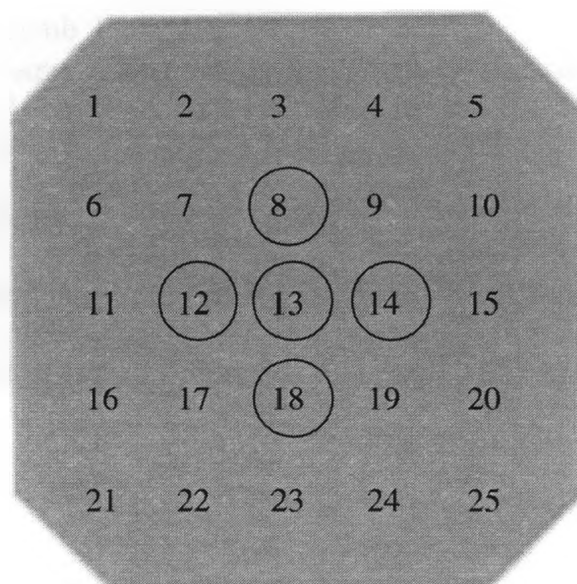


Figure A.2: Pixel number guide

APPENDIX B – SYMBOLIC EQUATIONS FOR CALIBRATION ALGORITHM CREATED IN MAPLE

>Program Name: Calib_Symb_Eq.mw

- Creates symbolic equations necessary for calibration procedure

Created by: Anne-Marie Allen

Date Created: Nov 19, 2008

Date Last Modified: Feb 16, 2009

> with(LinearAlgebra) :

> restart;

> P matrix relates 3D points in the projection coordinate system with their 2D image points

> P:=Matrix([[cs/d,1/sp,0] , [ls/d,0,1/sp] , [1/d,0,0]]) ;

$$P := \begin{bmatrix} \frac{cs}{d} & \frac{1}{sp} & 0 \\ \frac{ls}{d} & 0 & \frac{1}{sp} \\ \frac{1}{d} & 0 & 0 \end{bmatrix}$$

**> ROTz:=Matrix([[cos(theta),-sin(theta),0] ,
[sin(theta),cos(theta),0] , [0,0,1]]) ;**

$$ROTz := \begin{bmatrix} \cos(\theta) & -\sin(\theta) & 0 \\ \sin(\theta) & \cos(\theta) & 0 \\ 0 & 0 & 1 \end{bmatrix}$$

**> ROTy:=Matrix([[cos(Phi),0,sin(Phi)] , [0,1,0] ,
[-sin(Phi),0,cos(Phi)]]) ;**

$$ROTy := \begin{bmatrix} \cos(\Phi) & 0 & \sin(\Phi) \\ 0 & 1 & 0 \\ -\sin(\Phi) & 0 & \cos(\Phi) \end{bmatrix}$$

**> ROTx:=Matrix([[1,0,0] , [0,cos(psi),-sin(psi)] ,
[0,sin(psi),cos(psi)]]) ;**

$$ROTx := \begin{bmatrix} 1 & 0 & 0 \\ 0 & \cos(\psi) & -\sin(\psi) \\ 0 & \sin(\psi) & \cos(\psi) \end{bmatrix}$$

> Z-Y-X Euler angle rotation sequence (R matrix) is associated with the change in axes from \mathcal{R} to \mathcal{R}'

> $\mathbf{R} := \mathbf{ROTz} . \mathbf{ROTy} . \mathbf{ROTx}$;

$$R := \begin{bmatrix} \cos(\theta) \cos(\Phi) & -\sin(\theta) \cos(\psi) + \cos(\theta) \sin(\Phi) \sin(\psi) & \sin(\theta) \sin(\psi) + \cos(\theta) \sin(\Phi) \cos(\psi) \\ \sin(\theta) \cos(\Phi) & \cos(\theta) \cos(\psi) + \sin(\theta) \sin(\Phi) \sin(\psi) & -\cos(\theta) \sin(\psi) + \sin(\theta) \sin(\Phi) \cos(\psi) \\ -\sin(\Phi) & \cos(\Phi) \sin(\psi) & \cos(\Phi) \cos(\psi) \end{bmatrix}$$

> Translation matrix

> $\mathbf{T} := \mathbf{Matrix}([[1, 0, 0, -xs], [0, 1, 0, -ys], [0, 0, 1, -zs]])$;

$$T := \begin{bmatrix} 1 & 0 & 0 & -xs \\ 0 & 1 & 0 & -ys \\ 0 & 0 & 1 & -zs \end{bmatrix}$$

> $\mathbf{M} := \mathbf{P} . \mathbf{R} . \mathbf{T}$;

$$M := \begin{bmatrix} \left[\frac{cs \cos(\theta) \cos(\Phi)}{d} + \frac{\sin(\theta) \cos(\Phi)}{sp}, \right. \\ \frac{cs (-\sin(\theta) \cos(\psi) + \cos(\theta) \sin(\Phi) \sin(\psi))}{d} + \frac{\cos(\theta) \cos(\psi) + \sin(\theta) \sin(\Phi) \sin(\psi)}{sp}, \\ \frac{cs (\sin(\theta) \sin(\psi) + \cos(\theta) \sin(\Phi) \cos(\psi))}{d} + \frac{-\cos(\theta) \sin(\psi) + \sin(\theta) \sin(\Phi) \cos(\psi)}{sp}, \\ \left. - \left(\frac{cs \cos(\theta) \cos(\Phi)}{d} + \frac{\sin(\theta) \cos(\Phi)}{sp} \right) xs \right. \\ - \left(\frac{cs (-\sin(\theta) \cos(\psi) + \cos(\theta) \sin(\Phi) \sin(\psi))}{d} + \frac{\cos(\theta) \cos(\psi) + \sin(\theta) \sin(\Phi) \sin(\psi)}{sp} \right) ys \\ \left. - \left(\frac{cs (\sin(\theta) \sin(\psi) + \cos(\theta) \sin(\Phi) \cos(\psi))}{d} + \frac{-\cos(\theta) \sin(\psi) + \sin(\theta) \sin(\Phi) \cos(\psi)}{sp} \right) zs \right] , \left[\right. \\ \frac{ls \cos(\theta) \cos(\Phi)}{d} - \frac{\sin(\Phi)}{sp}, \frac{ls (-\sin(\theta) \cos(\psi) + \cos(\theta) \sin(\Phi) \sin(\psi))}{d} + \frac{\cos(\Phi) \sin(\psi)}{sp}, \\ \frac{ls (\sin(\theta) \sin(\psi) + \cos(\theta) \sin(\Phi) \cos(\psi))}{d} + \frac{\cos(\Phi) \cos(\psi)}{sp}, \left. - \left(\frac{ls \cos(\theta) \cos(\Phi)}{d} - \frac{\sin(\Phi)}{sp} \right) xs \right. \\ \left. - \left(\frac{ls (-\sin(\theta) \cos(\psi) + \cos(\theta) \sin(\Phi) \sin(\psi))}{d} + \frac{\cos(\Phi) \sin(\psi)}{sp} \right) ys \right] \end{bmatrix}$$

$$\begin{aligned}
& - \left(\frac{ls (\sin(\theta) \sin(\psi) + \cos(\theta) \sin(\Phi) \cos(\psi))}{d} + \frac{\cos(\Phi) \cos(\psi)}{sp} \right) zs \Bigg] \cdot \left[\frac{\cos(\theta) \cos(\Phi)}{d}, \right. \\
& \frac{-\sin(\theta) \cos(\psi) + \cos(\theta) \sin(\Phi) \sin(\psi)}{d}, \frac{\sin(\theta) \sin(\psi) + \cos(\theta) \sin(\Phi) \cos(\psi)}{d}, \\
& \left. - \frac{\cos(\theta) \cos(\Phi) xs}{d} - \frac{(-\sin(\theta) \cos(\psi) + \cos(\theta) \sin(\Phi) \sin(\psi)) ys}{d} - \frac{(\sin(\theta) \sin(\psi) + \cos(\theta) \sin(\Phi) \cos(\psi)) zs}{d} \right] \\
& \Bigg]
\end{aligned}$$

> c coordinate of image point written in terms of calibration parameters

```
>fcp:=(M[1,1]*x+M[1,2]*y+M[1,3]*z+M[1,4])/
(M[3,1]*x+M[3,2]*y+M[3,3]*z+M[3,4]);
```

$$\begin{aligned}
cp = & \left(\left(\frac{cs \cos(\theta) \cos(\Phi)}{d} + \frac{\sin(\theta) \cos(\Phi)}{sp} \right) x \right. \\
& + \left(\frac{cs (-\sin(\theta) \cos(\psi) + \cos(\theta) \sin(\Phi) \sin(\psi))}{d} + \frac{\cos(\theta) \cos(\psi) + \sin(\theta) \sin(\Phi) \sin(\psi)}{sp} \right) y \\
& + \left(\frac{cs (\sin(\theta) \sin(\psi) + \cos(\theta) \sin(\Phi) \cos(\psi))}{d} + \frac{-\cos(\theta) \sin(\psi) + \sin(\theta) \sin(\Phi) \cos(\psi)}{sp} \right) z \\
& - \left(\frac{cs \cos(\theta) \cos(\Phi)}{d} + \frac{\sin(\theta) \cos(\Phi)}{sp} \right) xs \\
& - \left(\frac{cs (-\sin(\theta) \cos(\psi) + \cos(\theta) \sin(\Phi) \sin(\psi))}{d} + \frac{\cos(\theta) \cos(\psi) + \sin(\theta) \sin(\Phi) \sin(\psi)}{sp} \right) ys \\
& \left. - \left(\frac{cs (\sin(\theta) \sin(\psi) + \cos(\theta) \sin(\Phi) \cos(\psi))}{d} + \frac{-\cos(\theta) \sin(\psi) + \sin(\theta) \sin(\Phi) \cos(\psi)}{sp} \right) zs \right) \Bigg/ \left(\right. \\
& \frac{\cos(\theta) \cos(\Phi) x}{d} + \frac{(-\sin(\theta) \cos(\psi) + \cos(\theta) \sin(\Phi) \sin(\psi)) y}{d} + \frac{(\sin(\theta) \sin(\psi) + \cos(\theta) \sin(\Phi) \cos(\psi)) z}{d} \\
& \left. - \frac{\cos(\theta) \cos(\Phi) xs}{d} - \frac{(-\sin(\theta) \cos(\psi) + \cos(\theta) \sin(\Phi) \sin(\psi)) ys}{d} - \frac{(\sin(\theta) \sin(\psi) + \cos(\theta) \sin(\Phi) \cos(\psi)) zs}{d} \right)
\end{aligned}$$

> l coordinate of image point written in terms of calibration parameters

```
>flp:=(M[2,1]*x+M[2,2]*y+M[2,3]*z+M[2,4])/
(M[3,1]*x+M[3,2]*y+M[3,3]*z+M[3,4]);
```

$$\begin{aligned}
lp = & \left(\left(\frac{ls \cos(\theta) \cos(\Phi)}{d} - \frac{\sin(\Phi)}{sp} \right) x + \left(\frac{ls (-\sin(\theta) \cos(\psi) + \cos(\theta) \sin(\Phi) \sin(\psi))}{d} + \frac{\cos(\Phi) \sin(\psi)}{sp} \right) y \right. \\
& + \left(\frac{ls (\sin(\theta) \sin(\psi) + \cos(\theta) \sin(\Phi) \cos(\psi))}{d} + \frac{\cos(\Phi) \cos(\psi)}{sp} \right) z - \left(\frac{ls \cos(\theta) \cos(\Phi)}{d} - \frac{\sin(\Phi)}{sp} \right) xs \\
& - \left(\frac{ls (-\sin(\theta) \cos(\psi) + \cos(\theta) \sin(\Phi) \sin(\psi))}{d} + \frac{\cos(\Phi) \sin(\psi)}{sp} \right) ys \\
& \left. - \left(\frac{ls (\sin(\theta) \sin(\psi) + \cos(\theta) \sin(\Phi) \cos(\psi))}{d} + \frac{\cos(\Phi) \cos(\psi)}{sp} \right) zs \right) \Bigg/ \left(\frac{\cos(\theta) \cos(\Phi) x}{d} \right. \\
& + \frac{(-\sin(\theta) \cos(\psi) + \cos(\theta) \sin(\Phi) \sin(\psi)) y}{d} + \frac{(\sin(\theta) \sin(\psi) + \cos(\theta) \sin(\Phi) \cos(\psi)) z}{d} - \frac{\cos(\theta) \cos(\Phi) xs}{d} \\
& \left. - \frac{(-\sin(\theta) \cos(\psi) + \cos(\theta) \sin(\Phi) \sin(\psi)) ys}{d} - \frac{(\sin(\theta) \sin(\psi) + \cos(\theta) \sin(\Phi) \cos(\psi)) zs}{d} \right)
\end{aligned}$$

APPENDIX C – MATLAB CODE AND INSTRUCTIONS FOR ESTIMATION OF CALIBRATION PARAMETERS

C.1 INSTRUCTIONS

1. Run Angela Kedgley's digitization and RSA code (Kedgley, 2009a) to determine:
 - 2D distortion point coordinates
 - 2D distortion-corrected calibration point coordinates
 - x-ray source coordinates
2. Derive the calibration equations based on the orientation of the fluoroscope and calibration frame (Section 2.2).
3. Create the symbolic calibration equations (Appendix B)
4. Copy the symbolic equations for "cp" and "lp" from Maple and paste them into the "Proj_Points_Calc.m" MATLAB Code
5. Run "Calibration_Points.m" to create an excel spreadsheet with the 3D coordinates of calibration points and their corresponding distortion-corrected 2D points. You might need to multiply the C or L coordinates of the 2D points by -1 so that C and L axis are in the same direction as 2 axes of the projection coordinate system (see Figure 2.6). Distortion corrected point coordinates are expressed in the following coordinate system.

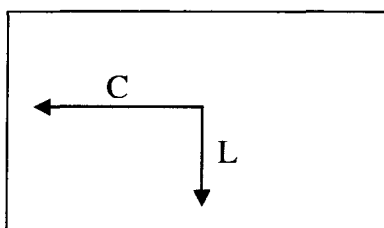


Figure C.1: Coordinate system for distortion-corrected points

6. Run "Starting_Parameters.m" to generate initial estimates of the calibration parameters
7. Run "Optimization_Main.m" to generate final estimates of the calibration parameters.

C.2 “CALIBRATION_POINTS.M”

```

%Program: Calibration Points
%Description: Creates an excel spreadsheet with the fiducial and
%control points 3D coordinates and their corresponding 2D projection
%coordinates
%Date Created: Feb 17, 2009
%Written by: Anne-Marie Allen

% Obtain the name of the file containing the fiducial points
fid_file = input('Enter the name of the file containing the distortion corrected fiducial
points : ','s');
fid_filename = strcat(fid_file, '.xls');

% Obtain the name of the file containing the control points
con_file = input('Enter the name of the file containing the distortion corrected control
points : ','s');
con_filename = strcat(con_file, '.xls');

% Obtain the name of the file with the 3D positions of the points on the calibration frame
Frame_points_file= input('Enter the name of the file containing the 3D calibration frame
points : ','s');
Frame_points_filename = strcat(Frame_points_file, '.xls');

% Obtain if F1/C1 planes or F2/C2 planes should be used
FC_planes=input('Input 1 for F1/C1 and input 2 for F2/C2 : ');

% Obtain if FluoroA or FluoroB pixel size should be used
Fluoro_type=input('Input A for FluoroA and input B for FluoroB :','s');

if Fluoro_type=='A'
    sp = 0.38471030965223; % FluoroA pixel size
elseif Fluoro_type=='B'
    sp = 0.3819051976636; %FluoroB pixel size
end

data_dir = ['.....\'];

Frame_points_dir = [.....\];

% 3D Coordinates of fiducial and control points
if FC_planes==1
    fid_pts_3D=xlsread([Frame_points_dir,Frame_points_filename],1);
    con_pts_3D=xlsread([Frame_points_dir,Frame_points_filename],3);
else

```

```

    fid_pts_3D=xlsread([Frame_points_dir,Frame_points_filename],2);
    con_pts_3D=xlsread([Frame_points_dir,Frame_points_filename],4);
end

% 2D fiducial and control points
fid_pts_2D = xlsread([data_dir,fid_filename]);
con_pts_2D = xlsread([data_dir,con_filename]);

%Build a matrix with 3D point and 2D projections (fid_con_pts)
%Column 1 = x coordinate of 3D fiducial/control point (mm)
%Column 2 = y coordinate of 3D fiducial/control point (mm)
%Column 3 = z coordinate of 3D fiducial/control point (mm)
%Column 4 = c coordinate of projection of 3D fiducial/control %point(pix)
%Column 5 = l coordinate of projection of 3D fiducial/control %point(pix)

n=1;
for i=1:1:45
    if fid_pts_2D(i,:)~=5555
        fid_con_pts(n,1)=fid_pts_3D(i,1);
        fid_con_pts(n,2)=fid_pts_3D(i,2);
        fid_con_pts(n,3)=fid_pts_3D(i,3);
        fid_con_pts(n,4)=fid_pts_2D(i,2)/sp;
        fid_con_pts(n,5)=fid_pts_2D(i,3)/sp;
        n=n+1;
    end
end

for i=1:1:45
    if con_pts_2D(i,:)~=5555
        fid_con_pts(n,1)=con_pts_3D(i,1);
        fid_con_pts(n,2)=con_pts_3D(i,2);
        fid_con_pts(n,3)=con_pts_3D(i,3);
        fid_con_pts(n,4)=con_pts_2D(i,2)/sp;
        fid_con_pts(n,5)=con_pts_2D(i,3)/sp;
        n=n+1;
    end
end

%Output 3D and 2D projections of fiducial and control points
output_filename = strcat('Fluoro',Fluoro_type,'-CalibrationPoints');
output_write = fullfile(data_dir, output_filename);
xlswrite(output_write, fid_con_pts);

```


C.3 “PROJ_POINTS_CALC.M”

%Program Name: Proj_Points_Calc

%Description: Calculates 2D coordinates of projected calibration points

%(cp,lp) using estimates of calibration parameters

%created by: Anne-Marie Allen

%Date created: Jan 8, 2009

%Date modified: March 19, 2009

function[cp,lp] = proj_points_calc(xs,ys,zs,sp,theta,phi,psi,d,cs,ls,x,y,z,i)

% c coordinate of projected calibration point, as calculated

% from estimated parameters

cp=((cs*cos(theta)*cos(phi)/d+sin(theta)*cos(phi)/sp)*x+(cs*(-
sin(theta)*cos(psi)+cos(theta)*sin(phi)*sin(psi))/d+(cos(theta)*cos(psi)+sin(theta)*sin(psi)*sin(phi)*sin(psi))/sp)*y+(cs*(sin(theta)*sin(psi)+cos(theta)*sin(phi)*cos(psi))/d+(-
cos(theta)*sin(psi)+sin(theta)*sin(phi)*cos(psi))/sp)*z-
(cs*cos(theta)*cos(phi)/d+sin(theta)*cos(phi)/sp)*xs-(cs*(-
sin(theta)*cos(psi)+cos(theta)*sin(phi)*sin(psi))/d+(cos(theta)*cos(psi)+sin(theta)*sin(psi)*sin(phi)*sin(psi))/sp)*ys-(cs*(sin(theta)*sin(psi)+cos(theta)*sin(phi)*cos(psi))/d+(-
cos(theta)*sin(psi)+sin(theta)*sin(phi)*cos(psi))/sp)*zs)/(cos(theta)*cos(phi)*x/d+(-
sin(theta)*cos(psi)+cos(theta)*sin(phi)*sin(psi))*y/d+(sin(theta)*sin(psi)+cos(theta)*sin(phi)*cos(psi))*z/d-cos(theta)*cos(phi)*xs/d-(-
sin(theta)*cos(psi)+cos(theta)*sin(phi)*sin(psi))*ys/d-
(sin(theta)*sin(psi)+cos(theta)*sin(phi)*cos(psi))*zs/d);

% l coordinate of projected calibration point, as calculated

% from estimated parameters

lp=((ls*cos(theta)*cos(phi)/d-sin(phi)/sp)*x+(ls*(-
sin(theta)*cos(psi)+cos(theta)*sin(phi)*sin(psi))/d+cos(phi)*sin(psi)/sp)*y+(ls*(sin(theta)*sin(psi)+cos(theta)*sin(phi)*cos(psi))/d+cos(phi)*cos(psi)/sp)*z-
(ls*cos(theta)*cos(phi)/d-sin(phi)/sp)*xs-(ls*(-
sin(theta)*cos(psi)+cos(theta)*sin(phi)*sin(psi))/d+cos(phi)*sin(psi)/sp)*ys-
(ls*(sin(theta)*sin(psi)+cos(theta)*sin(phi)*cos(psi))/d+cos(phi)*cos(psi)/sp)*zs)/(cos(theta)*cos(phi)*x/d+(-
sin(theta)*cos(psi)+cos(theta)*sin(phi)*sin(psi))*y/d+(sin(theta)*sin(psi)+cos(theta)*sin(phi)*cos(psi))*z/d-cos(theta)*cos(phi)*xs/d-(-
sin(theta)*cos(psi)+cos(theta)*sin(phi)*sin(psi))*ys/d-
(sin(theta)*sin(psi)+cos(theta)*sin(phi)*cos(psi))*zs/d);

C.4 “STARTING_PARAMETERS.M”

```
%Program Name: Starting_Parameters
%Description: Determines initial starting parameters before
%optimization routine is employed
%created by: Anne-Marie Allen
%Date created: Jan 8, 2009
%Date modified: March 19, 2009

%P Matrix
cs = 0; %initial estimate of image coord. of source projection
ls = 0; %initial estimate of image coord. of source projection

d=1000; %initial estimate of source to projected source distance

%R Matrix
% Euler Angles (zyx) Associated with the change from R to R'
theta=0; %rot abt vertical z axis
phi=0; %rot abt y (inclination)
psi=0; %rot abt x (rot in the image plane)

sum_E=0;
i = 0;
E_min=100;
par(1:3,1:6) = zeros(3,6);

data_dir = ['.....\'];

% Obtain the location of the file containing the fiducial and control
% points (o/p of “Calibration Points.m”)
points_file = input('Enter the name of the file which contains the fiducial and control
points (o/p of “Calibration Points.m”): ','s');
points_filename = strcat(points_file, '.xls');
points = xlsread([data_dir,points_filename],1);

% Obtain the location of the fluoro focus
focus_file = input('Enter the name of the file which contains fluoro focus: ','s');
focus_filename = strcat(focus_file, '.xls');
focus = xlsread([data_dir,focus_filename],1);

%T Matrix
xs = focus(1,1); %source coord. (x) in R/lab frame
ys = focus(2,1); %source coord. (y) in R/lab frame
zs = focus(3,1); %source coord. (z) in R/lab frame
```

```

% Obtain if FluoroA or FluoroB pixel size should be used
Fluoro_type=input('Input A for FluoroA and input B for FluoroB : ','s');

if Fluoro_type=='A'
    sp = 0.38471030965223; % FluoroA pixel size
elseif Fluoro_type=='B'
    sp = 0.3819051976636; %FluoroB pixel size
end

Points_size=size(points);

x=points(:,1); %x coordinate of calibration point
y=points(:,2); %y coordinate of calibration point
z=points(:,3); %z coordinate of calibration point
c=points(:,4); % c coordinate of projected calibration point, as measured
l=points(:,5); % l coordinate of projected calibration point, as measured

%First Iteration
%Angles iterate from -pi to pi in increments of pi/16
for theta=(-pi:pi/16:pi)
    for phi=(-pi:pi/16:pi)
        for psi=(-pi:pi/16:pi)
            for i=1:Points_size(1,1)

                % c and l coordinate of projected calibration point, as
                % calculated from estimated parameters
                [cp,lp] =
                Proj_Points_Calc(xs,ys,zs,sp,p(1),p(2),p(3),p(4),p(5),p(6),x(i,1),y(i,1),z(i,1),i);
                %temporary error calculation
                E_temp=(cp-c(i,1))^2+(lp-l(i,1))^2;
                sum_E = sum_E + E_temp;
                E_temp=0;

            end

            if ((sqrt(sum_E/Points_size(1,1)))*sp) < E_min
                % Root mean squared error in mm
                E_min=(sqrt(sum_E/Points_size(1,1)))*sp;
                par(1,1:6)=[theta,phi,psi,d,cs,ls];
            end

            sum_E=0;

        end
    end
end
end
end

```

```

if par(1,4) == 0
    par(1,1:6)=[0,0,0,d,cs,ls];
end

%Second iteration
%Angles iterate from value resulting min error - pi/16 to value resulting in
%min error + pi/16 in increments of pi/128
for theta=(par(1,1)-pi/16:pi/128:par(1,1)+pi/16)
    for phi=(par(1,2)-pi/16:pi/128:par(1,2)+pi/16)
        for psi=(par(1,3)-pi/16:pi/128:par(1,3)+pi/16)
            for i=1:Points_size(1,1)

                % c and l coordinate of projected calibration point, as
                % calculated from estimated parameters
                [cp,lp] =
                Proj_Points_Calc(xs,ys,zs,sp,p(1),p(2),p(3),p(4),p(5),p(6),x(i,1),y(i,1),z(i,1),i);
                %temporary error calculation
                E_temp=(cp-c(i,1))^2+(lp-l(i,1))^2;
                sum_E = sum_E + E_temp;

            end

            if ((sqrt(sum_E/Points_size(1,1)))*sp) < E_min
                % Root mean squared error in mm
                E_min=(sqrt(sum_E/Points_size(1,1)))*sp;
                par(2,1:6)=[theta,phi,psi,d,cs,ls];
            end
            sum_E=0;
        end
    end
end

if par(2,4) == 0
    par(2,1:6)=par(1,1:6);
end

%Third iteration
%Angles range from value resulting in min error - pi/128 to value resulting in
%min error + pi/128 in increments of pi/1024
for theta=(par(2,1)-pi/128:pi/1024:par(2,1)+pi/128)
    for phi=(par(2,2)-pi/128:pi/1024:par(2,2)+pi/128)
        for psi=(par(2,3)-pi/128:pi/1024:par(2,3)+pi/128)
            for i=1:Points_size(1,1)

```

```

        % c and l coordinate of projected calibration point, as
        calculated from estimated parameters
        [cp,lp] =
        Proj_Points_Calc(xs,ys,zs,sp,p(1),p(2),p(3),p(4),p(5),p(6),x(i,1),y(i,1),z(i,1),i);
        %temporary error calculation
        E_temp=(cp-c(i,1))^2+(lp-l(i,1))^2;
        sum_E = sum_E + E_temp;

    end

    if ((sqrt(sum_E/Points_size(1,1)))*sp) < E_min
        % Root mean squared error in mm
        E_min=(sqrt(sum_E/Points_size(1,1)))*sp;
        par(3,1:6)=[theta,phi,psi,d,cs,ls];
    end
    sum_E=0;
end
end
end

if par(3,4) == 0
    par(3,1:6)=par(2,1:6);
end

% write estimated starting parameters to an excel spreadsheet
starting_par_filename = strcat('Fluoro',Fluoro_type,'_starting par');
xlswrite([data_dir,starting_par_filename],par);

```

C.5 “OPTIMIZATION_MAIN.M”

```
%Program:Optimization_main
%Description: Estimates the calibration parameters (theta, phi, psi, d, cs,ls) by using
'fmincon'
    %objective function = 'objfun.m'
    %constraint function = 'confun.m'
%Date Created: Feb 15, 2009
%Written by:Anne-Marie Allen

% Calibration Parameters (p)
% theta = p(1), rotation about the z axis (rads)
% phi = p(2), image plane tilt (y axis) (rads)
% psi = p(3), rotation in the image plane (x axis) (rads)
% d = p(4), distance from the image plane to the source (mm)
% cs = p(5), x coord of the projected source on the image plane (pix)
% ls = p(6), y coord of the projected source on the image plane (pix)

data_dir = ['C.....\'];

%Obtain the name of the file containing the 3D and 2D projected %fiducial and
calibration points (o/p of Calibration_Points.m)
points_file = input('Enter the name of the file containing the 3D and 2D projected fiducial
and calibration points (o/p of Calibration_Points.m) : ','s');
points_filename = strcat(points_file, '.xls');
points = xlsread([data_dir,points_filename]);

% Obtain the name of the file containing the starting parameters
starting_par_file = input('Enter the name of the file containing starting parameters : ','s');
starting_par_filename = strcat(starting_par_file, '.xls');
starting_par = xlsread([data_dir,starting_par_filename]);

% Obtain the location of the fluoro focus
focus_file = input('Enter the name of the file which contains fluoro focus: ','s');
focus_filename = strcat(focus_file, '.xls');
focus = xlsread([data_dir,focus_filename],1);

% xs = focus(1,1); %source coord. (xs)
% ys = focus(2,1); %source coord. (ys)
% zs = focus(3,1); %source coord. (zs)

% Obtain if FluoroA or FluoroB pixel size should be used
Fluoro_type=input('Input A for FluoroA and input B for FluoroB : ','s');

if Fluoro_type=='A'
```

```

    sp = 0.38471030965223; % FluoroA pixel size
elseif Fluoro_type=='B'
    sp = 0.3819051976636; %FluoroB pixel size
end

%Input for objective function
%input(:,1) = x coordinate of 3D fiducial/control point (mm)
%input(:,2) = y coordinate of 3D fiducial/control point (mm)
%input(:,3) = z coordinate of 3D fiducial/control point (mm)
%input(:,4) = c coordinate of projection of 3D fiducial/control point(pix)
%input(:,5) = l coordinate of projection of 3D fiducial/control point(pix)
input(:,1:5) = points(:,1:5);

input(1,6) = focus(1,1); %source coord. (xs)
input(1,7) = focus(2,1); %source coord. (ys)
input(1,8) = focus(3,1); %source coord. (zs)
input(1,9) = sp; % pixel size

%starting estimates
p0=[starting_par(3,1),starting_par(3,2),starting_par(3,3),starting_par(3,4),starting_par(3,
5),starting_par(3,6)];

%lower bounds
lb=[-5 -5 -5 900 -2 -2];

%upper bounds
ub=[5 5 5 1100 2 2];

options = optimset('LargeScale', 'off','MaxFunEvals',1000);

% 'fmincon' function used to estimate calibration parameters
[p,Eval,exitflag,output]=fmincon('objfun',p0,[],[],[],[],lb,ub,'confun',options,input);

output_write = fullfile(data_dir, 'FluoroB-parameters');
xlswrite(output_write, p);

output_write = fullfile(data_dir, 'FluoroB-Error');
xlswrite(output_write, Eval);

```

C.6 “OBJFUN.M”

%Program:Objfun

%Description: Objective function for the “optimization_main” routine

%Date Created: Feb 15, 2009

%Written by: Anne-Marie Allen

function E = objfun(p,input)

% Calibration Parameters

% theta = p(1), rotation about the z axis

% phi = p(2), image plane tilt (y axis)

% psi = p(3), rotation in the image plane (x axis)

% d = p(4), distance from the image plane to the source (mm)

% cs = p(5), x coord of the projected source on the image plane (pix)

% ls = p(6), y coord of the projected source on the image plane (pix)

%Input for objective function

x = input(:,1); %x coordinate of 3D fiducial/control point (mm)

y = input(:,2); %y coordinate of 3D fiducial/control point (mm)

z = input(:,3); %z coordinate of 3D fiducial/control point (mm)

c = input(:,4); %c coordinate of projection of 3D fiducial/control point(pix)

l = input(:,5); %l coordinate of projection of 3D fiducial/control point(pix)

xs = input(1,6); %x source coord. (mm)

ys = input(1,7); %y source coord. (mm)

zs = input(1,8); %z source coord. (mm)

sp = input(1,9); %pixel size (mm/pix)

sum_E=0;

E=0;

i = 0;

input_size=size(input(:,1));

for i=1:input_size(1,1)

 % c and l coordinate of projected calibration point, as

 % calculated from estimated parameters

 [cp,lp] = Proj_Points_Calc(xs,ys,zs,sp,p(1),p(2),p(3),p(4),p(5),p(6),x(i,1),y(i,1),z(i,1),i);

 %temporary error calculation

 E_temp=(cp-c(i,1))^2+(lp-l(i,1))^2;

 sum_E = sum_E + E_temp;

 E_temp = 0;

end


```
E=(sqrt(sum_E/input_size(1,1)))*sp; % root mean square error (mm)
```

C.7 “CONFUN.M”

```
%Program: Confun
```

```
%Description: Constraint function for the “optimization_main” routine
```

```
%N.B. 'fmincon' must have a constraint function
```

```
%Date Created: Feb 15, 2009
```

```
%Written by: Anne-Marie Allen
```

```
function[c,ceq]=confun(p,points)
```

```
c=[-p(4)+995; p(4)-1005; -p(5)-2; p(5)-2; -p(6)-2; p(6)-2];
```

```
ceq=[];
```

APPENDIX D – CODE FOR IMAGE PLANE CORRECTION

D.1 “DISTGRID_ROTTRANS.M”

```
%Program:DistGrid_RotTrans
%Description:
% - Calculates centre of the distortion grid wrt the bottom left hand
% corner of the image
% - Calculates the rotation angle of the distortion grid wrt to the
% horizontal axis of the image
%Date Created: October 12, 2009
%Written by: Anne-Marie Allen

% Obtain the name of the file of the digitized distortion grid points
Dist_points_file= input('Enter the name of the file containing the digitized distortion grid
points : ','s');
Dist_points_filename = strcat(Dist_points_file, '.xls');

data_dir = ['C.....\'];

% Obtain if FluoroA or FluoroB pixel size should be used
Fluoro_type=input('Input A for FluoroA and input B for FluoroB : ','s');

if Fluoro_type=='A'
    sp = 0.38471030965223; % FluoroA pixel size
elseif Fluoro_type=='B'
    sp = 0.3819051976636; %FluoroB pixel size
end

% 2D fiducial and control points
dist_pts = xlsread([data_dir,Dist_points_filename]);

% Distortion grid centre wrt bottom left hand corner of the image (mm)
origin_x = (dist_pts(70,2))*sp
origin_y = (dist_pts(70,3))*sp

% Rotation of the distortion grid about the distortion grid centre m =
polyfit(dist_pts(65:75,2),dist_pts(65:75,3),1);
angle_rad = atan2(m(1,1),1)
angle_deg = angle_rad*(180/pi)
```

D.2 “IMPORTPOINTS.RVB”

'Program: ImportPoints

'Description: Imports 2D Points from an Excel spreadsheet onto the image plane using
'the distortion grid coordinate system (CPlane)

'Sheet 1 = fiducial points

'Sheet 2 = control points

'Date Created: July 14, 2009

'Date Modified: Oct 13, 2009

'Created by: Anne-Marie Allen

Call ImportPoints

Sub ImportPoints()

Dim sFileName, arrFPoints(45), arrCPoints(45), arrWorldFPoints(), arrWorldCPoints()

Dim oExcel, oSheet1, oSheet2, nRow, nRowCount, ncounterF, ncounterC

' User selects the file with the distortion corrected 2D calibration frame points (sheet1 =
fiducial; sheet 2 = control)

sFileName = Rhino.OpenFileName("Select File with the distortion corrected 2D
calibration points (sheet1=fid;sheet2=con)","Excel Files (*.xls)|*.xls|")

If IsNull(sFileName) Then Exit Sub

' Launch Excel and open the specified file

Set oExcel = CreateObject("Excel.Application")

oExcel.Workbooks.Open(sFileName)

' Get the first and second worksheet

Set oSheet1 = oExcel.ActiveWorkbook.Worksheets(1)

Set oSheet2 = oExcel.ActiveWorkbook.Worksheets(2)

' Import the fiducial points

Rhino.Print "Importing fiducial points"

ncounterF = 0

For nRow = 1 To 45

 Fx = oSheet1.Cells(nRow, 2).Value

 Fy = oSheet1.Cells(nRow, 3).Value

 Fz = 0

 If (Fx <> 5555) Then

 ncounterF = 1 + ncounterF

 arrFPoints(ncounterF) = Array(Fx,Fy,Fz)

```

        Rhino.Print Rhino.Pt2Str(arrFPoints(ncounterF))
    End If
Next

'Import the control points
Rhino.Print "Importing control points"
ncounterC = 0
For nRow = 1 To 45
    Cx = oSheet2.Cells(nRow, 2).Value
    Cy = oSheet2.Cells(nRow, 3).Value
    Cz = 0
    If (Cx <> 5555) Then
        ncounterC = 1 + ncounterC
        arrCPoints(ncounterC) = Array(Cx,Cy,Cz)
        Rhino.Print Rhino.Pt2Str(arrCPoints(ncounterC))
    End If
Next

'Quits excel
oExcel.Quit

Set oSheet = Nothing
Set oExcel = Nothing

'User enters the name of the Construction Plane which defines distortion grid coordinate
system
Dim arrCPlane
strCPlane = Rhino.GetString("Type in the name of the Construction Plane (CPlane)
which defines distortion grid coordinate system")
arrCPlane = Rhino.NamedCPlane(strCPlane)
If Not IsArray(arrCPlane) Then
    Rhino.Print "Invalid CPlane entered. Please run code again."
    Exit Sub
End If

'Transforms fiducial points from distortion grid coordinate system to lab coordinate
system
If (UBound(arrFPoints) > 0) Then
    ReDim arrWorldFPoints(UBound(arrFPoints))
    For i = 1 To ncounterF
        arrWorldFPoints(i)=Rhino.XFormCPlaneToWorld(arrFPoints(i),
arrCPlane)
        Rhino.AddPoint arrWorldFPoints(i)
    Next
End If

```

'Transforms control points from distortion grid coordinate system to lab coordinate system

If (UBound(arrCPoints) > 0) Then

ReDim arrWorldCPoints(UBound(arrCPoints))

For i = 1 To ncounterC

arrWorldCPoints(i)=Rhino.XFormCPlaneToWorld(arrCPoints(i),
arrCPlane)

Rhino.AddPoint arrWorldCPoints(i)

Next

End If

End Sub

D.3 “PROJECTPOINTS.RVB”

'Program: ProjectPoints

'Description: Projects points onto the image plane and converts the coordinates
'of the projected points into the distortion grid coordinate system

'Date Created: July 14, 2009

'Created by: Anne-Marie Allen

Call ProjectPoints

Sub ProjectPoints

Dim arrPoints, arrSurface, arrSource, arrPointsName, strPointsName

'User selects the surface to project the points onto

arrSurface = Rhino.GetObject("Click the surface (image plane) to project onto", 8)

If Not Rhino.IsSurface(arrSurface) Then

 Rhino.Print "Invalid surface selected. Please run code again."

 Exit Sub

End If

'User selects points to project

arrPoints = Rhino.GetObjects("Select 3D calibration points to project on to the surface")

Rhino.Print "Only click points which have corresponding 2D distortion corrected points."

If Not IsArray(arrPoints) Then

 Rhino.Print "Invalid points selected. Please run code again."

 Exit Sub

End If

'Determines how many points were picked

Dim intUBound

intUBound = UBound(arrPoints)

'Prints the points to be projected

arrPointsName = Rhino.ObjectNames(arrPoints)

Dim i

For i = 0 To intUBound

 strPointsName = arrPointsName(i)

 Rhino.Print "You selected point " & (strPointsName) & " to be projected"

Next

'User selects the fluoroscope source

arrSource = Rhino.GetObjects("Click the fluoroscope source", 1)

If Not IsArray(arrSource) Then

 Rhino.Print "Invalid source selected. Please run code again."

```

        Exit Sub
    End If

    'Determines the coordinates of the points
    For i = 0 To intUBound
        arrPoints(i) = Rhino.PointCoordinates(arrPoints(i))
        Rhino.Print "Point Coord is "
        Rhino.Print Rhino.Pt2Str(arrPoints(i))
    Next

    arrSource(0) = Rhino.PointCoordinates(arrSource(0))

    'Determines the vector between the source and each point
    ReDim arrVector(intUBound)
    For i = 0 To intUBound
        arrVector(i) = Rhino.PointSubtract(arrPoints(i), arrSource(0))
        Rhino.Print "vector is "
        Rhino.Print Rhino.Pt2Str(arrVector(i))
    Next

    'Determines the projection of each point onto the surface
    ReDim arrProjPoints(intUBound)
    For i = 0 To intUBound
        arrProjPoints(i) = Rhino.ProjectPointToSurface(arrPoints(i), arrSurface,
        arrVector(i))
        Rhino.Print "Proj Point Coord is "
        Rhino.Print Rhino.Pt2Str(arrProjPoints(i)(0))
    Next

    'Adds the projected points to the open document
    For i = 0 To intUBound
        Rhino.AddPoints arrProjPoints(i)
    Next

    'User enters the name of the Construction Plane (CPlane) which defines the distortion
    grid coordinate system
    Dim arrCPlane
    strCPlane = Rhino.GetString("Type in the name of the Construction Plane (
    CPlane) which defines the distortion grid coordinate system")
    arrCPlane = Rhino.NamedCPlane(strCPlane)
    If Not IsArray(arrCPlane) Then
        Rhino.Print "Invalid CPlane entered. Please run code again."
        Exit Sub
    End If

    'Transforms coordinates of the projected points from world to CPlane coordinates

```

```

ReDim arrCPlanePoints(intUBound)
For i = 0 To intUBound
    arrCPlanePoints(i)=Rhino.XformWorldToCPlane(arrProjPoints(i)(0), arrCPlane)
    Rhino.Print "Proj Point in CPlane coord is "
    Rhino.Print Rhino.Pt2Str(arrCPlanePoints(i))
Next

'Exports projected points to an excel file
Dim objExcel
Set objExcel = CreateObject("Excel.Application") 'Launch excel

objExcel.Visible = True 'Make excel visible

objExcel.WorkBooks.Add 'Add a new workbook

objExcel.Columns(1).ColumnWidth = 15
objExcel.Columns(2).ColumnWidth = 15
objExcel.Columns(3).ColumnWidth = 15
objExcel.Columns(4).ColumnWidth = 15
objExcel.Columns(5).ColumnWidth = 15

objExcel.Cells(1, 1).Value = "X Coord"
objExcel.Cells(1, 2).Value = "Y Coord"
objExcel.Cells(1, 3).Value = "Plane Type"
objExcel.Cells(1, 4).Value = "Plane Number"
objExcel.Cells(1, 5).Value = "Bead Number"

Dim intIndex
intIndex = 2

For i = 0 To intUBound
    strPointsName = arrPointsName(i)
    objExcel.Cells(intIndex + i, 1).Value = arrCPlanePoints(i)(0)
    objExcel.Cells(intIndex + i, 2).Value = arrCPlanePoints(i)(1)
    objExcel.Cells(intIndex + i, 3).Value = Mid(strPointsName,1,1)
    objExcel.Cells(intIndex + i, 4).Value = Mid(strPointsName,2,1)
    objExcel.Cells(intIndex + i, 5).Value = Mid(strPointsName,4,2)
Next

objExcel.Quit

End Sub

```


D.4 “ROT_TRANS_IMPLANE.M”

```
% Rot_Trans_ImPlane
% Description : Program that calculates the required image plane
% translation and rotation.
% Date Created: July 23, 2009
% Date Modified: Oct 13, 2009
% created by: Anne-Marie Allen

data_dir = ['C:\.....'];

% Obtain the location of the file containing all of the distortion
%corrected 2D fiducial and control points mm (fiducial = sheet1,
%control = sheet2)
points_file = input('Enter the name of the file which contains the distortion corrected 2D
fiducial and control points (fiducial = sheet1, control = sheet2): ','s');
points_filename = strcat(points_file, '.xls');
Fpoints = xlsread([data_dir,points_filename],1);
Cpoints = xlsread([data_dir,points_filename],2);

% Obtain the location of the file containing the projected points to
%use for image plane alignment (o/p from ProjectPoints.rvb)
proj_points_file = input('Enter the name of the file which contains projected calibration
frame points (o/p from ProjectPoints.rvb): ','s');
proj_points_filename = strcat(proj_points_file, '.xls');
[proj_points,proj_points_txt] = xlsread([data_dir,proj_points_filename],1);

%Determines which cells contain fiducial and calibration beads
F = strmatch('F', proj_points_txt(:,3));
C = strmatch('C', proj_points_txt(:,3));

%Extracts the corresponding distortion corrected fiducial points
for i=1:1:size(F)
    bead_no=proj_points(F(i,1)-1,5);
    dist_cor_points(F(i,1)-1,1)= Fpoints(bead_no,2);
    dist_cor_points(F(i,1)-1,2)= Fpoints(bead_no,3);

    if dist_cor_points(F(i,1)-1,1)==5555
        bead_no
        sprintf('%s %d %s %d %s','The fiducial bead', bead_no, 'was not digitized.
        Please delete the', i,'th row from the ProjectPoints file and run code again');
        return
    end
end
end
```

```

%Extracts the corresponding distortion corrected control points
for i=1:1:size(C)
    bead_no=proj_points(C(i,1)-1,5);
    dist_cor_points(C(i,1)-1,1)= Cpoints(bead_no,2);
    dist_cor_points(C(i,1)-1,2)= Cpoints(bead_no,3);

    if dist_cor_points(C(i,1)-1,1)==5555
        bead_no
            sprintf('%s %d %s %d %s','The control bead', bead_no, 'was not digitized.
            Please delete the', i,'th row from the ProjectPoints file and run code again');
        return
    end
end

%starting estimates
points_new0(:,.) = proj_points(:,1:2);

options = optimset('LargeScale',
'off','MaxFunEvals',5000,'TolFun',0.001,'TolCon',0.001,'TolX',0.001);

[points_new,RMSE_dist,exitflag,output]=fmincon('Rot_Trans_ImPlane_objfun',points_n
ew0,[],[],[],[],[],[],'Rot_Trans_ImPlane_confun',options,proj_points);

% Find point closest and furthest from the centre of the distortion grid
size=size(dist_cor_points);
dmax = 50;
dmin = 50;
for i = 1:1:size
    d = sqrt((dist_cor_points(i,1)^2)+(dist_cor_points(i,2)^2));
    if d > dmax
        dmax = d;
        max_row = i;
    elseif d < dmin
        dmin = d;
        min_row = i;
    end
end

% Image Displacement Correction (mm)
dispx = points_new(min_row,1)-dist_cor_points(min_row,1);
dispy = points_new(min_row,2)-dist_cor_points(min_row,2);

% Image Rotation Correction (rads)

% Translated furthest and closest point by image displacement correction
trans_dist_cor_points(1,1) = dist_cor_points(min_row,1)+dispx;

```

```

trans_dist_cor_points(1,2) = dist_cor_points(min_row,2)+dispy;
trans_dist_cor_points(2,1) = dist_cor_points(max_row,1)+dispx;
trans_dist_cor_points(2,2) = dist_cor_points(max_row,2)+dispy;

% Create a vector using the translated distortion corrected points
trans_dist_cor_points_v(1,:) = trans_dist_cor_points(2,:) - trans_dist_cor_points(1,:);

% Create a vector using the corresponding new points
new_points_v(1,:) = points_new(max_row,:) - points_new(min_row,:);

% Angle between distortion corrected vector and the distortion grid
% horizontal axis
dist_cor_points_a =
atan2(dot(trans_dist_cor_points_v(1,:),[0,1]),dot(trans_dist_cor_points_v(1,:),[1,0]));

% Angle between new points vector and the distortion grid
% horizontal axis
new_points_a = atan2(dot(new_points_v(1,:),[0,1]),dot(new_points_v(1,:),[1,0]));

% Angle between distortion corrected vector and new points vector
rot = new_points_a - dist_cor_points_a;

rot_pt_type = char(proj_points_txt(min_row+1,3));
rot_pt_num = double(proj_points(min_row,5));

sprintf('%s %d %s %d %s','Translate the image by', dispx, 'mm in horizontal distortion
grid axis and', dispy,'mm in the vertical distortion grid axis ')
sprintf('%s %d %s %s %d %s','Rotate the image by ', rot, 'rad about the', rot_pt_type
,rot_pt_num,'distortion corrected point')

```

D.5 “ROT_TRANS_IMPLANE_OBJFUN.M”

```
%Program:Rot_Trans_ImPlane_objfun
%Description: Objective function for the Rot_Trans_ImPlane optimization %routine
%Date Created: July 23, 2009
%Written by: Anne-Marie Allen

function RMSE_dist = Rot_Trans_ImPlane_objfun(points_new,proj_points)

sum_dist=0;
proj_points_size=size(proj_points);

for i=1:proj_points_size

    dist(i,1) = ((proj_points(i,1) - points_new(i,1))^2)+((proj_points(i,2)-
points_new(i,2))^2);

    sum_dist = sum_dist + dist(i,1);
end

% root mean square error (RMSE)(mm) between projected points and new points
RMSE_dist = sqrt((sum_dist)/proj_points_size(1,1));
```

D.6 “ROT_TRANS_IMPLANE_CONFUN.M”

```

%Program:Rot_Trans_ImPlane_confun
%Description: Constraint function for the Rot_Trans_ImPlane function
%Date Created: July 23, 2009
%Date Modified: Oct 1, 2009
%Written by: Anne-Marie Allen

function[c,ceq]=Rot_Trans_ImPlane_confun(points_new,dist_cor_points)

%nonlinear inequality constraints c(x)<= 0
c=[];

%linear equality constraints ceq(x) = 0
k=1;

%distance constraints

%first end of line
for i=1:size(dist_cor_points)-1

    %second end of line
    for j=i+1:size(dist_cor_points)-1

        %distance between distortion corrected points
        dist_const(k,1) = sqrt(((dist_cor_points(i,1)-
            dist_cor_points(j,1))^2)+((dist_cor_points(i,2)-dist_cor_points(j,2))^2));

        %distance between new points
        dist_new(k,1) = sqrt(((points_new(i,1)-points_new(j,1))^2)+((points_new(i,2)-
            points_new(j,2))^2));

        %constrains the distance between distortion corrected points and
        corresponding new points to be equal
        ceq(1,k)=(dist_const(k,1)-dist_new(k,1));

        k=k+1;
    end
end

end

```

APPENDIX E – INSTRUCTIONS FOR EXPERIMENTAL SET-UP RECREATION IN RHINOCEROS

E.1 INITIAL NOTES

This appendix details the steps required to model the experimental set-up of one fluoroscope in Rhinoceros. The experimental set-up that will be recreated is the same set-up from Section 2.2.1. The following calibration parameters and picture (Figure E.1) will be used:

- Fluoroscope B
- x-ray source coordinates = -650.6155, 109.0026, 313.3554 mm
- Euler angle sequence = $Rot(Z, -0.1006rad) Rot(Y, 0.2395rad) Rot(X, 0.03574rad)$
- Distance $d = 999.9911$ mm
- Image plane size = 720×540pix (274.972×206.229mm)

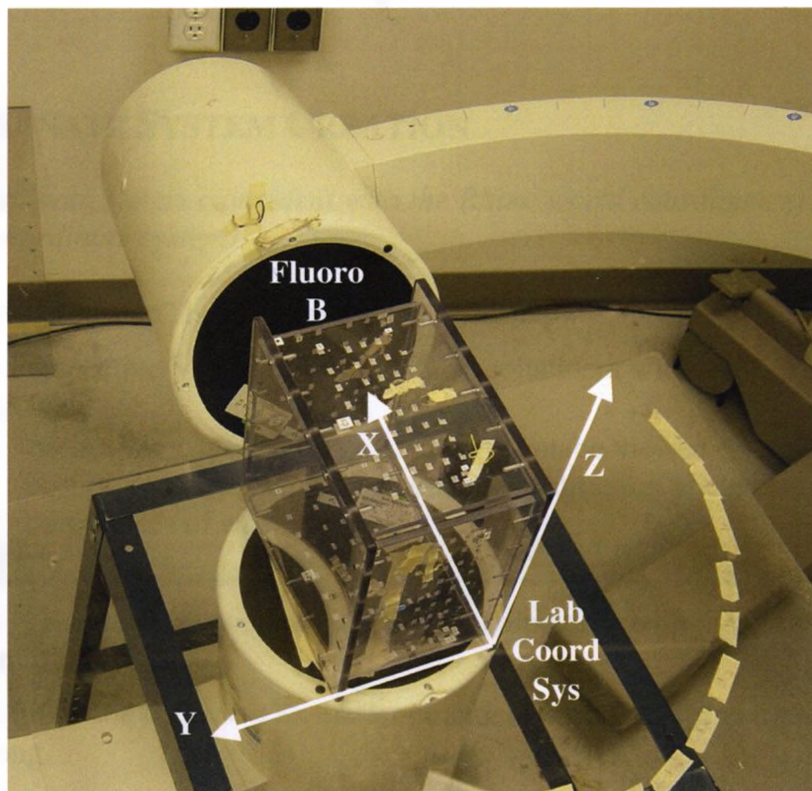


Figure E.1: Picture of experimental set-up

Settings

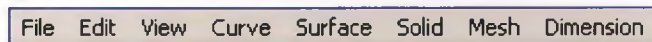
1. Once you open Rhinoceros, choose “Small Objects – Millimeters” as the Startup Template.
2. Ensure that following toolbars are displayed (Tools → Toolbar Layout...):
 - a. “Main1”

- b. "Main2"
 - c. "Standard"
 - d. "Lines"
3. If the Gridlines are obstructing your view, you can turn them off by using the menu bar (Tools → Options → Document Properties → Grid → Show Gridlines)

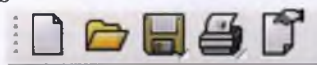
Initial Notes

You can navigate in Rhino by using the following:

- Menu bar



- Buttons




- Command line








- o When using the command line, type in the command name, press enter and follow the displayed instructions.

E.2 COORDINATE SYSTEM CREATION

Create a coordinate system coincident with the Rhino world coordinate system (laboratory coordinate system)

1. Ensure "Gridsnap" is on (**Command:** Gridsnap)
2. In the Perspective View, draw a line  coincident with the X (red) axis that is 10 mm long.
 - As the line is being drawn, its length can be viewed on the bottom left portion of the screen. These are the construction plane coordinates (i.e. coordinates of each image)

CPlane	x 0.000	y 10.000	z 0.000	10.000
--------	---------	----------	---------	--------
3. In the Perspective View, draw a line  coincident with the Y (green) axis that is 10 mm long.
4. In the Front View, draw a line  coincident with the Z (blue) axis that is 10 mm long.
5. Colour the lines by clicking a line and then clicking  → Display Color
 - X = red
 - Y = green
 - Z = blue
6. The line length and line start/end coordinates can be confirmed by clicking  → Details
7. Group the 3 lines together to create a coordinate system

- **Command: Group**
 - click the 3 lines
 - press enter
- 8. Copy and paste the group in the same location.
- 9. Name one group “LabCoordSys” and one group “FluoroBCoordSys”
(**Command: SetGroupName**)
- 10. Right click  to automatically zoom into the objects. Your screen should look like Figure E.2.

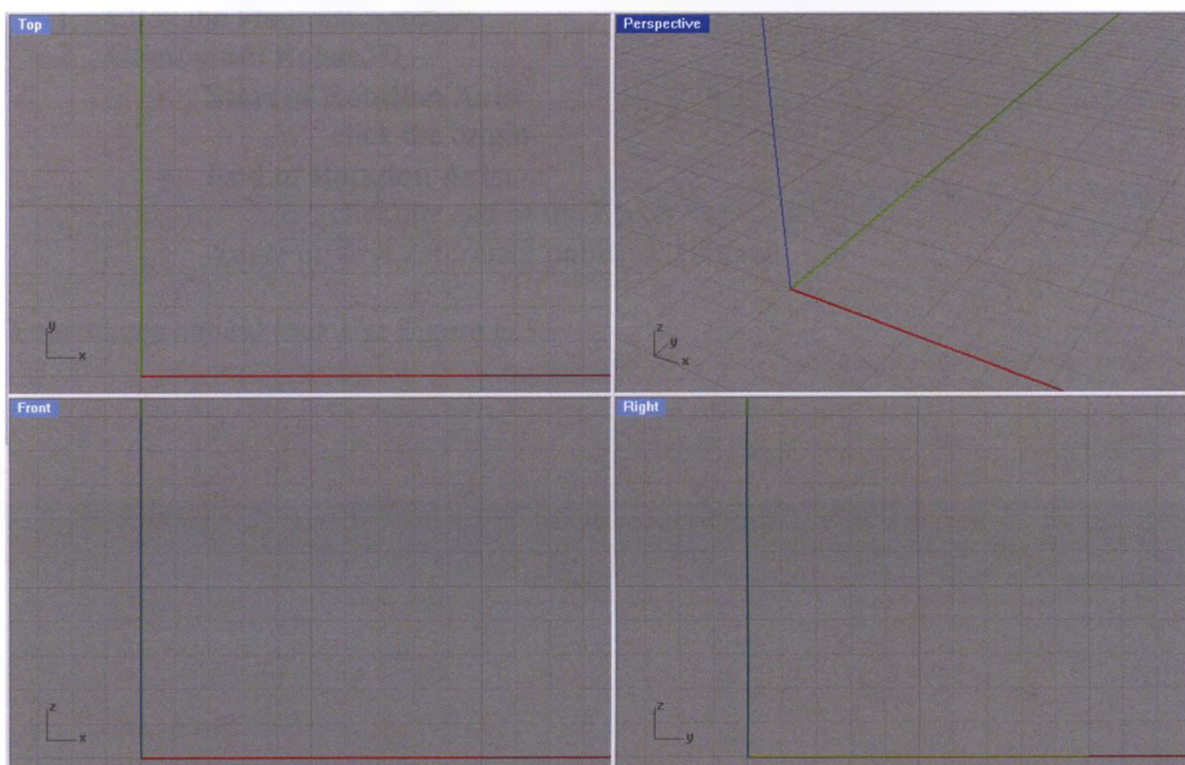


Figure E.2: Creating coordinate systems

E.3 EULER ANGLE ROTATIONS

Rotate the “FluoroBCoordSys” according to the angles calculated during the calibration algorithm. For this example we will assume the following sequence:
 $\text{Rot}(Z, -0.1006\text{rad})$ $\text{Rot}(Y, 0.2395\text{rad})$ $\text{Rot}(X, 0.03574\text{rad})$

$\text{Rot}(Z, -0.1006\text{rad})$

1. Click the FluoroBCoordSys.
2. **Command:** Rotate3D
 - **Start of Rotation Axis:**
 - click the origin
 - **End of Rotation Axis:**
 - click the end of the Z axis
 - **Angle or first reference point:** -0.1006rad

Your screen should look like Figure E.3

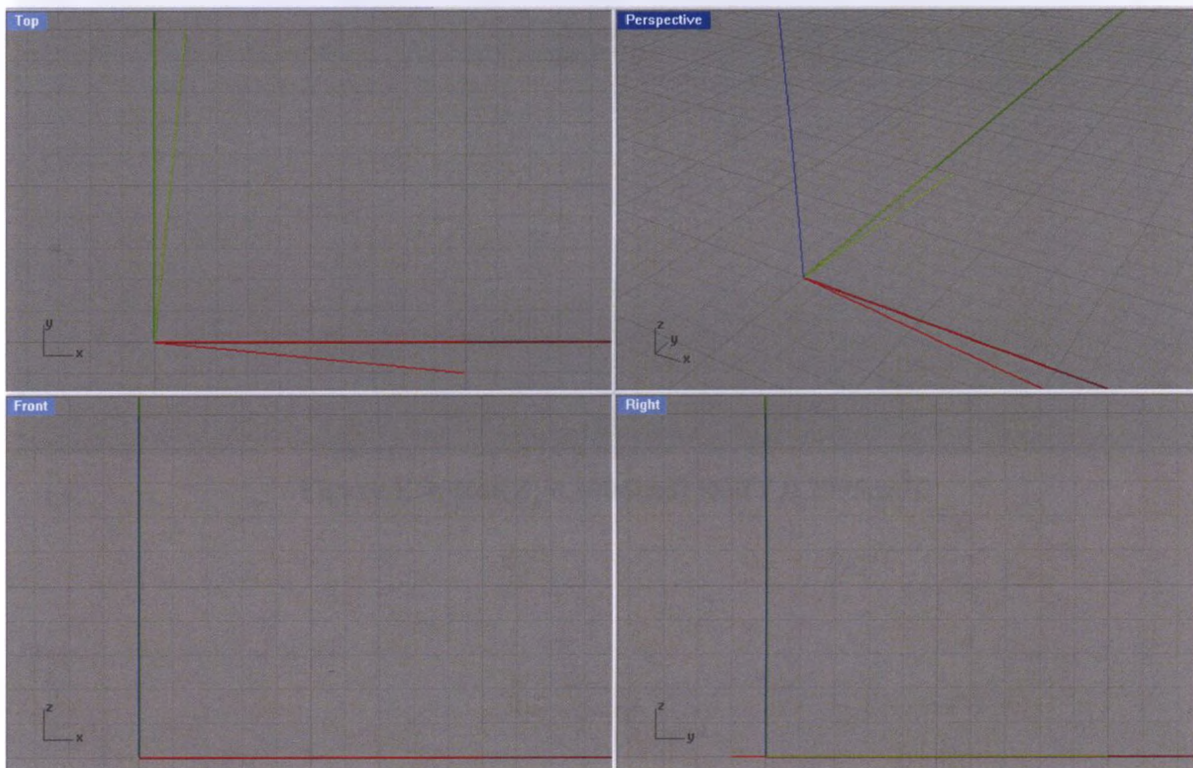


Figure E.3: $\text{Rot}(Z, -0.1006\text{rad})$

$Rot(Y, 0.2395rad)$

3. Click the FluoroBCoordSys.

4. **Command:** Rotate3D

- **Start of Rotation Axis:**
 - click the origin
- **End of Rotation Axis:**
 - click the end of the Y axis of the FluoroBCoordSys
- **Angle or first reference point:** 0.2395rad

Your screen should look like Figure E.4.

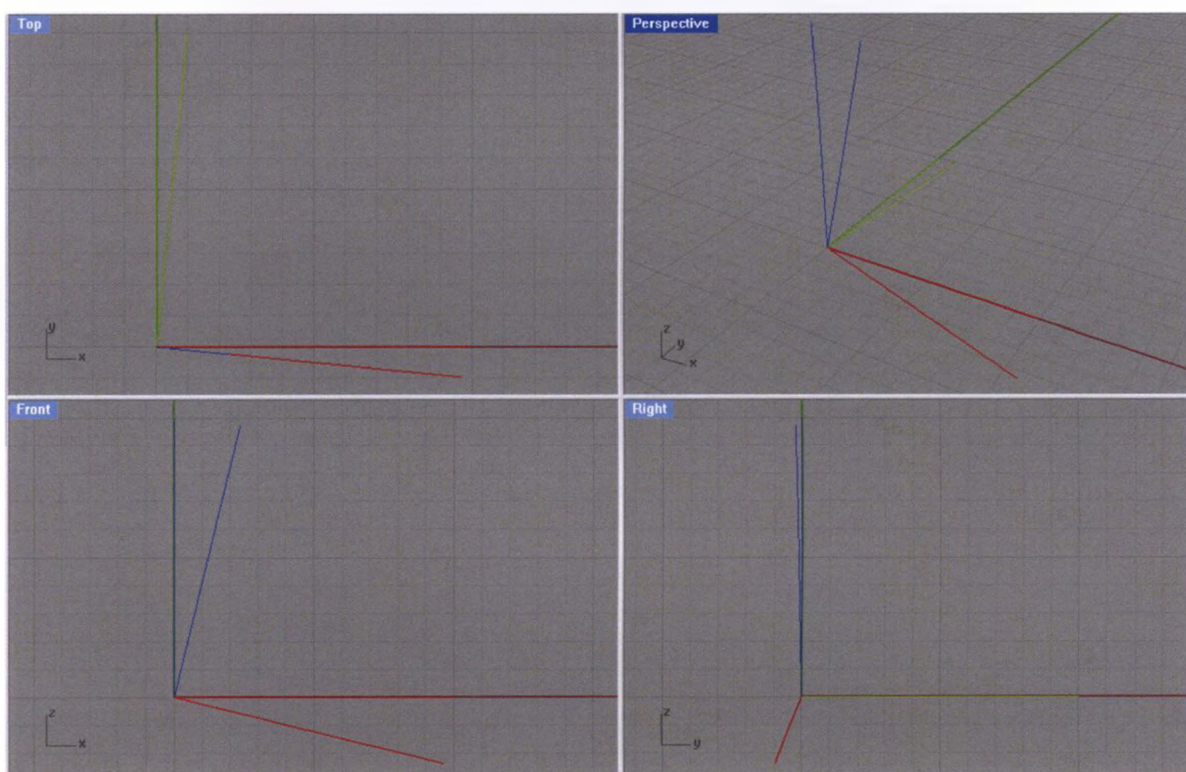


Figure E.4: $Rot(Z, -0.1006rad)$ $Rot(Y, 0.2395rad)$

Rot (X,0.03574rad)

5. Click the FluoroBCoordSys.

6. **Command:** Rotate3D

- **Start of Rotation Axis:**
 - click the origin
- **End of Rotation Axis:**
 - click the end of the X axis of the FluoroBCoordSys
- **Angle or first reference point:** 0.03574rad

Your screen should look like Figure E.5.

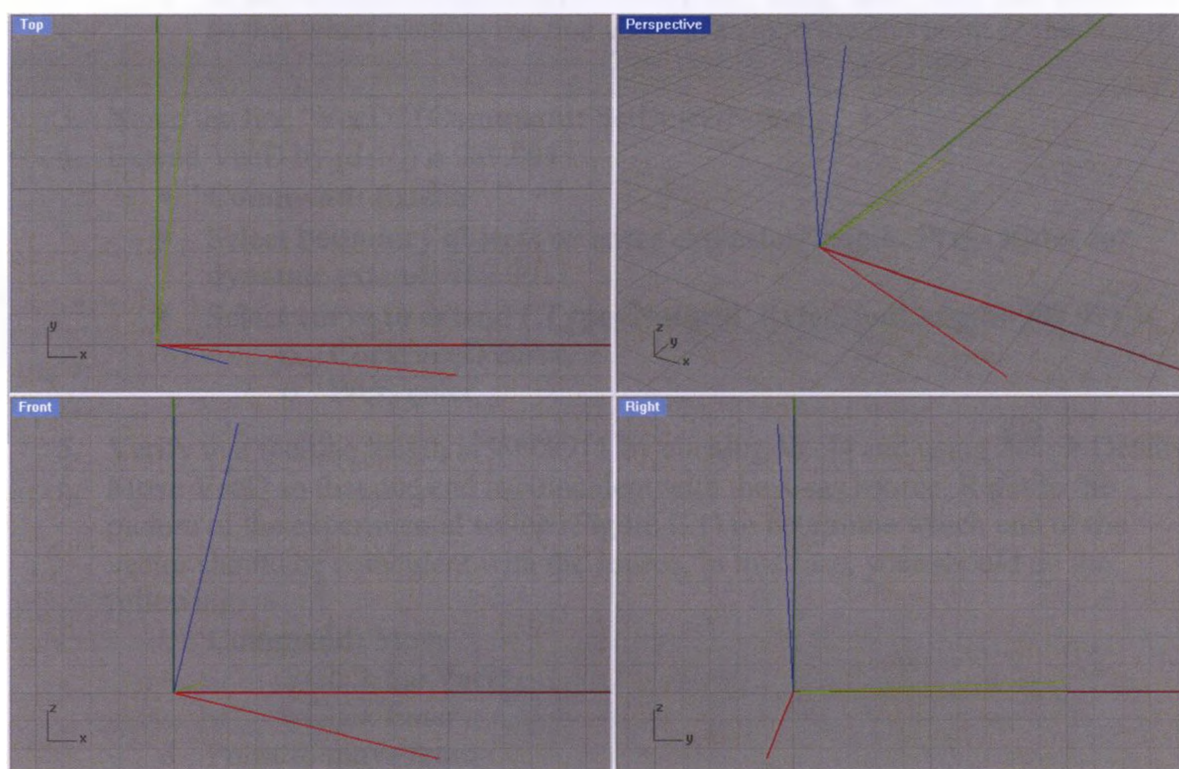


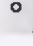
Figure E.5: Rot(Z,-0.1006rad) Rot (Y,0.2395rad) Rot (X,0.03574rad)

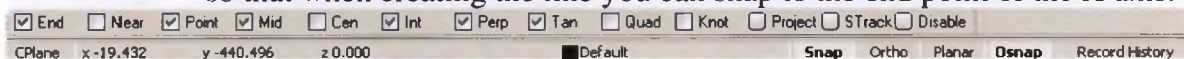
E.4 VECTOR CREATION


Create a vector using the axis about which the final rotation was made (X' in this example). One end of the vector coincides with the corresponding x-ray source and its length is defined by d , as calculated during the calibration.

For this example we will assume the following:

- X-ray source coordinates = -650.6155, 109.0026, 313.3554
- $d = 999.9911$

1. Create a point  to define the x-ray source. Make sure there are no spaces when you enter point coordinates into the command line.
2. Create a line coincident with the X axis of the FluoroBCoordSys.
 - In the bottom left hand corner ensure the “Snap” and “End” are turned on so that when creating the line you can snap to the end point of the X axis.



3. Name the line “VecD” (**Command: SetObjectName**)
4. Extend VecD by $(d-10) = 989.9911$
 - **Command: Extend**
 - **Select boundary objects or enter extension length. Press Enter for dynamic extend: 989.9911**
 - **Select curve to extend (Type=Natural ExtensionLength=989.991):**
 - Click VecD curve
 - Press enter
5. Verify that the line length is 999.9911 by clicking VecD and using  → Details
6. Move VecD so that one end is coincident with the x-ray source. Refer to the picture of the experimental set-up (Figure E.1) to determine which end of the vector should be coincident with the source. In this case, you should do the following:
 - **Command: Move**
 - Click the VecD
 - Click Enter
 - **Point to move from :**
 - Click the “FluoroBCoordSys” origin
 - Press Enter
 - **Point to move to:**
 - Click the x-ray source

Your screen should now look like Figure E.6.

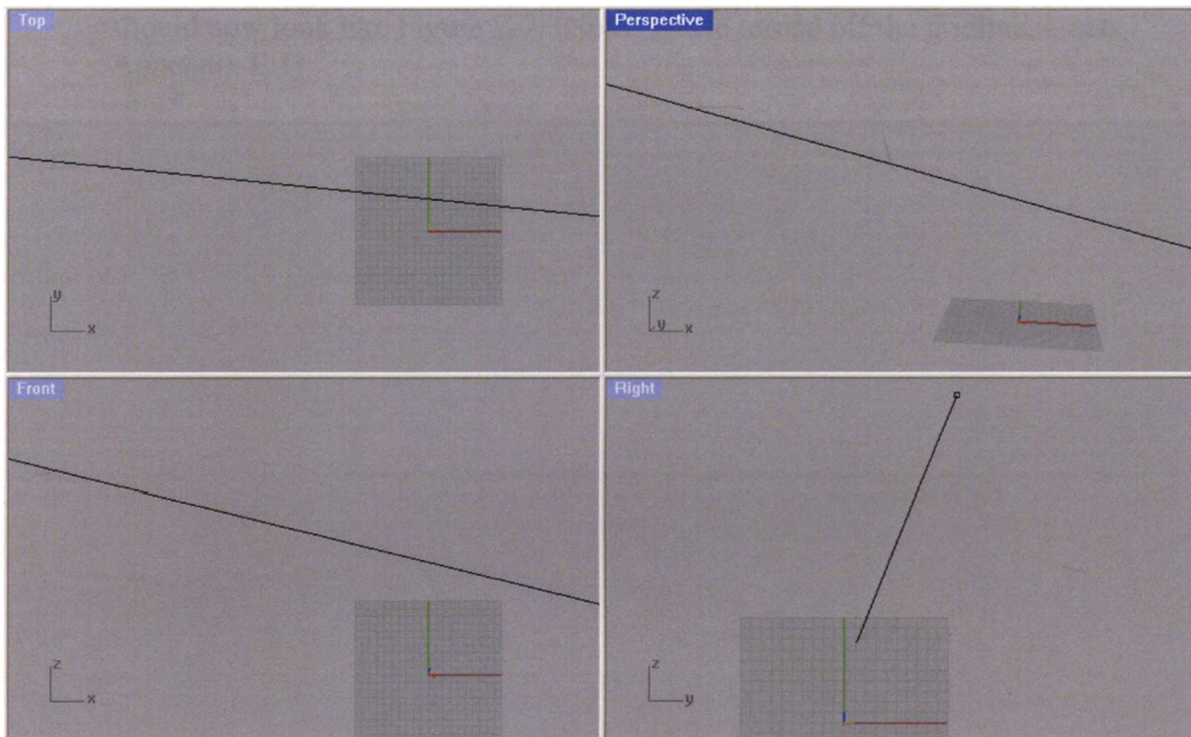


Figure E.6: Vector creation

E.5 IMAGE PLANE

Create and orient the image plane. For fluoroscope B, the dimensions are 720×540pix with 0.3819mm/pix = 274.972×206.229mm.

Image Plane Creation

1. Create a coordinate system by following the steps 1-7 in the previous “Coordinate Creation” section or by copying and pasting the “LabCoordSys”
2. Name the group “FluoroB-ProjCoordSys”
3. By viewing Figure 2.6, it can be seen that the projection coordinate system’s:
 - Z’ axis -> parallel to the vertical image plane edge
 - Y’ axis -> parallel to the horizontal image plane edge
 - X’ axis -> perpendicular to the image plane.

Therefore, create the image plane in the “Right” view = ZY plane.

You might need to right-click “Right” and Set View to “Right”

With the FluoroB-ProjCoordSys origin in the centre of the image, two opposite corner coordinates are (137.486,103.115) and (-137.486,-103.115)

Command: Rectangle

First corner of rectangle: 137.486,103.115

Other corner of length: -137.486,-103.115

4. Group the rectangle (image plane) and “FluoroB-ProjCoordSys” together and name this group “FluoroB-ImPlane” (**Command:** SetGroupName). Your screen

should now look like Figure E.7. (Note: I have turned off the gridlines – see Appendix E.1)

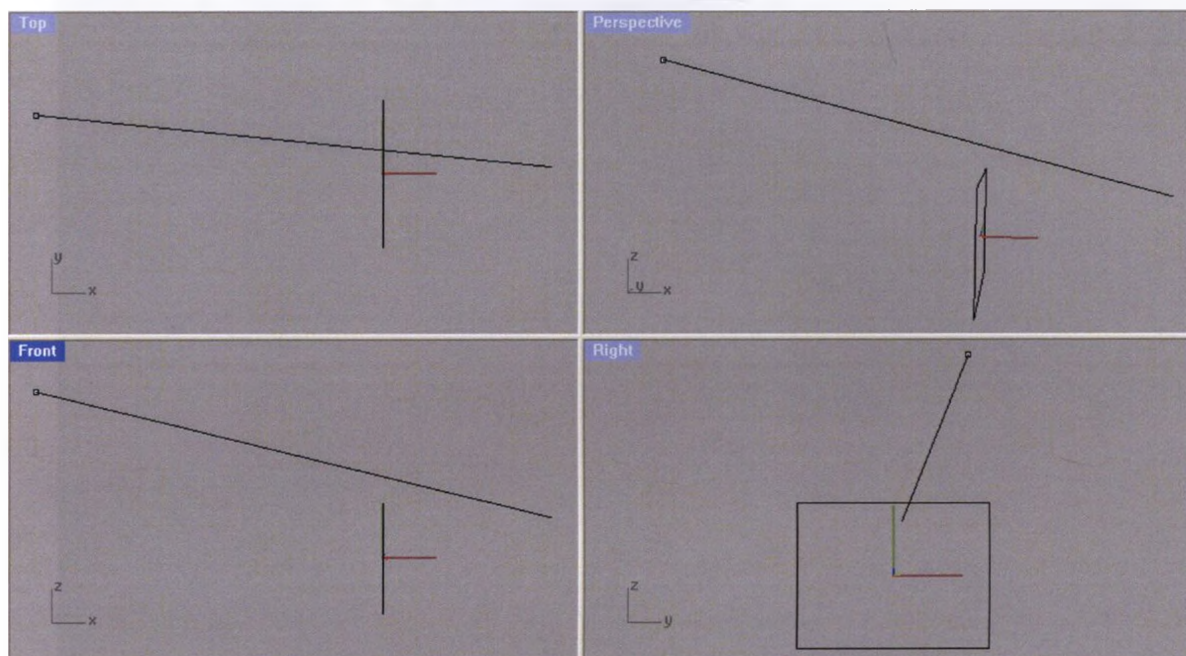


Figure E.7: Image plane creation

Image Plane Orientation

5. First zoom into the origin in the Perspective View (Figure E.8).
6. We know the “FluoroBCoordSys” is in the correct orientation, so we need to orient the “FluoroB-ImPlane” group to the “FluoroBCoordSys”.
 - **Command:** Orient3Pt
 - **Select objects to orient:**
 - Click the “FluoroB-ImPlane” group
 - **Reference point 1:**
 - Click the end of the “FluoroB-ImPlane” X-axis
 - **Reference point 2:**
 - Click the end of the “FluoroB-ImPlane” Y-axis
 - **Reference point 3:**
 - Click the end of the “FluoroB-ImPlane” Z-axis
 - **Target point 1:**
 - Click the end of the “FluoroBCoordSys” X-axis
 - **Target point 2:**
 - Click the end of the “FluoroBCoordSys” Y-axis
 - **Target point 3:**
 - Click the end of the “FluoroBCoordSys” Z-axis

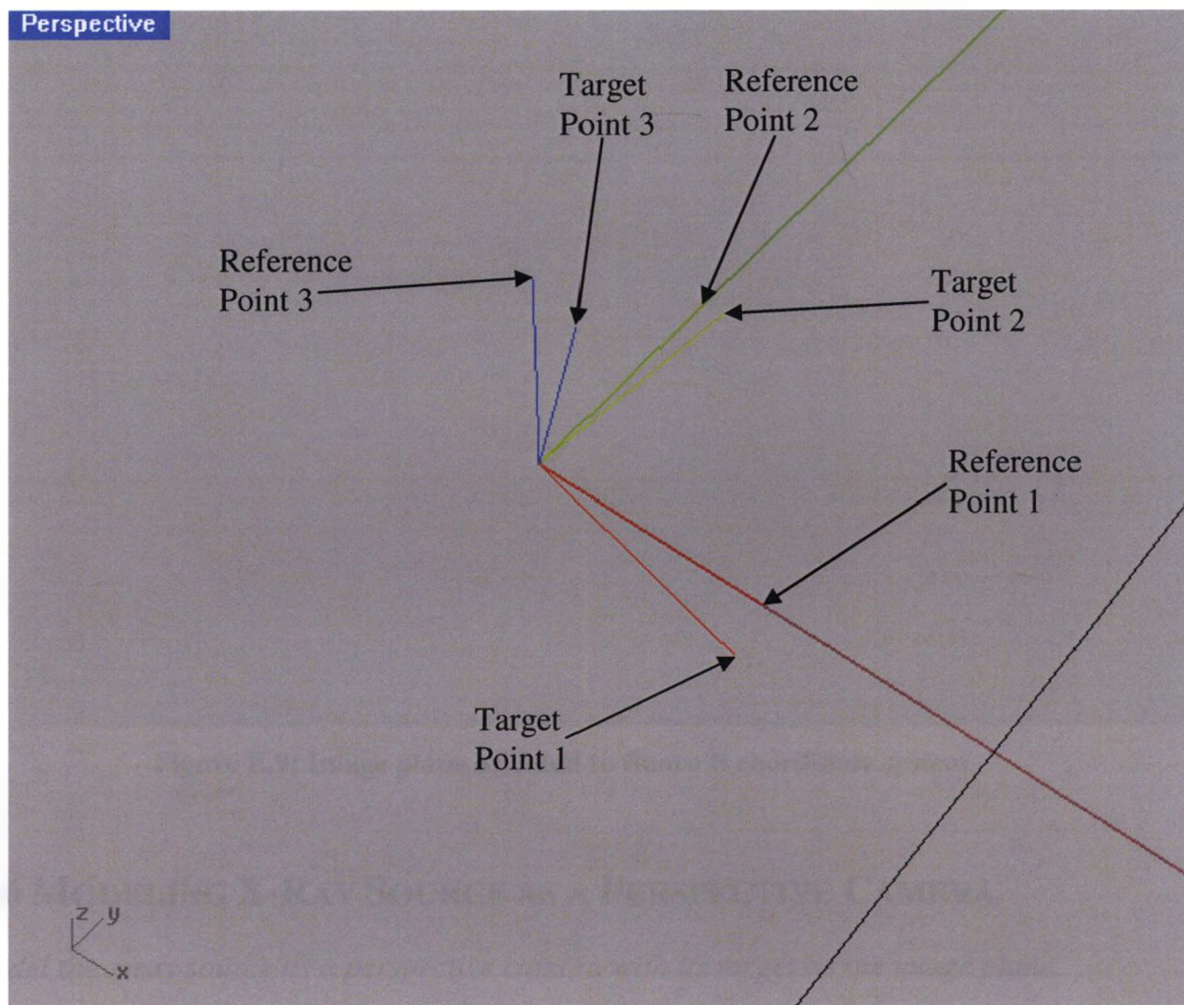


Figure E.8: Guide to orient image plane to fluoro B coordinate system

7. To ensure that the “FluoroB-ImPlane” is oriented correctly, click the “FluoroBCoordSys” and the “FluoroB-ImPlane” should also be selected/highlighted. The “LabCoordSys” should not be selected/highlighted. If this is not the case, redo Step #7.
8. With the “FluoroB-ImPlane” oriented correctly Move the FluoroBCoordSys such that its origin is coincident with the end of the d vector opposite the source.
 - **Command: Move**
 - Click the “FluoroB-ImPlane”
 - Click Enter
 - **Point to move from :**
 - Click the “FluoroB-ImPlane” origin
 - Press Enter
 - **Point to move to:**
 - Click the end of the d vector opposite the source

Your screen should now look like Figure E.9.

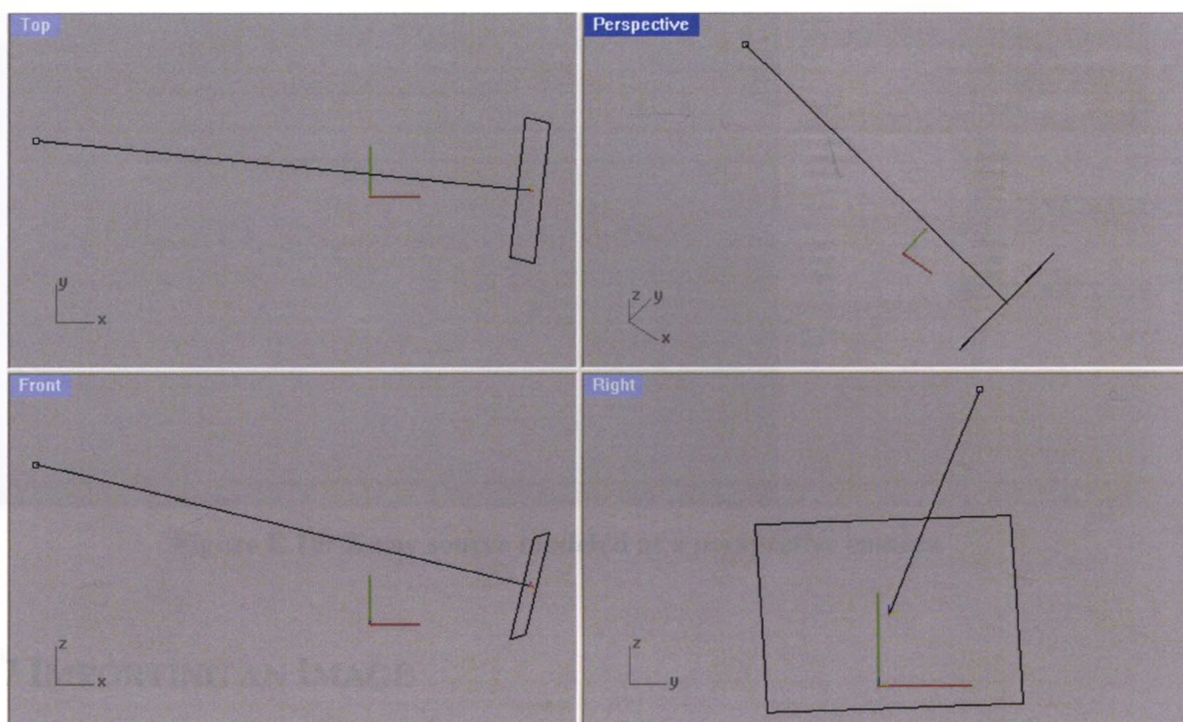






Figure E.9: Image plane oriented to fluoro B coordinate system

E.6 MODELING X-RAY SOURCE AS A PERSPECTIVE CAMERA

Model the x-ray source as a perspective camera with its target on the image plane.

1. Click on the view that is most parallel to the image plane. In this case it is the "Right View".
2. Change the projection from parallel to perspective.  → Projection: Perspective.
3. Change the camera location to the x-ray source.  → Camera → Place Button → click the x-ray source
4. Change the target location to the origin of the "FluoroB-ImPlane".
 → Target → Place Button → click origin of the "FluoroB-ImPlane"
5. Change the Lens length to the 100.
6. You can rotate the image in the image plane using
 - **Command:** Tiltview
7. Name this view "B". Right click on "Right" 
 - Set View → Named Views... → Save → Type in "B" → Ok → Close

Note: Do not zoom in and out of the image with the scrolley mouse. You must change the Camera Lens Length in the "Viewport" Properties page.

Your screen should now look like Figure E.10.

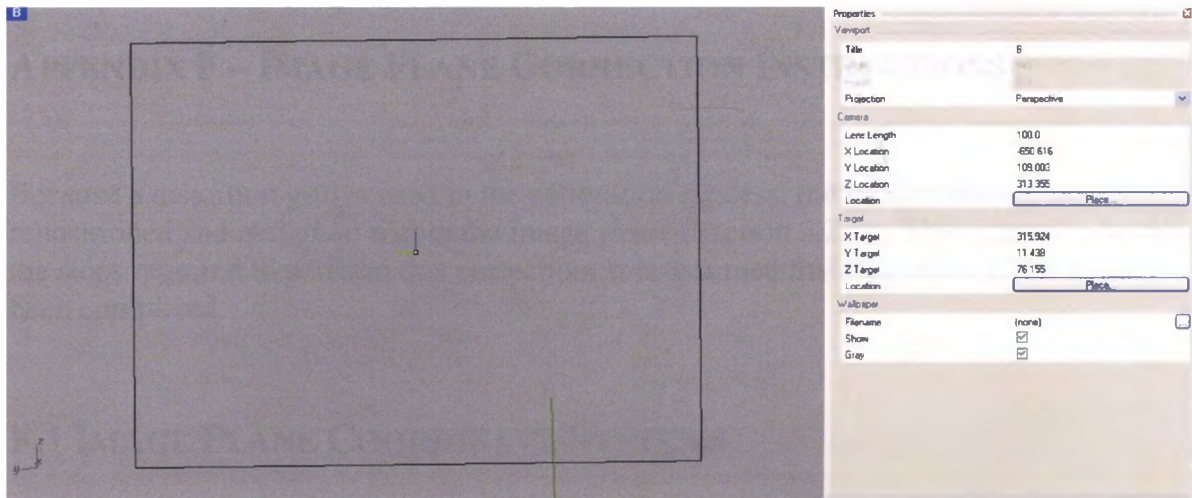




Figure E.10: X-ray source modeled as a perspective camera

E.7 IMPORTING AN IMAGE

Import an image onto the image plane.

1. Create a surface using the image plane.
 - 
 - **First corner of surface:** Click the bottom left hand corner
 - **Second corner of surface:** Click the bottom right hand corner
 - **Third corner of surface:** Click the top right hand corner
 - **Fourth corner of surface:** Click the top left hand corner
2. Right click the view “B”
 - Set CPlane → To Object → Click the surface
3. Place an image on image plane using the “PictureFrame” command
 - **Command:** PictureFrame
 - Find the image to import
 - **First corner of picture frame:** Click bottom left hand corner
 - **Length of picture:** Click the bottom right hand corner
4. To change the image.
 - Click on the image.
 -  Properties → Material (in drop down menu) → Texture → Map File

Note: The image must be saved in the same folder as the Rhino file

***Please read Appendix F for instructions on the required image plane correction**

APPENDIX F – IMAGE PLANE CORRECTION INSTRUCTIONS

Because a distortion grid is used in the calibration process, the image needs to be repositioned and realigned within the image plane (Section 2.2.2). This appendix details the steps required to perform this correction. It is assumed that Appendix E has already been completed.

F.1 IMAGE PLANE COORDINATE SYSTEMS

The CPlane of a view defines the 2D coordinate system of the image. We need to create two CPlanes (coordinate systems): a pixel grid coordinate system and a distortion grid coordinate system

“PixelGridCoordSys” – corresponds to the coordinate system used in MATLAB when digitizing points, specifically Angela Kedgley’s “pick_points” code (Kedgley, 2009a)

- The coordinate system’s position and orientation is the same for all images and calibration set-ups (Figure F.1)
 - origin = bottom left hand corner of the image
 - x axis = points to the right along the horizontal axis of the image
 - y axis = point upwards along the vertical axis of the image

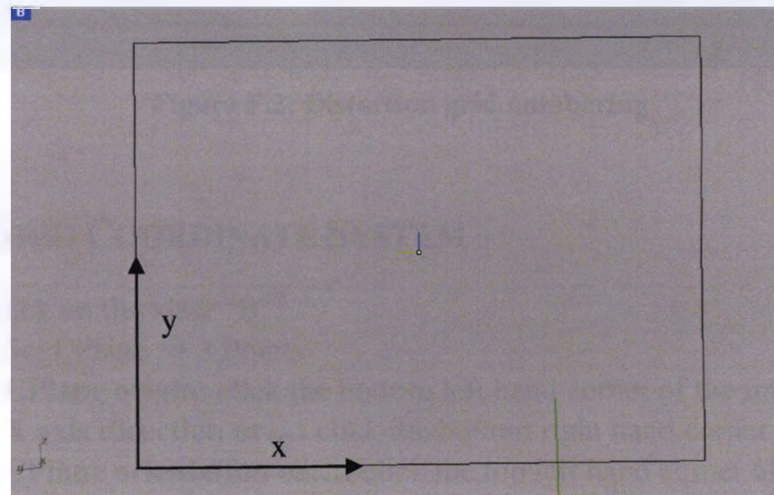


Figure F.1: Pixel grid coordinate system

“DistGridCoordSys” – corresponds to the coordinate system used for distortion-corrected points

- The coordinate system’s position and orientation is NOT the same for each calibration set-up, but depends on the position/orientation of the distortion grid on the II (see Section 2.2.2)
 - origin = centre bead (#70) of the distortion grid

- x axis = points to the left along beads # 51 – 57
- y axis = points down along beads # 57,44,32,20,10,3 (Figure F.2)

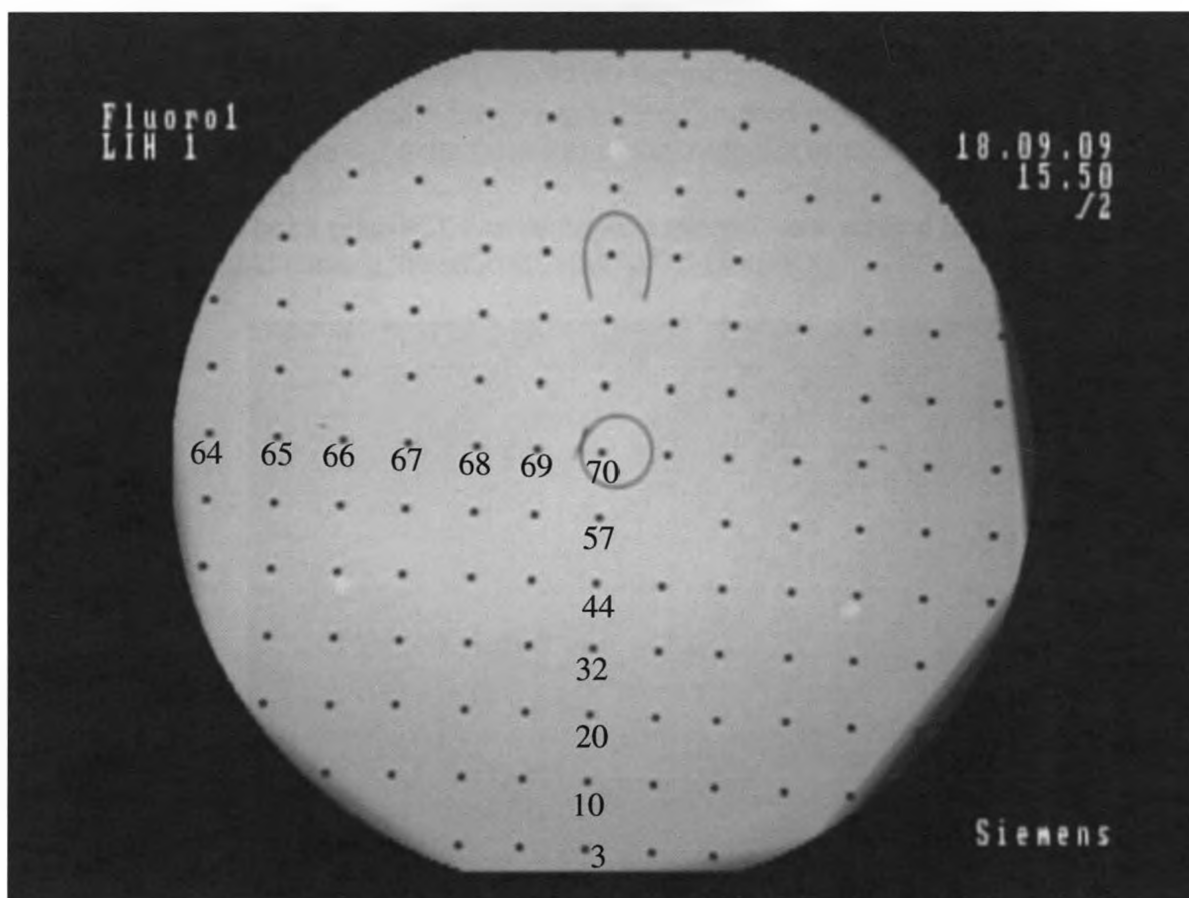


Figure F.2: Distortion grid numbering

F.2 PIXEL GRID COORDINATE SYSTEM

1. Right-click on the view "B".
 - Set CPlane → 3 Points
 - **CPlane origin:** click the bottom left hand corner of the image
 - **X axis direction or...:** click the bottom right hand corner of image
 - **CPlane orientation or...:** click the top left hand corner of the image
2. You can check that CPlane you have created is correct by moving the cursor around and observing that the CPlane coordinates displayed in the bottom left-hand corner of the screen correspond to the correct pixel grid coordinate system as shown in Figure F.1
3. Save the CPlane. Right-click on the view "B"
 - Set CPlane → Named CPlanes → Save → Type in "PixelGridCoordSys" → Ok → Close

F.3 DISTORTION GRID COORDINATE SYSTEM

1. Change the image to the fluoroscopic image taken of the distortion grid.
2. Create a point at the centre of the image.
3. Draw a line from the point (step #2) to the midpoint of the left edge of the image. (this will be easier if you have snap to “mid” turned on)
4. Draw a line from the point (step #2) to the midpoint of the bottom edge of the image.
5. Group the point (step #2), horizontal line (step#3) and vertical line (step#4) together and name it “DistGridCoordSys” (Figure F.3)

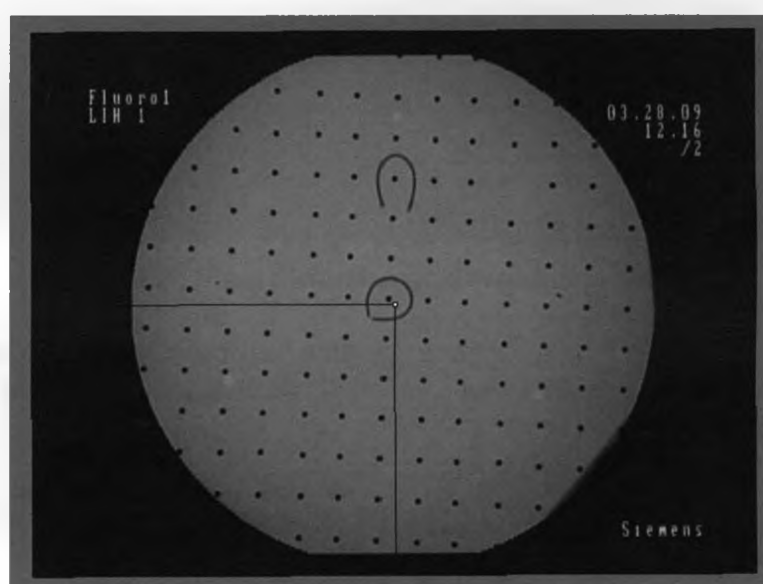


Figure F.3: Initial distortion grid coordinate system

6. Ensure the CPlane is set to the “PixelGridCoordSys” while completing steps #7 - 10!
7. Open MATLAB and run “DistGrid_RotTrans.m” (Appendix D.1) to calculate the origin of the “DistGridCoordSys” and axes rotation
8. Plot the new “DistGridCoordSys” origin. The origin should match the location of the #70 distortion grid bead (Figure F.2).
9. Move the “DistGridCoordSys” from the centre of the image to the “DistGridCoordSys” origin (point from step #8) (**Command:** Move)
10. Rotate the “DistGridCoordSys” about the “DistGridCoordSys” origin by the rotation angle found in step #7 (**Command:** Rotate) The axes should align with the distortion grid beads. (Figure F.4)

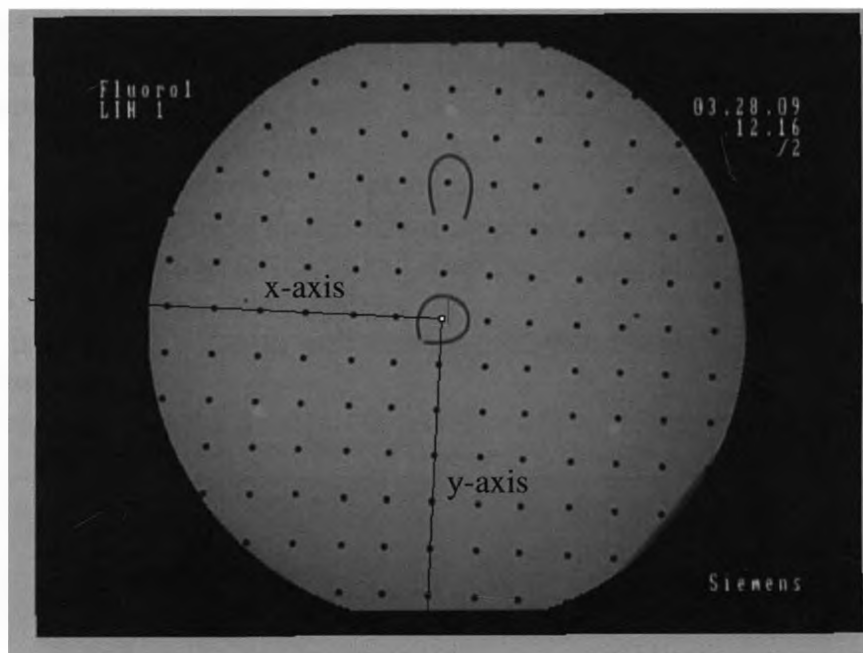


Figure F.4: Final distortion grid coordinate system

11. Group the "DistGridCoordSys" with the image.
12. You will save the "DistGridCoordSys" as a new CPlane in the next section.

F.4 INITIAL ESTIMATE OF IMAGE PLANE CORRECTION

1. Rotate the image about the "DistGridCoordSys" origin by the negative angle found from the "DistGrid_RotTrans.m" code
2. Translate the image from the "DistGridCoordSys" origin to the centre of the image plane. The origin and axes should still be aligned with the distortion grid beads (Figure F.4)
3. Right-click on the view "B".
 - Set CPlane → 3 Points
 - **CPlane origin:** click the origin of the "DistGridCoordSys"
 - **X axis direction or...:** click the end of rotated horizontal line (x axis in Figure F.4)
 - **CPlane orientation or...:** click the end of the rotated vertical line (y axis in Figure F.4)
4. Save the CPlane. Right-click on the view "B"
 - Set CPlane → Named CPlanes → Save → Type in "DistGridCoordSys" → Ok → Close

F.5 FINAL IMAGE PLANE CORRECTION

1. Change the image to the fluoroscopic image taken of the calibration frame

2. Run “ImportPoints.rvb” (Appendix D.2) in Rhinoceros to plot the distortion-corrected calibration points onto the image plane.

3. **Command:**_LoadScript

- Add the “ImportPoints.rvb” script
- Double click on the script to run it
- Select the file with the distortion corrected 2D calibration points (sheet1=fiducial points and sheet2=control points)
- Type in DistGridCoordSys

The points should line up well with the calibration point as seen on the image (Figure F.5).

4. Group the image and 2D distortion-corrected point together.

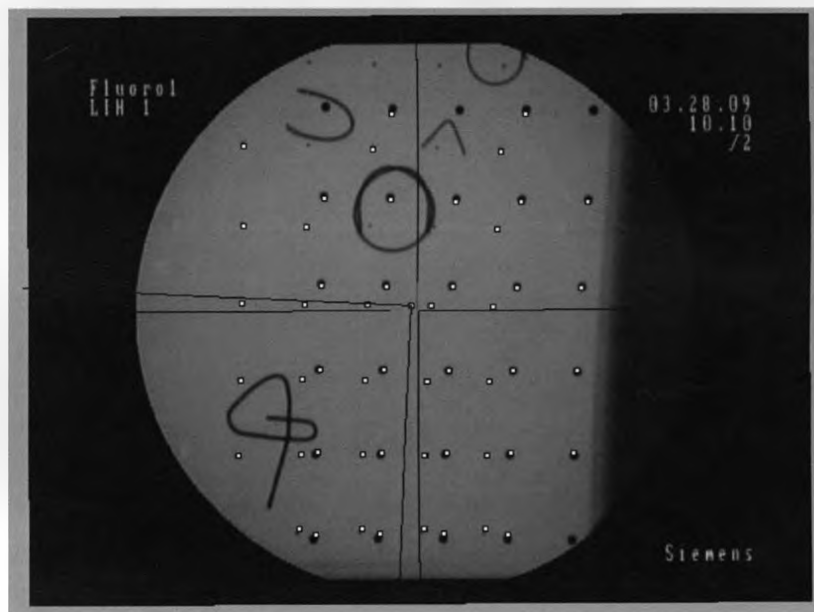


Figure F.5: Calibration image with 2D distortion-corrected points as open squares and uncorrected points as black circular points

5. Import a Rhinoceros file containing the 3D calibration frame points. The 2D distortion-corrected calibration points are shown as black outlined squares and the 3D calibration frame points are shown as red outlined squares (Figure F.6)

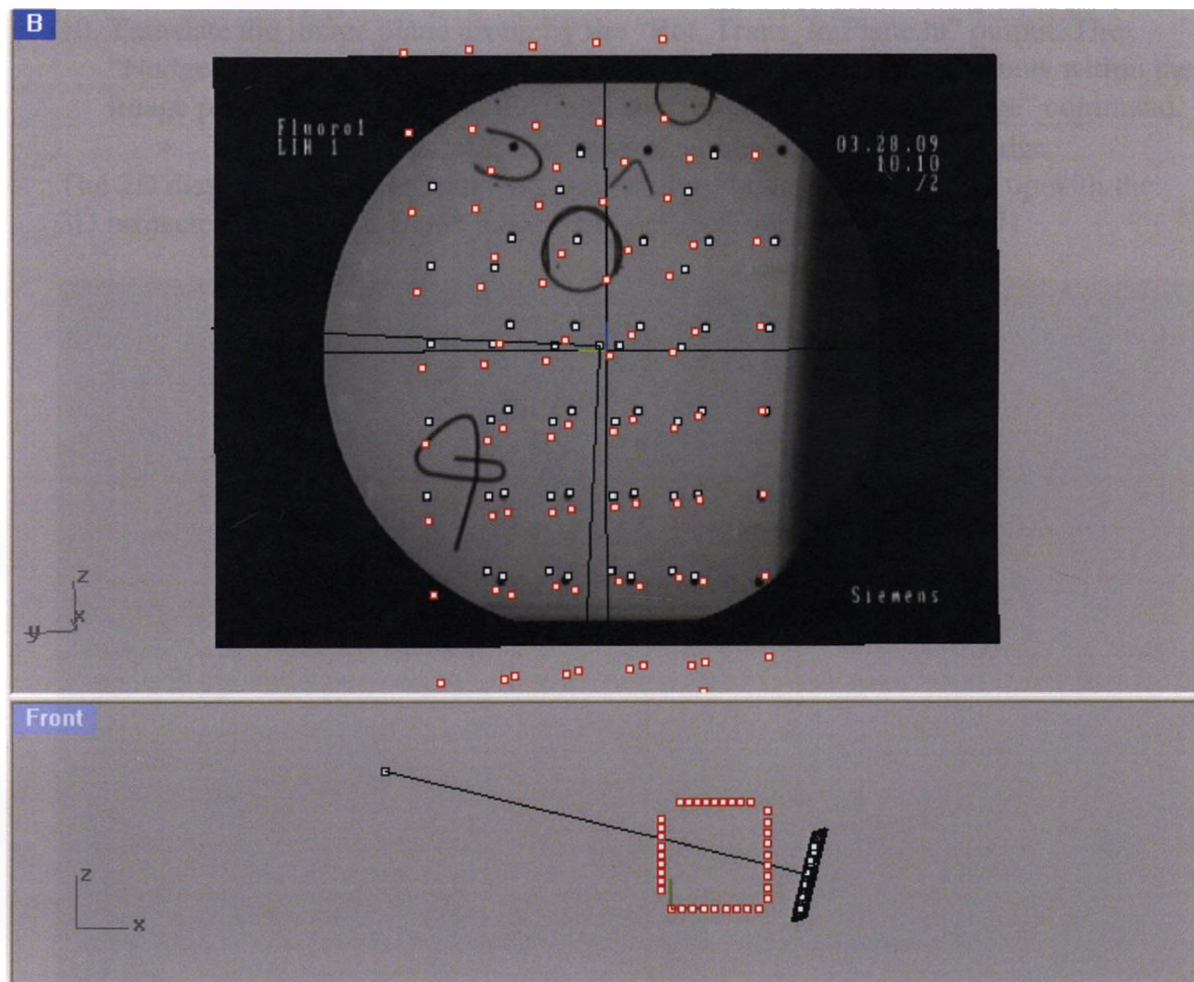


Figure F.6: 2D distortion-corrected points as open black squares, 3D projected points as open red squares and uncorrected points as black circular points

6. Run "ProjectPoints.rvb"(Appendix D.3) in Rhinoceros to project the 3D calibration frame points onto the image plane. When running the code:
 - Click the image plane
 - Only click red 3D calibration frame points that have a corresponding 2D distortion-corrected calibration point.
 - Click the fluoroscope source
 - Type in "DistGridCoordSys" as the CPlane
 - Save the excel file as FluoroB-ProjPoints
7. Run "Rot_Trans_ImPlane.m" (Appendix D.4) in MATLAB to determine the final image plane rotation and translation correction.
8. Ensure the CPlane is set to "DistGridCoordSys"
9. Rotate the image plane group by the "Rot_Trans_ImPlane.m" output. The MATLAB command window will specify the point of rotation (**Command:** rotate)

10. Translate the image plane group by the “Rot_Trans_ImPlane.m” output. The “Nudge” command is useful for translating objects by specific amounts within the image plane because can put the translation amounts into the “Nudge” command.

- Tools → Options → Rhino Options → Modeling Aids → Nudge

The 2D distortion-corrected points (black outlined squares) should line up with the 3D projected calibration frame points (red outlined squares) (Figure F.7)






Figure F.7: Final image plane pose

11. Ungroup the image from the 2D distortion-corrected points. (**Command:** ungroup)
12. Fix the location of the image plane (**Command:** Lock)
13. Hide any objects that are obstructing the image (**Command:** Hide)

APPENDIX G – MATCHING INSTRUCTIONS AND CODE

This Appendix describes the steps taken in matching a 3D model to 2 fluoroscopic images. It also provides to the code necessary to export the 3D coordinates of bony landmarks in the laboratory coordinate system.

G.1 MATCHING INSTRUCTIONS

1. Complete Appendix E and F for both fluoroscopes.
2. Import the 3D model as a stl format.
3. Import the bony landmarks as iges format. Their location should correspond with bony landmarks on the 3D model.
4. Name each bony landmark ( → Properties → Object → Name)
5. Group the 3 bony landmarks to the 3D model (**Command:** Group)
6. Rotate and translate the 3D model to match the 2 images using the following commands: Rotate, Rotate3D, Move, Nudge
 - You can change the amount that a “Nudge” moves an object
Tools → Options → Rhino Options → Modeling Aids → Nudge
7. It may be useful to change the colour of the 3D model group
( → Properties → Object → Display Color)
or to render the 3D model group
(right click on the view → change from “Wireframe” to “Rendered”)
8. Zoom in and out of the image plane by changing the lens length
( → Properties → Camera → Lens length)
9. Focus in on a different portion of the image plane by changing the target location
10. Begin by matching a bone’s silhouette to the entire bony outline on the image.
Focus on the overall pose and do not rotate/translate the 3D model increments in less than 1 mm or 1 °.
11. Choose one or two easily identifiable bony landmarks on each image.
12. Match the 3D models to these chosen bony landmarks, while still ensuring a good match for the overall bone. “Nudge” is a useful command for moving the bone by small increments.
13. When you are satisfied that the bone is matched, ungroup the 3D model from the bony landmarks.
14. Export the 3D coordinates of the bony landmarks by running “ExportPoints.rvb” (Appendix G.2)

G.2 “EXPORTPOINTS.RVB”

'Program: ExportPoints

'Export the 3D coordinates of bony landmarks

'Date Created: Oct 29, 2009

'Created by: Anne-Marie Allen

Call ExportPoints

Sub ExportPoints

Dim arrPoints, arrPointsName, strPointsName

'User selects bony landmarks to export

arrPoints = Rhino.GetObjects("Select bony landmarks to export")

Rhino.Print "Only click points which have corresponding 2D distortion corrected points."

If Not IsArray(arrPoints) Then

 Rhino.Print "Invalid points selected. Please run code again."

 Exit Sub

End If

'Determines how many points were picked

Dim intUBound

intUBound = UBound(arrPoints)

'Prints the points to be projected

arrPointsName = Rhino.ObjectNames(arrPoints)

Dim i

For i = 0 To intUBound

 strPointsName = arrPointsName(i)

 Rhino.Print "You selected point " & (strPointsName) & " to be exported"

Next

'Determines the coordinates of the points

For i = 0 To intUBound

 arrPoints(i) = Rhino.PointCoordinates(arrPoints(i))

 Rhino.Print "Point Coord is "

 Rhino.Print Rhino.Pt2Str(arrPoints(i))

Next

'Exports projected points to an excel file

Dim objExcel

Set objExcel = CreateObject("Excel.Application") 'Launch excel

```
objExcel.Visible = True 'Make excel visible
```

```
objExcel.WorkBooks.Add 'Add a new workbook
```

```
objExcel.Columns(1).ColumnWidth = 15
```

```
objExcel.Columns(2).ColumnWidth = 15
```

```
objExcel.Columns(3).ColumnWidth = 15
```

```
objExcel.Columns(4).ColumnWidth = 15
```

```
'objExcel.Cells(1, 1).Value = "X Coord"
```

```
'objExcel.Cells(1, 2).Value = "Y Coord"
```

```
'objExcel.Cells(1, 3).Value = "Plane Type"
```

```
'objExcel.Cells(1, 4).Value = "Plane Number"
```

```
'objExcel.Cells(1, 5).Value = "Bead Number"
```

```
Dim intIndex
```

```
intIndex = 1
```

```
For i = 0 To intUBound
```

```
    strPointsName = arrPointsName(i)
```

```
    objExcel.Cells(intIndex + i, 1).Value = Mid(strPointsName,1)
```

```
    objExcel.Cells(intIndex + i, 2).Value = arrPoints(i)(0)
```

```
    objExcel.Cells(intIndex + i, 3).Value = arrPoints(i)(1)
```

```
    objExcel.Cells(intIndex + i, 4).Value = arrPoints(i)(2)
```

```
Next
```

```
objExcel.Quit
```

```
End Sub
```

APPENDIX H – LETTER OF PERMISSION TO REPRODUCE JOURNAL MATERIAL



Anne-Marie Allen

To permissions@iop.org

cc

bcc

22/09/2009 16:39

Subject Requesting Permission

Wolf Orthopaedic Biomechanics Laboratory
The University of Western Ontario
3m Centre, Room 1230,
UWO, London, ON N6A 3K7
Canada

Anne-Marie Allen

To Whom it May Concern,

I am preparing an engineering masters monograph thesis entitled "Development and Validation of a Markerless Radiostereometric Analysis (RSA) System".

I would appreciate permission to reproduce the following item in a printed copy of my thesis. In case you do not control these rights, I would appreciate it if you could let me know to whom I should apply for permissions.

1. Figure 14. Michael, G. (2001). X-ray computed tomography. *Physics Education* , 36 (6), 442-451. Published by the Institute of Physics (IOP)



Thank you,

Anne-Marie Allen

PERMISSION TO REPRODUCE AS REQUESTED
IS GIVEN PROVIDED THAT:

- (a) the consent of the author(s) is obtained
- (b) the source of the material including author/editor, title, date and publisher is acknowledged.

IOP Publishing Ltd
Dirac House
Temple Back
BRISTOL
BS1 6BE

from **Gregory Michael** [hide details](#) 12:14 AM (8 hours ago)  [Reply](#) 

to Anne-Marie Allen
 date Thu, Sep 24, 2009 at 12:14 AM
 subject RE: Requesting Permission

Anne-Marie,
 Yes, go ahead, that's ok with me. Good luck with the thesis.
 Cheers,
 Greg.

From: On Behalf Of Anne-Marie Allen

Sent: Thursday, 24 September 2009 1:03 AM
To: Gregory Michael
Subject: Requesting Permission

- Hide quoted text -
 Wolf Orthopaedic Biomechanics Laboratory
 The University of Western Ontario
 3m Centre, Room 1230,
 UWO, London, ON N6A 3K7
 Canada

Anne-Marie Allen

Dear Dr. Micheal,

I am preparing an engineering masters monograph thesis entitled "Development and Validation of a Markerless Radiostereometric Analysis (RSA) System" .

I would appreciate your permission to reproduce the following item in a printed copy of my thesis.

1. Figure 14. Michael, G. (2001). X-ray computed tomography. *Physics Education*, 36(6), 442-451. Published by the Institute of Physics (IOP)

I have received permission from the IOP Publishing (please find attached). They informed me that I am able to reproduce the figure once I also obtain your permission.

Please let me if I can provide you with more information.

Thank you very much,
 Anne-Marie Allen